Design and Control of a Tilt-Rotor Tailsitter Aircraft

Ma, Z.

DOI
10.4233/uuid:ea2515e0-5642-404d-a59d-03233659f59a

Publication date
2026

Document Version
Final published version

Citation (APA)
Ma, Z. (2026). *Design and Control of a Tilt-Rotor Tailsitter Aircraft*. [Dissertation (TU Delft), Delft University of Technology]. https://doi.org/10.4233/uuid:ea2515e0-5642-404d-a59d-03233659f59a

DESIGN AND CONTROL OF A TILT-ROTOR TAILSITTER AIRCRAFT

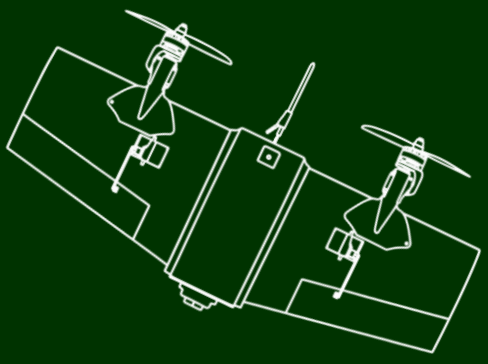

Ziqing Ma

Design and Control of a Tilt-Rotor Tailsitter Aircraft

Ziqing MA

Design and Control of a Tilt-Rotor Tailsitter Aircraft

Proefschrift

ter verkrijging van de graad van doctor
aan de Technische Universiteit Delft,
op gezag van de Rector Magnificus prof.dr.ir. T.H.J.J. van den Hagen,
voorzitter van het College voor Promoties,
in het openbaar te verdedigen op maandag 5 januari 2026 om 12:30 uur

door

Ziqing MA

Master of Engineering in Control Science and Engineering,
Northwestern Polytechnical University, Xi'an, China,
geboren te Hubei, China.

Dit proefschrift is goedgekeurd door de promotoren:

Prof. dr. G.C.H.E. de Croon
Dr. ir. E.J.J. Smeur

Samenstelling promotiecommissie:

Rector Magnificus	voorzitter
Prof. dr. G.C.H.E. de Croon	Technische Universiteit Delft, promotor
Dr. ir. E.J.J. Smeur	Technische Universiteit Delft, copromotor
Onafhankelijke leden:	
Prof. dr. ir. L.L.M. Veldhuis	Technische Universiteit Delft
Dr. ir. E. van Kampen	Technische Universiteit Delft
Dr. S. Sun	Technische Universiteit Delft
Prof. dr. E.N. Johnson	Pennsilvania State University, US
Dr. M. Bronz	Ecole Nationale de l'Aviation Civile, France
Prof. dr. ir. M. Mulder	Technische Universiteit Delft, reserve member

Keywords: VTOL aircraft, wind tunnel tests, incremental control, wing-propeller interaction
Cover design: Ziqing Ma & Yu Wang

ISBN 978-94-6518-205-6

An electronic version of this dissertation is available at
http://repository.tudelft.nl/.

Contents

Summary

Hybrid unmanned aerial vehicles (UAVs) with vertical take-off and landing (VTOL) capability combine efficient forward flight with hovering, making them ideal for missions requiring both high-speed flight and precise maneuvering. Among various hybrid UAVs, tailsitters offer a compact and mechanically efficient solution for applications such as search-and-rescue and environmental monitoring. However, operation across the full flight envelope remains challenging due to highly nonlinear aerodynamics at high angles of attack (AoA)and limited control authority caused by actuator saturation. This work addresses these challenges through a systematic integration of wind tunnel–based aerodynamic analysis, control law development, and flight test validations, culminating in an integrated design and control framework enabling agile, robust, and fully autonomous tailsitter flight.

Firstly, wind tunnel tests were performed on a tailsitter wing under varying propeller thrust, elevon deflection, and airspeed across the full range of angles of attack, resulting in the first publicly available aerodynamic dataset of its kind. The results reveal nonlinear aerodynamic behavior, including during stall, post-stall, and reverse flow. In reversed flow, elevon-induced pitch moments act oppositely to normal flow, though this can be mitigated by increasing throttle. Elevon deflection proves effective at low angles of attack and high airspeeds, but its influence degrades at high angles and low speeds. These findings underscore the need for alternative or supplemental actuation to maintain control authority, especially in vertical or descending flight where traditional surfaces lose effectiveness.

Secondly, in response to the limited pitch control authority observed in conventional elevon-only tailsitters (E-tailsitters), new control strategies are necessitated to achieve full-envelope autonomous flight without actuator saturation. A tailsitter equipped with dual tilt rotors (TR-tailsitter) is introduced, which relies exclusively on thrust vectoring for control moment generation. While thrust vectoring provides ample pitch control authority in hover and vertical flight, it lacks sufficient roll control during forward flight due to wing-propeller interaction. To address this limitation, a TRE-tailsitter is proposed, integrating tilting rotors with conventional elevons. This combined actuation setup provides complementary control, with tilt rotors primarily handling low-speed and vertical flight phases, while elevons dominate during high-speed cruise. To achieve full-envelope autonomous flight, a cascaded Incremental Nonlinear Dynamic Inversion (INDI) controller is implemented, with Weighted Least Squares (WLS) control allocation, which dynamically coordinates actuator allocation between rotor tilt and elevon deflection across different flight regimes, avoiding actuator saturation and ensuring seamless transitions.

Thirdly, to enable fully autonomous field deployment, a pivoting takeoff and

landing controller is developed for robust VTOL operation under windy and uneven terrain conditions. By exploiting rotor tilt, the vehicle initiates liftoff from a horizontal ground posture through a controlled pivoting motion around its tail, eliminating the need for landing gear and enabling deployment on uneven terrains. Indoor and outdoor flight tests validate the stability and robustness of the proposed approach in the presence of wind disturbances.

Fourthly, the agility of the tilt-rotor tailsitter UAV is examined through high-speed sharp turn scenarios, where maximizing lift is essential for minimizing turning radius. Wind tunnel data covering various actuator combinations are used to develop empirical models of axial force, lift and pitch moment w.r.t thrust, rotor tilt, elevon deflection, AoA, and airspeed, capturing wing–propeller interaction effects. The derived models and pitching moment trim tests reveal that upward rotor tilt combined with downward elevon deflection enhances lift while maintaining pitch equilibrium. Furthermore, a theoretical minimum turning radius of $8.01m$ at $18m/s$ coordinated sharp turn is computed, confirming that coordinated actuation enables aggressive maneuvers without compromising pitch stability or speed.

Overall, this dissertation develops a tilt-rotor tailsitter UAV capable of robust, autonomous and agile operation across the full flight envelope.The proposed framework advances the understanding of tailsitter aerodynamics and control, and provides a pathway toward field-deployable UAVs for demanding missions requiring both maneuverability and autonomy.

Samenvatting

Hybride onbemande luchtvaartuigen (UAV's) met verticale start- en landingscapaciteiten (VTOL) combineren efficiënte voorwaartse vlucht met de mogelijkheid om te blijven zweven, waardoor ze ideaal zijn voor missies die zowel vluchten op hoge snelheid als nauwkeurige manoeuvres vereisen. Onder de diverse hybride UAV's bieden tailsitters een compacte en mechanisch efficiënte oplossing voor toepassingen zoals zoek- en reddingsacties en milieumonitoring. Operaties over het volledige vliegbereik blijven echter uitdagend vanwege de zeer niet-lineaire aerodynamica bij hoge invalshoeken (Angle of Attack - AoA) en de beperkte stuurautoriteit veroorzaakt door actuatorverzadiging. Dit werk pakt deze uitdagingen aan door een systematische integratie van aerodynamische analyses gebaseerd op windtunneltests, de ontwikkeling van regelwetten en validaties door middel van vliegtests. Dit resulteert in een geïntegreerd ontwerp- en regelkader dat een wendbare, robuuste en volledig autonome vlucht van de tailsitter mogelijk maakt.

Ten eerste zijn er windtunneltests uitgevoerd op een tailsitter-vleugel onder variërende propellstuwkracht, elevon-uitslag en luchtsnelheid over het volledige bereik van invalshoeken, wat heeft geresulteerd in de eerste openbaar beschikbare aerodynamische dataset in zijn soort. De resultaten tonen niet-lineair aerodynamisch gedrag aan, waaronder tijdens overtrek (stall), post-stall en omgekeerde stroming. Bij omgekeerde stroming werken de door de elevon geïnduceerde stampmomenten in tegengestelde richting ten opzichte van normale stroming, hoewel dit kan worden gecompenseerd door het verhogen van de stuwkracht. Elevon-uitslag blijkt effectief bij lage invalshoeken en hoge luchtsnelheden, maar de invloed neemt af bij hoge hoeken en lage snelheden. Deze bevindingen onderstrepen de noodzaak voor alternatieve of aanvullende actuatie om stuurautoriteit te behouden, vooral tijdens verticale of dalende vluchten waar traditionele stuurvlakken hun effectiviteit verliezen.

Ten tweede zijn er, als reactie op de beperkte stampstuurautoriteit die werd waargenomen bij conventionele tailsitters met alleen elevons (E-tailsitters), nieuwe regelstrategieën nodig om autonome vluchten over het volledige bereik te realiseren zonder actuatorverzadiging. Er wordt een tailsitter geïntroduceerd die is uitgerust met dubbele kantelrotoren (TR-tailsitter), die uitsluitend vertrouwt op stuwkrachtvectoring voor het genereren van stuurmomenten. Hoewel stuwkrachtvectoring voldoende stampstuurautoriteit biedt tijdens zweven en verticale vluchten, ontbreekt het aan voldoende rolbesturing tijdens voorwaartse vluchten als gevolg van vleugel-propellerinteractie. Om deze beperking aan te pakken, wordt een TRE-tailsitter voorgesteld, waarbij kantelrotoren worden geïntegreerd met conventionele elevons. Deze gecombineerde actuatie-opstelling biedt complementaire besturing, waarbij kantelrotoren voornamelijk de lage-snelheids- en verticale vluchtfasen voor hun rekening nemen, terwijl elevons domineren tijdens kruisvluchten met hoge

snelheid. Om autonome vluchten over het volledige bereik te bereiken, is een gecascadeerde Incremental Nonlinear Dynamic Inversion (INDI) regelaar geïmplementeerd, met Weighted Least Squares (WLS) regelallocatie, die de actuatorallocatie tussen rotorkanteling en elevon-uitslag dynamisch coördineert over verschillende vluchtregimes, waardoor actuatorverzadiging wordt vermeden en naadloze overgangen worden gegarandeerd.

Ten derde is, om volledig autonome inzet in het veld mogelijk te maken, een pivot-start- en landingsregelaar ontwikkeld voor robuuste VTOL-operaties onder winderige omstandigheden en op ongelijk terrein. Door gebruik te maken van rotorkanteling initieert het voertuig het opstijgen vanuit een horizontale grondhouding via een gecontroleerde draaibeweging rond zijn staart, waardoor een landingsgestel overbodig wordt en inzet op oneffen terreinen mogelijk is. Vliegtests binnen en buiten valideren de stabiliteit en robuustheid van de voorgestelde aanpak in de aanwezigheid van windverstoringen.

Ten vierde wordt de wendbaarheid van de tilt-rotor tailsitter UAV onderzocht door middel van scenario's met scherpe bochten op hoge snelheid, waarbij het maximaliseren van de lift essentieel is voor het minimaliseren van de draaicirkel. Windtunneldata die verschillende actuatorcombinaties bestrijken, worden gebruikt om empirische modellen te ontwikkelen van axiale kracht, lift en stampmoment met betrekking tot stuwkracht, rotorkanteling, elevon-uitslag, invalshoek en luchtsnelheid, waarbij de effecten van vleugel-propellerinteractie worden vastgelegd. De afgeleide modellen en trimtests voor het stampmoment tonen aan dat opwaartse rotorkanteling gecombineerd met neerwaartse elevon-uitslag de lift verbetert terwijl het stampevenwicht behouden blijft. Bovendien wordt een theoretische minimale draaicirkel van $8{,}01\ \mathrm{m}$ bij een gecoördineerde scherpe bocht van $18\ \mathrm{m/s}$ berekend, wat bevestigt dat gecoördineerde actuatie agressieve manoeuvres mogelijk maakt zonder de stampstabiliteit of snelheid in gevaar te brengen.

Over het geheel genomen ontwikkelt dit proefschrift een tilt-rotor tailsitter UAV die in staat is tot robuuste, autonome en wendbare operaties over het volledige vliegbereik. Het voorgestelde kader bevordert het begrip van tailsitter-aerodynamica en -besturing, en biedt een weg naar in het veld inzetbare UAV's voor veeleisende missies die zowel wendbaarheid als autonomie vereisen.

Nomenclature

α	Angle of attack
θ	Pitch angle
γ	Flight path angle
ξ	Heading angle
μ	Bank angle
p	Roll rate
q	Pitch rate
r	Yaw rate
V	Airspeed
L	Lift force
D	Drag force
C_L	Lift coefficient
C_D	Drag coefficient
C_M	Pitching moment coefficient
ρ	Air density
$\bar{q}$	Dynamic pressure
S	Reference area
c_a	Mean aerodynamic chord
u	Control input
u_{eq}	Control input equilibrium component
Δu	Control input feedback correction
u	Control input
T	Thrust
T_Z	Overall thrust
δ_f	Flap deflection
δ_e	Elevon deflection
δ_l, δ_r	Tilt angles of the left and right rotors
T_l, T_r	Thrusts of the left and right rotors
$\mathbf{\Omega}$	Angular velocity vector
$\dot{\mathbf{\Omega}}$	Angular acceleration vector
$\mathbf{q_{ref}}$	Reference quaternion
$\mathbf{q_s}$	Quaternion state
$\mathbf{q_{error}}$	quaternion error
$\mathbf{I}$	Diagonal inertia matrix
$\mathbf{M}_a$	Aerodynamic moment vector
$\mathbf{M}_c$	Control moment vector
$\mathbf{M}_{\delta_T}$	Control moment vector by rotor tilt

$\mathbf{G}_{\delta_T}$	Control effectiveness of rotor tilt
$\mathbf{G}_T$	Control effectiveness of thrust
$\mathbf{G}_E$	Control effectiveness of elevon deflection
$\mathbf{W}_u$	Control input weighting matrix
$\mathbf{W}_v$	Control objective weighting matrix
W_{uTilt}	Allocated eight for rotor tilt
$W_{uElevon}$	Allocated eight for elevon deflection
ω_l, ω_r	Angular velocities of the left and right rotors
m	Mass of the vehicle
g	Gravitational constant
τ_d	Actuator delay
ζ	Damping ratio
R	Turning radius

1

Introduction

Unmanned aerial vehicles (UAVs) capable of vertical take-off and landing (VTOL) have gained considerable attention in recent years. Traditional UAV configurations typically fall into two categories. Rotorcraft, such as quadcopters, excel at hovering and vertical maneuvers. Fixed-wing aircraft, on the other hand, are known for their efficient high-speed and long-range flight. VTOL UAVs aim to combine the advantages of both, offering the cruise efficiency of fixed wings along with the vertical lift and maneuverability of rotorcraft. This hybrid capability enhances mission range and operational efficiency, which is critical in applications such as aerial mapping, environmental monitoring, and search-and-rescue operations.

A variety of hybrid VTOL configurations have been explored, including quadplanes[1], [2], tilt-wings[3], [4], tilt-rotors (fixed-wing)[5], [6], and tailsitters[7], [8], as illustrated in Figure 1.1. Among these, *tailsitters* form a distinctive category: they take off and land on their tails and transition to forward flight by pitching their entire body 90°, rather than by changing the orientation of wings or rotors.

It is worth noting that tailsitters themselves span multiple subclasses. In addition to wing-borne tailsitters, a number of ducted-fan vehicles, such as cylindrical or canister-shaped designs, can also be regarded as tailsitters in a geometric sense, as they similarly operate with a vertical body axis during takeoff and landing and transition by body pitching. However, these ducted-fan platforms fundamentally differ from winged tailsitters in both aerodynamic mechanisms and control characteristics, as lift and control are primarily generated by the internal ducted flow rather than by aerodynamic surfaces. As a result, their performance, flow physics, and control structure are more closely related to thrust-dominated rotorcraft or jet-

like vehicles than to fixed-wing aircraft. In this dissertation, the term "tailsitter" specifically refers to winged tailsitters, for which aerodynamic lift is generated primarily by fixed wings during forward flight. The focus is therefore on platforms that combine the aerodynamic efficiency of wings with the hovering capability of VTOL propulsion, and not on ducted-fan or purely thrust-borne platforms.

Tailsitters' unique mode of transition, achieved simply by rotating the vehicle, reduces mechanical design complexity and is advantageous for missions requiring rapid transition between hover and forward flight. Despite this renewed interest, tailsitter UAVs still face critical technical challenges that have hindered their broader applications. In particular, four key areas are identified as focal challenges and will be discussed in follow-up sections, along with related prior work, to delineate the scope of the research.

(a) Quadplane [2]

(b) Tilt-wing [4]

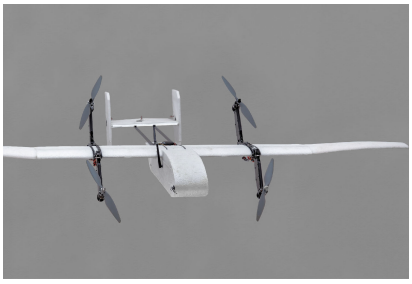

(c) Tilt-rotor (fixed-wing) [6]

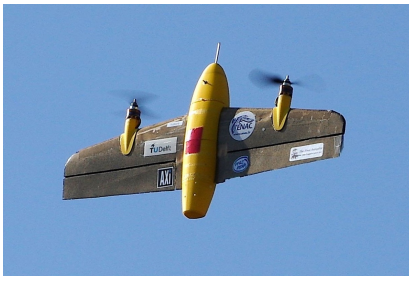

(d) Tailsitter [8]

Figure 1.1: Four categories of hybrid VTOL aircraft: (a) quadplanes, (b) tilt-wings, (c) tilt-rotors (fixed-wing), and (d) tailsitters.

1.1. Aerodynamics of Tailsitters

Tailsitter UAVs operate across a broad flight envelope that extends beyond that of both quadrotors and conventional fixed-wing aircraft. During mode transitions

between vertical and horizontal flight, the vehicle undergoes large pitch rotations, resulting in angles of attack (AoA) that can exceed 90°. Operating in this regime exposes the aircraft to highly nonlinear aerodynamic phenomena including flow separation, stall, and inverse flow, posing significant challenges for modeling, control, and stability.

Given the difficulty of constructing accurate theoretical models under such nonlinear conditions, wind tunnel testing becomes an essential tool for capturing the aerodynamic characteristics of tailsitter configurations. Gamble et al.[9] investigated the influence of propeller slipstream on a 24-inch flexible wing, estimating that 12–18% of the propeller thrust was converted into additional drag on the airframe. Fratello et al.[10] performed low-speed wind tunnel experiments on both propeller-wing and nacelle-wing layouts, revealing the intricate aerodynamic interactions among the propeller, nacelle, and wing. Several studies, including those by Stoll[11], Ananda[12], and Hrishikeshavan[13], further examined hybrid wing–propeller interactions under various conditions. Since the available NACA4412 airfoil data[14] cover only a limited AoA range of -16° to 20°, Kubo et al. [15] utilized modified NACA0012 data[16] to interpolate aerodynamic characteristics beyond this AoA range for their NACA4412-based main wing. Lyu et al.[17] conducted full-envelope wind tunnel tests on a tailsitter UAV, providing experimentally derived aerodynamic coefficients across a wide range of flight conditions. Similarly, Truong et al.[18] developed a semi-empirical model to estimate aerodynamic forces over the entire AoA spectrum. Notably, Snyderet al.[19] experimentally characterized four airfoils from 0° to 360° AoA, including aileron deflections up to $\pm 60^\circ$ on a NACA 23024 section, but observed little control authority beyond $\pm 20^\circ$ deflection. Despite these contributions, aerodynamic datasets covering the full AoA range for tailsitter UAVs remain scarce, particularly for small, low-cost platforms.

In addition to angle of attack, the aerodynamics of a tailsitter is strongly influenced by actuator inputs, thrust magnitude and control surface deflections. These actuator inputs affect not only the net propulsion but also modify the local airflow around the airframe, due to strong propeller–wing interactions. To support accurate control allocation and ensure sufficient controllability across the entire flight envelope, it is essential to characterize the aerodynamic response under systematic variations of thrust, elevon deflection, airspeed and angle of attack. However, existing literature rarely reports comprehensive datasets that span all angles of attack, multiple airspeeds, and diverse actuator configurations. This motivates thorough wind tunnel testing to empirically investigate the actuator–aerodynamic coupling,

1

forming the foundation for robust full-envelope control strategies.

1.2. Autonomous and Robust Takeoff and Landing

Apart from the challenge of highly-nonlinear aerodynamics, tailsitter UAVs continue to face fundamental limitations in their takeoff and landing operations, which constrain their autonomy and field applicability. Conventional tailsitter platforms with fixed rotors and control surfaces are designed to take off and land in an upright, vertical orientation. To ensure this posture on the ground, such systems often rely on dedicated support structures, including elongated landing gear, fins, or external launch frames [20], [21], [22], [23]. While mechanically straightforward, these additions increase structural weight and drag, directly impacting flight efficiency, endurance, and payload capacity. More importantly, the need for precise upright placement introduces a strong dependence on operator intervention and environmental conditions. The tailsitter must be carefully positioned and stabilized prior to each takeoff, which can be complicated under windy or uneven terrain conditions. Once toppled, the tailsitter cannot autonomously recover its posture for re-launch, necessitating manual reset by a human operator. This lack of robustness under field conditions hampers deployment flexibility and undermines the suitability of tailsitters for autonomous or persistent operations in dynamic, unstructured environments.

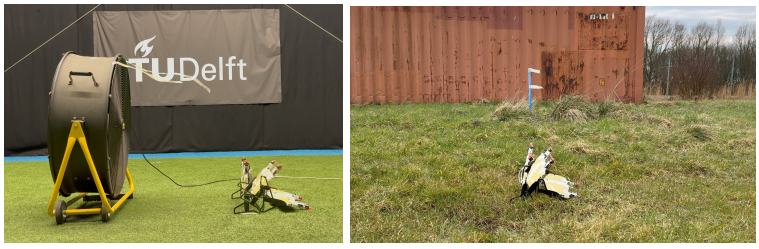

Figure 1.2: Conventional tailsitters with only control surfaces blown over under windy conditions before takeoff

To overcome these limitations, recent developments have explored alternative VTOL strategies that relax the need for upright ground posture. One promising approach is the pivot or "belly" takeoff maneuver, in which the vehicle starts from a horizontal resting position and uses thrust vectoring to rotate into a vertical hover. This concept has been demonstrated in the ArduPilot Thrust Vectored Belly Sitter (TVBS) project as well as in more recent research by Wang et al. [24], where a tilt-rotor mechanism is used solely to pitch the vehicle up from the ground, lifting

it into hover without the need for ground fixtures. However, their system exhibited significant pitch overshoot of 50° as well as notable lateral drift, both of which reduce flight safety and control precision during takeoff. Moreover, the landing phase was not fully autonomous: the UAV was manually caught by hand at low altitude to avoid hard impact. This not only introduces safety concerns but also limits operational autonomy and reliability, especially in windy or cluttered environments.

These observations indicate that existing implementations still suffer from control instability and a reliance on human intervention during critical phases. Achieving reliable and autonomous takeoff and landing from arbitrary flat surfaces under external disturbances such as wind remains a key challenge. Addressing this limitation is essential to enhance the practical deployability and operational resilience of tailsitter UAVs in real-world environments.

1.3. Full-envelope Control Without Actuator Saturation

Maintaining stable attitude control across all flight phases is particularly challenging for a tailsitter UAV due to the drastic variation in control effectiveness. In forward flight, aerodynamic control surfaces such as elevons are highly effective; even small deflections can generate sufficient control moments due to the high dynamic pressure. However, in vertical or descending flight, airflow over the surfaces is insufficient or even reversed, significantly reducing their effectiveness. This loss of authority leads to large deflection demands from the controller, which often exceed actuator limits, resulting in actuator saturation.

Actuator saturation during transition or low-speed maneuvers can severely degrade tracking performance, induce oscillations, or even lead to complete loss of control. This issue is particularly critical in conventional E-tailsitters (tailsitters with only aerodynamic control surfaces that function like elevons), where the absence of alternative moment-generation mechanisms forces the aerodynamic surfaces to operate at or beyond their limits. As observed in [8], saturation in pitch control near hover or during descent can render the vehicle unresponsive or unstable, compromising safe operation. In essence, a pure aerodynamic control scheme has a limited flight envelope. The flight performance in the high-speed forward flight phase can be guaranteed, but as airspeed decreases during vertical flight or descending, the vehicle can become uncontrollable due to vanishing control authority. This undermines the feasibility of conventional control-surface-only control and motivates the

use of thrust vectoring or alternative actuation to ensure controllability across the full flight envelope.

Ensuring stable control throughout the entire flight envelope, especially during transitions between hover and forward flight, is vital for the safe and agile operation of hybrid tailsitter UAVs. Smooth transitions require a global control approach without relying on discrete switching between flight modes. Therefore, the design of a unified control law capable of handling a wide range of aerodynamic conditions remains a central challenge in the control of tailsitters.

Conventional methods often employ separate control strategies for different flight phases. For instance, in [25] and [26], the authors proposed distinct controllers for hover and cruise regimes. Although this modularity facilitates transitions between vertical and forward flight phases, it requires manual or automatic switching between individual controllers, leading to discontinuities at mode boundaries.

To overcome these limitations, global controllers that span the full flight envelope have been investigated. In [27], a cascaded proportional–integral–derivative (PID) controller was implemented and validated through indoor trajectory tracking. However, the system exhibited noticeable pitch tracking errors, particularly under aggressive flight conditions. An alternative approach explored in [23] and [28] involved exploiting the property of differential flatness to design global controllers for E-tailsitters. These controllers enabled agile and aerobatic maneuvers in confined indoor environments. Similarly, Lu et al. [29] developed a model predictive controller based on differential flatness and a high-fidelity aerodynamic model, enabling aggressive and smooth trajectory tracking in outdoor flight tests. Other global control methods have also been explored. Mcintosh et al. [30] proposed a position control architecture for a simplified tailsitter model, incorporating a nonlinear dynamic inversion (NDI) controller for attitude control in simulation. While promising in structure, NDI requires precise aerodynamic models to ensure stability and is thus sensitive to modeling inaccuracies during transitions. To reduce this dependency on modeling accuracy, Smeur et al. [31] introduced a cascaded sensor-based incremental nonlinear dynamic inversion (INDI) controller for an E-tailsitter platform. By relying on direct sensor feedback instead of preidentified models, the INDI approach achieved robust control performance in outdoor environments, though elevon saturation was also observed.

Despite these advancements, achieving reliable full-envelope control without actuator saturation remains an open challenge for hybrid tailsitter UAVs. The highly nonlinear aerodynamic environment, combined with large variations in control ef-

fectiveness across flight modes, imposes stringent requirements on the controller's adaptability. A comprehensive control framework that unifies these aspects is necessary to enable agile, reliable, and fully autonomous operation of tailsitter UAVs under realistic mission scenarios.

1.4. Agile Maneuverability for High-speed Flight

Beyond ensuring basic controllability, an important goal for hybrid VTOL aircraft is to exploit their capabilities for truly agile flight. Achieving agile maneuvers such as sharp banked turns, rapid climbs, or aerobatic transitions requires both sufficient control authority and intelligent use of the available actuators.

Recent research demonstrates the agility potential of tailsitters. Tal et al [28] generated aerobatic trajectories for a tailsitter (with only aerodynamic controls) that include knife-edge and climbing turn, by using a differential-flatness-based trajectory planner. Their indoor flight tests showed that the vehicle could perform complex maneuvers in a confined space, transitioning between hover and fast translations smoothly. Lu et al. [29] extended this line of work by developing a model predictive controller based on differential flatness, enabling aggressive outdoor maneuvers such as steep dives followed by recoveries, sharp turns at high speed, and rejoining trajectories after temporary deviations. These works demonstrate that, when equipped with well-optimized controllers and accurate aerodynamic models, tailsitters are capable of executing high-agility maneuvers such as rapid transitions, aerobatic turns, and trajectory corrections under dynamic conditions, highlighting their potential for demanding aerial missions that require both maneuverability and versatility.

A suitable scenario to evaluate such agile capabilities is drone racing, which poses a comprehensive challenge to both reliable flight performance and time-optimal control. Unlike conventional quadrotor-based race drones, hybrid UAVs such as tailsitters offer superior forward-flight speed for the same weight, owing to their fixed-wing design. Additionally, the presence of a wing enables tailsitters to generate substantial lateral acceleration during high-speed turns without sacrificing forward thrust, offering a unique advantage in racing scenarios that involve aggressive maneuvers such as sharp turns. In such conditions, achieving a minimal turning radius while maintaining pitch stability and airspeed introduces a significant aerodynamic challenge of accurately characterizing the influence of actuator configurations on lift and control moment generation.

For hybrid tailsitter UAVs which combine tilt-rotor based propulsion with con-

ventional aerodynamic control surfaces, the prediction of lift and control moments becomes more complex due to wing–propeller interaction, defined as the aerodynamic coupling between propeller-induced flow and adjacent airframe surfaces. Propeller-wash modifies the local flow over wings and control surfaces, altering their aerodynamic behavior. Wing–propeller interaction is inherently complex, as it involves coupled effects on pressure distribution, boundary layer development, and flow separation over the lifting surfaces, thereby posing significant challenges for precise aerodynamic characterization and control-oriented modeling.

Some prior studies have investigated the aerodynamic impact of propeller induced flow and the subsequent wing-propeller interaction. As is illustrated in [32], the propeller-induced slipstream modifies local angle of attack distributions over the wing, leading to asymmetric lift profiles and changes in pressure gradients. In [33], the presence of slipstream significantly alters the lift distribution, potentially triggering earlier transitions to turbulent flow and enhancing lift on the upstream wing sections. It is further demonstrated in [34] that such slipstream effects intensify trailing vortices and affect post-propeller wake characteristics. Despite the insights offered by these studies, the coupled aerodynamic effects between wing and propeller in tailsitter configurations remain insufficiently characterized, particularly under aggressive maneuvers involving high angles of attack and complex actuator scheduling. Therefore, a thorough and quantitative analysis of wing-propeller interaction is especially imperative for high-speed sharp turn scenarios, where aerodynamic efficiency and moment equilibrium must be jointly maintained to ensure precise and agile flight.

1.5. Research Objectives and Questions

This dissertation aims to advance the design and control of hybrid tailsitter UAVs by enabling full-envelope flight with high agility, robustness, and control reliability. The main research goal is formulated as follows:

Research Goal

To develop a tailsitter UAV with sufficient control authority to enable autonomous, robust, and precise flight across the entire flight envelope, including vertical takeoff and landing, hover, forward flight, and all transitional phases. The research further aims to investigate the vehicle's capability for agile maneuvers such as sharp turns.

The research goal is further split into four research questions, formulated as follows.

At high angles of attack, particularly near stall or reverse flow conditions, the aerodynamic behavior of lifting surfaces becomes highly nonlinear and poorly understood. This affects both the predictability of aerodynamic forces and the design of control strategies. Precise aerodynamic characterization is therefore essential for the design and control of tailsitter aircraft.

Research Question 1

How does a tailsitter wing behave aerodynamically across different actuator settings, airspeeds, and all angles of attack, and how do these conditions affect its lift and moment generation as well as the control effectiveness of elevons?

Conventional elevon-based control becomes ineffective in certain flight regimes, such as hover or low-speed transitions. To maintain sufficient control authority, novel actuation strategies and coordinated control logic must be explored. This leads to the following question:

Research Question 2

How to design an actuation system and control allocation strategy that guarantees sufficient control authority across all flight phases of a hybrid tailsitter UAV, including hover, transition, and forward flight?

Practical deployment of tailsitter UAVs requires reliable autonomous takeoff and landing, even under environmental disturbances. Ensuring safe and robust operations without human intervention is critical for real-world applications. This motivates the following question:

Research Question 3

How to achieve robust and fully autonomous vertical takeoff and landing for a hybrid tailsitter UAV in unstructured environments with wind disturbances and irregular terrain?

Agile maneuvers such as sharp turns demand precise moment control and high lift, particularly in the presence of complex wing–propeller interactions. Leveraging

1

actuation to enable such performance leads to the final question:

Research Question 4

How to exploit wing–propeller interactions through optimal actuator configurations to enable agile maneuvers, such as sharp turns, without sacrificing forward speed?

By answering these questions, the dissertation intends to fill critical gaps in the current understanding and capabilities of tailsitter UAVs. Each question aligns with one or more of the challenges outlined earlier, and together they cover the spectrum from fundamental aerodynamic knowledge to practical control implementation and flight demonstration.

1.6. Dissertation Outline

The remainder of this dissertation is structured to systematically address the aerodynamic modeling, control design, and experimental validation of a tilt-rotor tailsitter UAV. The chapters are organized to progressively build from a better understanding of the aerodynamics toward the realization of a fully autonomous and agile flight platform. Each chapter contributes a key component of the overall system, culminating in a comprehensive framework for robust, full-envelope operation. A summary of the individual chapters is provided below.

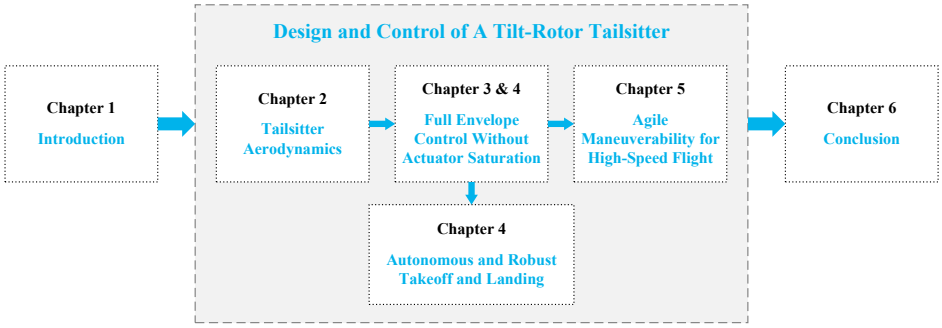

Figure 1.3: The outline of the thesis.

Chapter 2: Wind Tunnel Tests of A Wing across Full 360° Angle of Attack Range This chapter presents wind tunnel experiments conducted on a wing

equipped with fixed rotors and elevons, aimed at capturing aerodynamic characteristics over the full range of angles of attack and various actuator settings. A novel dataset is constructed, detailing lift and moment variations with respect to airspeed, angle of attack, flap deflection, and rotor thrust. In particular, the influence of inverse flow on control effectiveness is analyzed, showing significantly reduced elevon authority during vertical and descending flight. The results serve as a foundation for understanding the aerodynamic constraints of E-tailsitters (tailsitters utilizing control surfaces, like elevons, for moment generation) and motivate the need for alternative control actuation in low-speed regimes.

Chapter 3: Attitude Control of a Tilt-rotor-only Tailsitter Addressing the control limitations observed in Chapter 2, this chapter introduces a tilt-rotor (TR) tailsitter UAV that relies solely on thrust vectoring for control moment generation. An incremental nonlinear dynamic inversion (INDI) controller is implemented to provide robust stabilization without requiring an accurate aerodynamic model. Experimental results show that the use of thrust vectoring significantly mitigates actuator saturation by providing ample pitch moment authority, compared to conventional E-tailsitters. However, limited roll authority is observed during forward flight due to the reliance on tilting rotors alone, highlighting the insufficiency of single-modality actuation for full-envelope control.

Chapter 4: Design and Full-envelope Control of a Tilt-rotor Tailsitter To overcome the roll control limitations identified in Chapter 3, this chapter details the development of a novel tilt-rotor elevon (TRE) tailsitter UAV. The design integrates tilting rotors for vertical-phase control and elevons for forward flight, enabling complementary actuation across the flight envelope. A robust pivoting takeoff and landing mechanism is developed to eliminate the need for upright placement, supporting fully autonomous ground operations. A cascaded INDI control strategy with airspeed-scheduled control allocation is implemented, ensuring smooth transitions and avoiding actuator saturation. Comparative studies with TR-tailsitter and E-tailsitter configurations demonstrate that the TRE-tailsitter achieves superior performance in both vertical and forward flight phases, and the transitions between these two.

Chapter 5: Actuator Configurations for Sharp Turn Maneuvers This chapter explores how actuator configurations influence lift generation to enable agile flight, particularly sharp turns while maintaining airspeed. Wind tunnel experiments

were conducted across various rotor tilt angles, elevon deflections, airspeeds, and AoAs to construct an accurate experimental model linking lift and pitch moment to actuator settings. The tests also reveal key aspects of wing–propeller interaction, especially under coupled thrust vectoring and elevon deflections. Dynamic balance tests were then performed, using upward rotor tilt to counter downward flap-induced moments, achieving pitch moment equilibrium while maximizing lift. The agreement between dynamic and static results validates the aerodynamic model. Finally, the experimental model is used to compute the actuator settings that yield maximum lift while maintaining 18 m/s airspeed, from which the theoretical minimum turn radius is derived. These results provide a quantitative basis for designing sharp-turn maneuvers in future autonomous guidance schemes.

Chapter 6: Conclusions and Future Work The final chapter synthesizes the dissertation's contributions in the context of its original research questions. It emphasizes the significance of all-AoA aerodynamics analysis, actuator saturation eliminated control strategies, and integrated system design. Limitations such as model fidelity and endurance are discussed, along with possible mitigations. The chapter outlines future research directions, including unsteady aerodynamic modeling, learning-based adaptive control, and advanced trajectory planning. The dissertation concludes by highlighting how the presented work advances the capabilities of hybrid VTOL tailsitter UAVs toward real-world autonomy and versatility.

References

[1] H. Karssies and C. De Wagter, "Extended incremental non-linear control allocation (xinca) for quadplanes", *International Journal of Micro Air Vehicles*, vol. 14, p. 17 568 293 211 070 825, 2022.

[2] M. Streetly, *IHS Jane's All the World's Aircraft: Unmanned: 2013-2014*. IHS Global, 2013.

[3] P. Hartmann, C. Meyer, and D. Moormann, "Unified velocity control and flight state transition of unmanned tilt-wing aircraft", *Journal of guidance, control, and dynamics*, vol. 40, no. 6, pp. 1348–1359, 2017.

[4] T. Ostermann, J. Holsten, Y. Dobrev, and D. Moormann, "Control concept of a tiltwing uav during low speed manoeuvring", in *Proceeding of the 28th International Congress of the Aeronautical Sciences: ICAS Brisbane, Australia*, vol. 1190, 2012.

[5] C. Chen, J. Zhang, D. Zhang, and L. Shen, "Control and flight test of a tilt-rotor unmanned aerial vehicle", *International Journal of Advanced Robotic Systems*, vol. 14, no. 1, p. 1 729 881 416 678 141, 2017.

[6] L. Bauersfeld, L. Spannagl, G. J. Ducard, and C. H. Onder, "Mpc flight control for a tilt-rotor vtol aircraft", *IEEE Transactions on Aerospace and Electronic Systems*, vol. 57, no. 4, pp. 2395–2409, 2021.

[7] S. Verling, B. Weibel, M. Boosfeld, K. Alexis, M. Burri, and R. Siegwart, "Full attitude control of a vtol tailsitter uav", in *2016 IEEE international conference on robotics and automation (ICRA)*, IEEE, 2016, pp. 3006–3012.

[8] E. J. J. Smeur, M. Bronz, and G. C. H. E. de Croon, "Incremental control and guidance of hybrid aircraft applied to a tailsitter unmanned air vehicle", *Journal of Guidance, Control, and Dynamics*, vol. 43, no. 2, pp. 274–287, 2020.

[9] B. J. Gamble and M. F. Reeder, "Experimental analysis of propeller-wing interactions for a micro air vehicle", *Journal of Aircraft*, vol. 46, no. 1, pp. 65–73, 2009.

[10] G. Fratello, D. Favier, and C. Maresca, "Experimental and numerical study of the propeller/fixed wing interaction", *Journal of Aircraft*, vol. 28, no. 6, pp. 365–373, 1991.

[11] A. M. Stoll, "Comparison of cfd and experimental results of the leaptech distributed electric propulsion blown wing", in *15th AIAA Aviation Technology, Integration, and Operations Conference*, AIAA, 2015, pp. 1–9.

[12] G. K. Ananda, M. S. Selig, and R. W. Deters, "Experiments of propeller-induced flow effects on a low-reynolds-number wing", *AIAA Journal*, vol. 56, no. 8, pp. 3279–3294, 2018.

[13] V. Hrishikeshavan, C. Bogdanowicz, and I. Chopra, "Experimental investigation of performance of a wing-propeller system for a quad-rotor-biplane micro air vehicle", in *54th AIAA/ASME/ASCE/AHS/ASC Structures, Structural Dynamics, and Materials Conference*, AIAA, 2013, pp. 1–19.

[14] I. H. Abbott and A. E. Von Doenhoff, *Theory of wing sections: including a summary of airfoil data*. Courier Corporation, 2012.

[15] D. Kubo and S. Suzuki, "Tail-sitter vertical takeoff and landing unmanned aerial vehicle: Transitional flight analysis", *Journal of Aircraft*, vol. 45, no. 1, pp. 292–297, 2008.

[16] C. C. Critzos, H. H. Heyson, and R. W. Boswinkle Jr, "Aerodynamic characteristics of naca 0012 airfoil section at angles of attack from 0 degrees to 180 degrees", Langley Aeronautical Laboratory, Tech. Rep., 1955.

[17] X. Lyu, H. Gu, Y. Wang, Z. Li, S. Shen, and F. Zhang, "Design and implementation of a quadrotor tail-sitter vtol UAV", in *2017 IEEE international conference on robotics and automation (ICRA)*, IEEE, 2017, pp. 3924–3930.

[18] V. Truong, "An analytical model for airfoil aerodynamic characteristics over the entire 360 degrees angle of attack range", *Journal of Renewable and Sustainable Energy*, vol. 12, no. 033303, pp. 1–16, 2020.

[19] M. H. Snyder, W. Wentz, and A. Ahmed, "Wer-16: Two-dimensional tests of four airfoils at angles of attack from 0 to 360 degrees", Wichita State University, Center for Energy Studies., Tech. Rep., 1984.

[20] J. Zhong and W. Chen, "Transition characteristics for a small tail-sitter unmanned aerial vehicle", *Chinese Journal of Aeronautics*, vol. 34, no. 10, pp. 220–236, 2021.

[21] E. A. Islas-Narvaez, J. F. Ituna-Yudonago, L. E. Ramos-Velasco, M. A. Vega-Navarrete, and O. Garcia-Salazar, "Design and determination of aerodynamic coefficients of a tail-sitter aircraft by means of cfd numerical simulation", *Machines*, vol. 11, no. 17, pp. 1–24, Jan. 2023.

[22] K. Anuar, W. Fatra, A. Asral, N. Nazaruddin, and M. Taslim, "Preliminary design of tail-sitter UAVs", in *3rd Conference on Innovation in Technology and Engineering Science (CITES)*, AIP Publishing, vol. 2891, May 2022, pp. 1–11.

[23] E. A. Tal and S. Karaman, "Global trajectory-tracking control for a tailsitter flying wing in agile uncoordinated flight", in *AIAA Aviation 2021 Forum*, AIAA, Jul. 2021, pp. 1–20.

[24] J. Wang et al., "Vectored-thrust system design for a tail-sitter micro-aerial-vehicle with belly/back takeoff ability", *Aerospace Science and Technology*, vol. 155, p. 109 542, 2024.

[25] A. Oosedo, S. Abiko, A. Konno, and M. Uchiyama, "Optimal transition from hovering to level-flight of a quadrotor tail-sitter uav", *Autonomous Robots*, vol. 41, pp. 1143–1159, 2017.

[26] X. Lyu, H. Gu, J. Zhou, Z. Li, S. Shen, and F. Zhang, "A hierarchical control approach for a quadrotor tail-sitter vtol uav and experimental verification", in *2017 IEEE/RSJ International Conference on Intelligent Robots and Systems (IROS)*, IEEE, 2017, pp. 5135–5141.

[27] R. Ritz and R. D'Andrea, "A global controller for flying wing tailsitter vehicles", in *2017 IEEE International Conference on Robotics and Automation (ICRA)*, IEEE, May 2017, pp. 2731–2738.

[28] E. Tal, G. Ryou, and S. Karaman, "Aerobatic trajectory generation for a vtol fixed-wing aircraft using differential flatness", *IEEE Transactions on Robotics*, vol. 39, no. 6, pp. 4805–4819, Dec. 2023.

[29] G. Lu, Y. Cai, N. Chen, F. Kong, Y. Ren, and F. Zhang, "Trajectory generation and tracking control for aggressive tail-sitter flights", *The International Journal of Robotics Research*, vol. 43, no. 3, pp. 241–280, 2024.

[30] K. F. McIntosh, S. Mishra, and J.-P. Reddinger, "Aerodynamic feedforward-feedback architecture for tailsitter control in hybrid flight regimes", *Journal of Guidance, Control, and Dynamics*, pp. 1–12, Jun. 2024.

[31] E. J. Smeur, M. Bronz, and G. C. de Croon, "Incremental control and guidance of hybrid aircraft applied to a tailsitter unmanned air vehicle", *Journal of Guidance, Control, and Dynamics*, vol. 43, no. 2, pp. 274–287, 2020.

[32] L. L. M. Veldhuis, "Propeller wing aerodynamic interference", *TU Delft Repository*, 2005.

[33] F. M. Catalano, "On the effects of an installed propeller slipstream on wing aerodynamic characteristics", *Acta Polytechnica*, vol. 44, no. 3, 2004.

[34] X. Chen, Z. Zhou, and W. Hongbo, "Investigation on approach to control lift distribution of wing by distributed propellers", in *Proceedings of the 31st Congress of the International Council of the Aeronautical Sciences, Belo Horizonte, Brazil*, 2018, pp. 9–14.

2

Wind Tunnel Tests of a Wing across Full 360° Angle of Attack Range

Following the introduction in Chapter 1, which outlines the challenges of controlling hybrid VTOL tailsitters, this chapter focuses on the aerodynamic characterization of a representative tailsitter wing. To address the lack of open-access aerodynamic data at high angles of attack (AoAs), a series of wind tunnel experiments were conducted across the full $360°$ *angle of attack range under varying flap deflections and throttle settings. Results reveal that flap deflections significantly influence lift, with stall occurring at both* $\pm 15°$ *and* $\pm 160°$ *AoA. The effect of propeller-wing interaction is strongly nonlinear and depends on AoA, airspeed, thrust, and flap angle. Under reverse flow, flap-induced pitch moments invert, though this can be mitigated by increasing the propeller thrust. Control effectiveness is highest near* $0°$ *AoA and is more sensitive to initial flap deflections than to large deflections. All data are published with open access to support further modeling and control design efforts.*

This chapter is based on the following article and data set:
Z. Ma, E.J.J. Smeur, G.C.H.E. de Croon, *Wind tunnel tests of a wing at all angles of attack*, International Journal of Micro Air Vehicles **14**, 17568293221110931 (2022).
Z. Ma, E.J.J. Smeur, *Wind tunnel data set with a wing at all angles of attack*, 4TU.ResearchData. dataset..

2.1. Introduction

In the family of unmanned aerial vehicles (UAVs), hybrid drones are becoming a research hotspot. Fixed-wing drones offer high endurance, long range, and high speed, while rotorcraft feature high agility, hovering and vertical take-off/landing (VTOL) capabilities. A hybrid drone integrates the advantages of both and is capable of hovering as well as using its wing for fast forward flight. Currently, four types of hybrid drones are being intensively studied[1]: the quadplane, the tilt-rotor, the tilt-wing, and the tailsitter. Among these types, the tailsitter stands out for its endurance and simple mechanisms. Potentially, tailsitters can be used in many societal applications, such as package delivery, exploration in complex environments and take-off/landing from a ship. However, in reality, there are still many challenges in the airframe design and control of tailsitters, especially when dealing with tailsitters' highly nonlinear aerodynamics and the impact of inverse flow in the descending phase.

Faced with these challenges, many studies have been carried out in recent years. Li et al.[2] proposed a nonlinear robust controller to handle the high nonlinearities, based on a nominal model and a nonlinear disturbance observer to compensate the uncertainties. Flores et al.[3] implemented a recurrent neural network for the estimation of highly nonlinear aerodynamic terms during the transition stage. Due to the difficulty of modeling highly nonlinear tailsitters, Barth et al. [4] proposed a model-free control algorithm to estimate and counteract the rapidly changing aerodynamic forces and moments with an intelligent feedback structure. In a similar fashion, Smeur et al. [5] proposed an incremental nonlinear dynamic inversion controller for the attitude and position control. Although many studies have focused on the high non-linearity of tailsitters, few of them take the inverse flow in the descending phase into consideration.

Considering the difficulty of accurately modeling the nonlinear aerodynamic forces, moments and the propeller–wing interaction of tailsitters at large angle of attack, wind tunnel tests provide a practical way to obtain reliable aerodynamic data. Fratello et al.[6] conducted experiments with both propeller-wing and nacelle-wing configurations at low subsonic speeds and the test results illustrated the interaction of the propeller, the nacelle and the wing. Gamble et al.[7] analyzed the propeller–wing interaction of a 24-inch span flexible-wing micro air vehicle using a combination of static bench tests and low-speed wind-tunnel measurements. Their results showed that 12–18% of the propeller thrust was converted into additional airframe drag when the wing was placed close to the propeller (at an axial spacing

of 0.17 D, where D is the propeller diameter), under zero-freestream, low-Reynolds-number conditions. Stoll[8], Hrishikeshavan[9], and Ananda[10] successively explored the aerodynamic characteristics of propeller-blown wings with distributed electric propulsion, under different experimental conditions. Since the range of the angle of attack (AoA) is confined to -16 to 20 degrees in the NACA4412 airfoil data[11], Kubo et al.[12] used the modified NACA0012 airfoil data[13] to interpolate for the angle of attack range that is not available for their main wing, the NACA4412 airfoil[11]. Lyu et al.[14] conducted a wind tunnel test to characterize the full envelope aerodynamics of a tailsitter UAV and showed the results of calculated aerodynamic coefficients. Truong et al.[15] presented a semi-empirical model of the aerodynamic coefficients of airfoils in the full range of angle of attack. Snyder et al.[16] presented the characteristics of four airfoils tested in the two-dimensional wind tunnel at the AoA from 0 to 360° and deflected the aileron of NACA 23024 airfoil from -60° to 60°. Results of their aileron study show that it's ineffective to deflect the aileron above 20°. The metadata is published together with the report. Nevertheless, the knowledge of the tail-sitter's aerodynamic model covering the full range of angle of attack is generally absent for low-cost UAVs[14], and only few data sets have recorded the impact of different flap deflections and throttle settings on the aerodynamics of a wing with or without propellers.

The main contribution of this chapter is an open-published wind tunnel test data set[17] that contains the aerodynamic data of a wing with and without spinning propellers for different flap deflections across the full angle of attack range, which is the first one of its kind. It is important to note that most published studies focus on two-dimensional airfoil aerodynamics, where the angle of attack is defined at the section level. In contrast, the present work investigates a finite-span three-dimensional wing, for which the measured angle of attack refers to the geometric orientation of the wing as a rigid body. Multiple tests were performed with different flap deflection angles for 0%, 50% and 70% throttle settings, where throttle settings represent the PWM command percentages sent to the motor controllers. In the present experiments, the propellers are driven using a fixed PWM-based throttle command as widely used on many UAVs, and no direct thrust or torque measurements are available. Therefore, the throttle setting is used here as a control input variable rather than as a direct physical parameter. The objective of this study is to experimentally characterize the resulting force and moment acting on the wing under different actuator command levels. To the best of the author's knowledge, no open-access dataset in the literature provides aerodynamic measurements across

the full 360° angle of attack range, combined with multiple propeller thrust settings and multiple flap deflections, for a wing configuration representative of VTOL tailsitters. The presented dataset therefore fills an important gap in available experimental data. Moreover, the wing-propeller interaction, the impact of inverse flow and the control effectiveness of flaps are also studied in this chapter based on the measured data.

This chapter is structured as follows. A description of the conducted experiments and a data set format are given first. After that, the data collected under different flap deflection, airspeed and throttle settings are presented. Then, the wing-propeller interaction, the influence of inverse flow and the control effectiveness are discussed. Finally, conclusions are drawn based on the aforementioned analysis.

2.2. Experiment setup and measurements

2.2.1. Experiment setup

The data were collected from multiple wind tunnel tests, all of which were conducted at the Open Jet Facility (OJF) at Delft University of Technology in February 2021. The OJF is a low-speed closed circuit wind tunnel situated in a large room with a width of 13 m and a height of 8 m. The octagonal outlet right before the test section is 2.85 m in width and 2.85 m in height. The maximum velocity in the test section is about 35 m/s. According to the facility specification, the OJF settling chamber is equipped with a honeycomb flow rectifier and five wire-mesh screens, which reduce spatial velocity deviations to below 0.5% at two meters downstream of the outlet and lower the longitudinal turbulence intensity to below 0.24%. Although the open-jet configuration introduces some spatial and temporal variations in the inflow, the resulting flow quality is adequate for the aerodynamic force and moment measurements carried out in this study. For the OJF-balance, the difference between the known applied loads and the back calculated loads are errors. The maximum and the standard deviation of the errors are presented in percentage of the nominal loads in Table 2.1[1]. The sampling frequency of the balance is 100 Hz.

The airfoil of the wing used for the wind tunnel tests is modified from the MH32 asymmetric airfoil[19], whose geometry is shown in Figure 2.2. The wingspan is 1 m. The wing has some taper, such that its chord is 0.25 m at the root and 0.2 m at

[1]The errors of OJF-balance are listed in a NLR-CR-2008-695 documentation from Netherlands Aerospace Centre[18]

Table 2.1: Maximum and standard errors of OJF-balance (expressed as percentage of nominal loads)

	MAX (%)	STDEV (%)
ΔF_x	0.06	0.02
ΔF_y	0.23	0.05
ΔF_z	0.16	0.05
ΔM_x	0.05	0.01
ΔM_y	0.05	0.01
ΔM_z	0.25	0.07

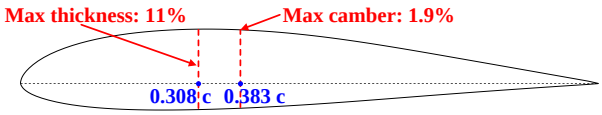

Figure 2.1: The cross section of the test wing.

the tip. The distance between each motor is 0.4 m, and the control surface width is 0.05 m. The labeled picture of the wing's cross section is shown in Figure 2.1. c refer to the chord of the respective cross section of the airfoil. The max thickness is 11% at 30.8% chord and the max camber is 1.9% at 38.3% chord. The two flaps on the wing are connected to servos that change the flap deflections. The maximum flap deflection angle is 38° each way. In this chapter, upward deflections are defined as positive values. The wing is equipped with three brushless DC motors (BLDC) of the type T-MOTOR MN3510-25 360 KV. The speed of the motors depends on the throttle setting of a BLHeli_32 electronic speed controller (ESC). The throttle setting is defined as a normalized percentage variable. During the experiment, this variable is implemented via a PWM signal applied to the ESC, with a pulse width ranging from 1000 µs to 2000 µs over the full throttle range. The propellers used in the tests are APC 13×10-inch propellers, with a diameter of 0.3302 m and a pitch of 0.254 m, and their manufaturer-provided performance data are available at[20]. The two propellers near the tip and root of the wing rotate in the same direction, while the propeller in the middle rotates in the opposite way.

Normally, wind tunnel experiments with half a wing would include a sidewall at the root of the wing that would prevent a root vortex there and reduce root-loss effects arising from three-dimensional flow leakage at the root. In this experiment, the sidewall is absent, which allows the development of root vortex formation and associated upwash and downwash, and may therefore influence the local aerodynamic loading near the root. However, since the main focus of the experiments

was to figure out the impact of flap deflections and throttle settings on the wing's dynamics instead of the absolute values of lift, drag and moment, the influence of root-loss effects is therefore considered as a systematic bias rather than a configuration dependent distortion and it is still feasible and meaningful to make comparable analysis between different flap deflections even with the absence of the sidewall.

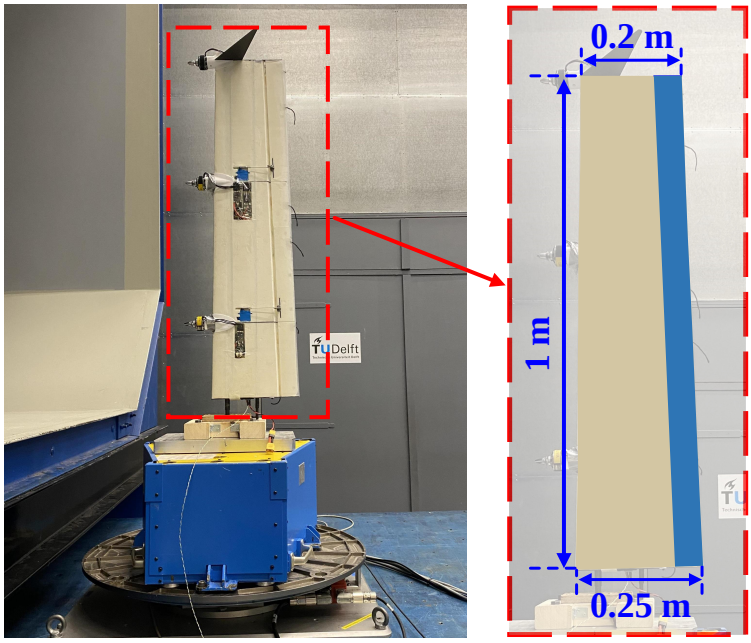

Figure 2.2: Side view of experiment setup without propellers.

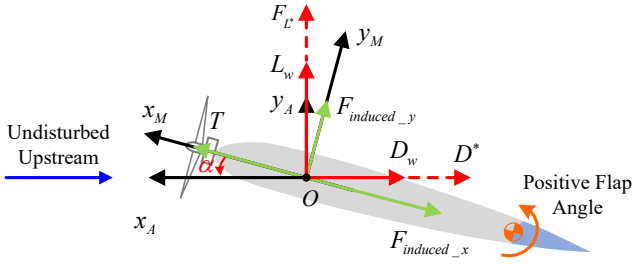

Figure 2.3: The measurement coordinate frame and the air coordinate frame from the top view. The blue arrow shows the direction of undisturbed upstream generated from the wind tunnel, and the orange arrow shows the positive deflection angle of the flap.

Figure 2.3 presents a top view of the measurement coordinate frame $x_M O y_M$

and the aerodynamic coordinate frame $x_A O y_A$. Both coordinate frames are right-handed. The experimental setup is shown in Figure 2.2. The wing is fixed on a six-axis forces and moments balance, which is mounted on a turntable, allowing a rotation of 360 degrees. All forces and moments are measured by the six-axis balance and are referenced to the balance center. For illustration purposes, the origin of the measurement and aerodynamic coordinate frames is shown on the wing, which corresponds to the vertical projection of the balance center onto the wing. This projected reference point is located chord-wise 0.018 m ahead of the root quarter-chord. The definitions of the force and moment components are provided and discussed in Section 2.3.1.

2.2.2. Measurements

To eliminate any measurement offsets, a calibration data set was first collected with no wind tunnel airflow by rotating the balance table together with the wing fixed on it for the full 360°. These calibration data were used to compensate for sensor bias and orientation dependent zero offsets of the six-axis balance prior to force and moment analysis. Then, for each measurement, the following procedure was followed. The airspeed was set as 3 m/s initially and increased with intervals of 3 m/s, until a maximum of 15 m/s. The wind tunnel airspeed is not closed loop controlled, and slight variations from the desired airspeed occur depending on the flow resistance in the test section. The actual airspeed is recorded continuously for each experiment. The average deviation between the actual airspeed and the desired airspeed is 0.8 m/s for 0% and 70% throttle settings, and 0.2 m/s for 50% throttle setting. Compared to the value of the desired airspeed, the deviation is much smaller and its influence is assumed to be negligible.

At each airspeed, the wing was rotated 360° at a speed of 2° per second, such that all possible AoA are covered. Based on experience with the Nederdrone [21], equipped with wings of this kind, a throttle setting corresponding to approximately 60% of the available PWM command range is typical during the hover and transition phase. To investigate the effect of the throttle, the experiment was performed with 50% throttle, 70% throttle and once without propellers mounted. For these three different throttle settings, the experiments were performed with various flap deflections: no flap deflection, 50% flap down, 50% flap up, 100% flap down and 100% flap up. It is worth mentioning that the motor stopped twice for an instant during the measurement for 50% throttle with 50% upward flap deflection, which is shown in Figure 2.7 as two small spikes. The available measurements from the wind

tunnel tests are listed in Table 2.2 and a an overview of the performed experiments is given Figure 2.4.

Table 2.2: List of available data from the wind tunnel tests

Measurements	Nomenclature
Time	t [s]
Force (measurement X-axis)	F_{X_M} [N]
Force (measurement Y-axis)	F_{Y_M} [N]
Force (measurement Z-axis)	F_{Z_M} [N]
Moment (measurement X-axis)	M_{X_M} [N·m]
Moment (measurement Y-axis)	M_{Y_M} [N·m]
Moment (measurement Z-axis)	M_{Z_M} [N·m]
RPM (wind tunnel)	rpm
Temperature	temp [°C]
Atmospheric pressure	P [Pa]
Differential pressure	dP [Pa]
Airspeed	V [m·s^{-1}]
Dynamic pressure	q [Pa]
Angle of attack	α [deg]

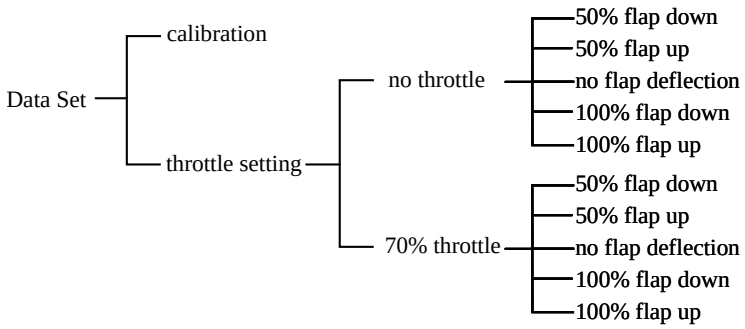

Figure 2.4: Structure of the published wind-tunnel dataset, organized by throttle setting and flap deflection.

2.3. Descriptions of the collected data

2.3.1. Forces and moments

Since the pitching moment is usually regarded as the most important moment in tailsitter research[22], the force components in the lift and drag directions, together with the pitching moment will be our main focus in this chapter.

As is shown in Figure 2.3, L_w and D_w represent the lift and drag of the wing measured with no propellers installed and no motor rotation, such that only the undisturbed upstream acts on the wing, T is the propeller thrust, and $F_{induced_x}$ and $F_{induced_y}$ are the forces induced by the propeller slipstream in the x_M and y_M axes, where the subscript M denotes the measurement coordinate frame $x_M O y_M$. F_{L^*} and F_{D^*} are defined as the projections of the measured force vector onto the positive y_A-axis and the negative x_A-axis, respectively, thereby accounting for the combined effects of the undisturbed upstream and propeller-induced flow. M is the pitching moment, and together with the forces F_{L^*}, F_{D^*} it can be calculated from the measurements by Equation (2.1).

$$\begin{aligned} F_{L^*} &= F_{X_M} \sin\alpha + F_{y_M} \cos\alpha \\ F_{D^*} &= -F_{X_M} \cos\alpha + F_{y_M} \sin\alpha \\ M &= M_z \end{aligned} \tag{2.1}$$

When the throttle setting is 0% and the propellers are not mounted, no thrust or propeller-induced slipstream is present. In this case, the measured forces, when resolved into the aerodynamic coordinate frame $x_A O y_A$, represent the aerodynamic loads induced solely by the undisturbed upstream, and therefore

$$\begin{aligned} L_w &= F_{L^*} \\ D_w &= F_{D^*} \end{aligned} \tag{2.2}$$

Accordingly, the aerodynamic coefficients of the wing can be calculated by Equation (2.3).

$$\begin{aligned} C_L &= \frac{L_w}{\frac{1}{2}\rho S V^2}, \\ C_D &= \frac{D_w}{\frac{1}{2}\rho S V^2}, \\ C_M &= \frac{M}{\frac{1}{2}\rho S V^2 c_a}. \end{aligned} \tag{2.3}$$

where ρ is the air density, S is the wing area, c_a is the mean aerodynamic chord and V refers to the undisturbed upstream velocity.

When the throttle setting is not 0%, in the aerodynamic coordinate frame $x_A O y_A$, apart from the aerodynamic forces L_w and D_w generated by the undisturbed upstream, the wing is also subjected to the propeller thrust T, and the force induced

by the propeller slipstream $F_{induced}$. By vector decomposition, F_{L^*} and F_{D^*} can be described by Equation (2.4).

$$\begin{aligned} F_{L^*} &= L_w + T\sin\alpha - F_{induced_x}\sin\alpha + F_{induced_y}\cos\alpha \\ F_{D^*} &= D_w - T\cos\alpha + F_{induced_x}\cos\alpha + F_{induced_y}\sin\alpha \end{aligned} \tag{2.4}$$

In the present study, the undisturbed freestream velocity of the wind tunnel is consistently selected as the reference velocity for normalization. Accordingly, the normalized coefficients C_{L^*} and C_{D^*} are defined with respect to the resultant forces F_{L^*} and F_{D^*}. It should be noted that F_{L^*} and F_{D^*} are not purely aerodynamic forces, as they include thrust-related components and contributions induced by the propeller slipstream. Therefore, C_{L^*} and C_{D^*} should be regarded as normalized dimensionless force coefficients rather than conventional aerodynamic coefficients.

2.3.2. Measurement validation

Since the test wing is a modified MH32 airfoil, within the AoA before the stall, we compared its lift coefficients at low Reynolds number to those of mh32-il airfoil in UIUC Airfoil Coordinates Database, as is shown in Table 2.3. In this table, the lift coefficient of our wing with no flap deflection is selected. The deviation in the values is predictable due to the different thickness and camber of the airfoil. Even if a deviation exists in the absolute values, it is found that the lift coefficients of the tested wing and the MH32-il airfoil are both approximately linear w.r.t. to the angle of attack with a similar trend in the pre-stall region.

Table 2.3: Comparison between test wing and MH32-il airfoil

	MH32-il[23]	Tested modified MH32
Max thickness	8.7%	11%
Max camber	2.3%	1.9%
α_{stall}	10°	14°
$C_L(\alpha = -5°)$	−0.4	0.07
$C_L(\alpha = 0)$	0.2	0.24
$C_L(\alpha = 5°)$	0.8	0.55
$C_L(\alpha_{\text{stall}})$	1.06	0.94

To validate the accuracy of measurements, we also conducted the repeated experiments for 0% throttle setting on two consecutive days respectively. Taking the repeated measurements for 0% throttle and $-19°$ flap deflection as an example, the resultant lift coefficients calculated from non-filtered data on two days keep

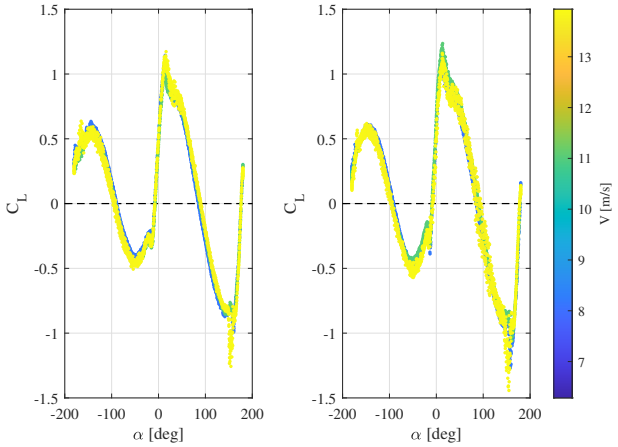

Figure 2.5: C_L for $-19°$ flap deflection (propellers removed, 0% throttle setting) from two repeated tests.

high consistency in the trend and values, as is shown in Figure 2.5. The colorbar in the figure represents the undisturbed freestream velocity. Since, for a fixed model geometry and air properties, variations in airspeed correspond directly to changes in Reynolds number, the figure therefore indicates that the resultant aerodynamic lift coefficient exhibits only weak sensitivity to Reynolds number within the tested range. Consequently, Reynolds-number effects can be considered negligible under the present experimental conditions.

2.3.3. Influence of flap deflection

For 0% throttle, no thrust is generated and no propeller-induced slipstream is present. As a result, the flow over the wing is solely determined by the undisturbed wind-tunnel freestream. Figure 2.6 displays the aerodynamic coefficients C_L, C_D and C_M of the wing for different flap deflections. The feature of our data set is that the measurements cover the full $360°$ AoA.

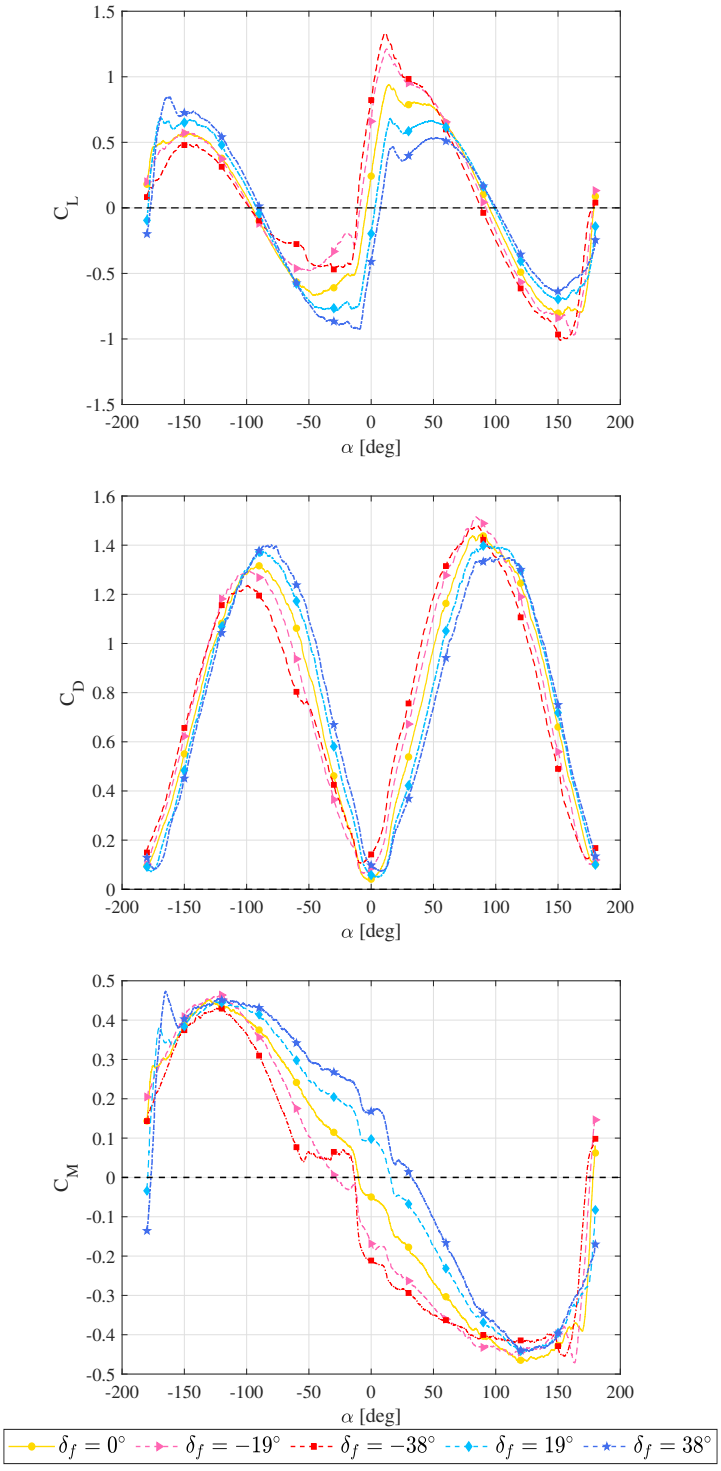

Figure 2.6: Aerodynamic coefficients C_L, C_D and C_M for different flap deflection (0% throttle setting).

It can be observed from Fig. 2.6 that upward and downward flap deflections influence the aerodynamic coefficients in an approximately symmetric but opposite manner. Increasing flap deflection magnitude strengthens its effect on all three coefficients. Within the linear operating range of angle of attack (-15° to 15°), the lift coefficient is well described by a first-order Taylor expansion in terms of C_{L_0}, C_{L_α}, and C_{L_δ}, confirming the validity of the conventional linear lift model in this regime. Within the -70° to 70° AoA range, downward flap deflections contribute to the larger value of C_L, whereas the opposite trend is observed in the reverse-flow region (-160° to -70° and 70° to 160°). In addition to the classical stall occurring near $\pm 10^\circ$, secondary stall features are observed at approximately $\pm 160^\circ$, corresponding to the onset of inverse flow conditions. Furthermore, the pitching moment coefficient attains extreme values near $\pm 160^\circ$, with downward and upward flap deflections producing opposite peak moments, reflecting the fundamental change in aerodynamic loading under reversed flow.

2.3.4. Influence of throttle setting

Figure 2.7 shows the dimensionless force coefficients C_{L^*} and C_{D^*} for 0%, 50% and 70% throttle settings at an undisturbed upstream airspeed of 12 m/s. Compared with flap deflection, the throttle setting which reflects thrust level, is the dominant factor affecting both C_{L^*} and C_{D^*} over the entire angle of attack range. As the throttle setting increases, both C_{L^*} and C_{D^*} exhibit systematic changes in peak magnitude, indicating a substantial modification of the wing aerodynamics by the propeller induced slipstream. In contrast to the zero throttle case, where the trends are mainly governed by freestream aerodynamics, the presence of propeller inflow under 50% and 70% throttle settings significantly alters the effective local angle of attack and dynamic pressure on the wing. The propeller wake reshapes the aerodynamic response over a wide range of α, extending the range of angles over which C_{L^*} increases with α. This behavior reflects the dominant role of the propeller slipstream in redefining the overall force characteristics. At $\alpha = 0^\circ$, for 50% and 70% throttle settings, the thrust component directly opposes the freestream drag, leading to negative values of C_{D^*} when the thrust exceeds the aerodynamic drag.

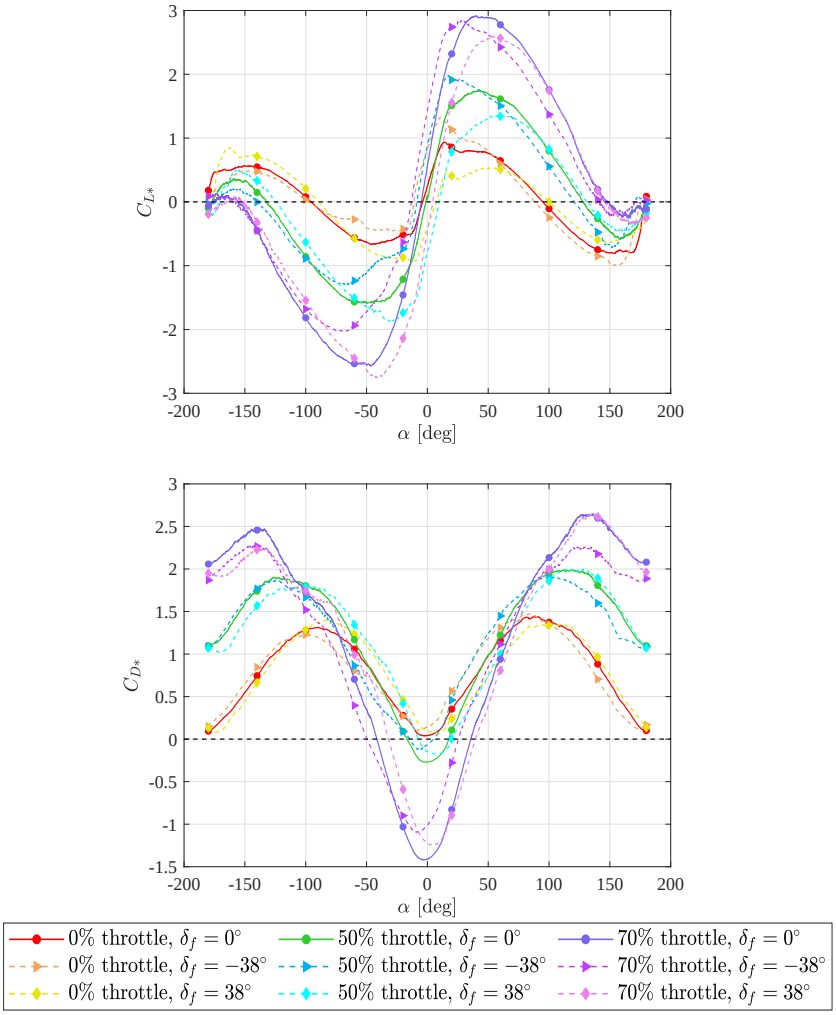

Figure 2.7: C_{L^*} and C_{D^*} for 0%, 50%, 70% throttle settings, for different flap deflections at 12 m/s undisturbed upstream airspeed.

2.3.5. Influence of airspeed

Figure 2.8 shows the pitching moment M measured at different undisturbed upstream airspeeds for both 0% and 70% throttle settings. In this section, the influence of airspeed is examined specifically in terms of the dimensional pitching moment, since from a flight-control perspective, the magnitude of the available absolute moment directly determines control authority.

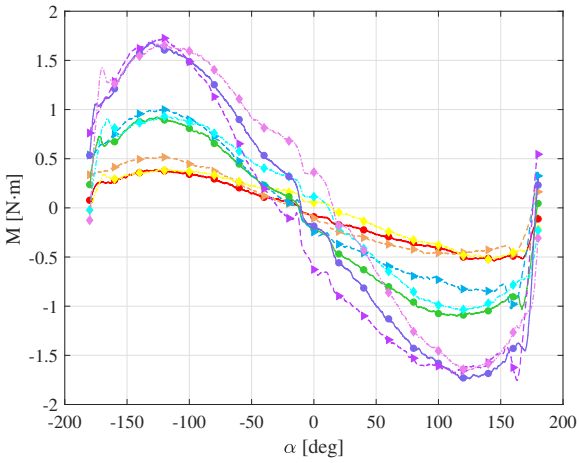

(a) 0% throttle

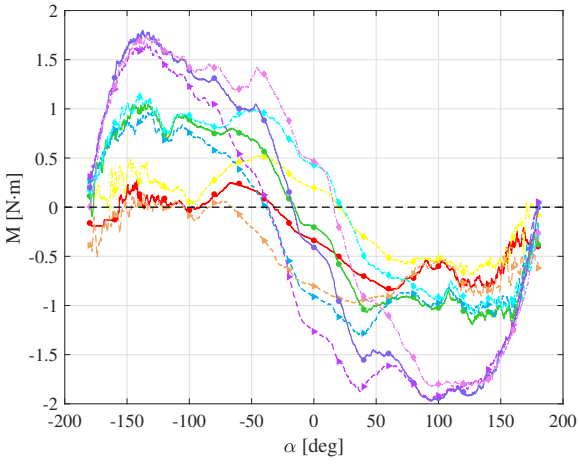

(b) 70% throttle

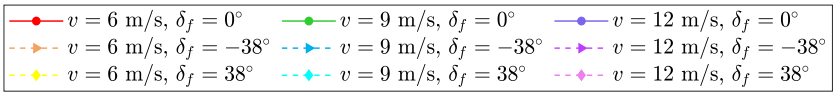

Figure 2.8: M at different airspeeds for respective 0% and 70% throttle settings.

For both throttle settings, an increase in undisturbed upstream airspeed leads to a consistent growth in the peak magnitude of the pitching moment over a wide range of angles of attack (approximately $-120°$ to $120°$), indicating a clear dynamic-pressure scaling of aerodynamic loads. At very large angles of attack approaching $\pm 180°$, however, the influence of freestream airspeed becomes significantly

weaker, where the pitching moment decreases substantially in magnitude and even exhibits a sign reversal. From a control perspective, this highlights that freestream airspeed is a critical parameter when assessing pitching authority in normal operating conditions, whereas its effect diminishes near fully reversed or reversed-flow configurations.

2.4. Discussion

In this chapter, key aerodynamic phenomena relevant to a tailsitter wing configuration are investigated based on wind-tunnel measurements. The discussion focuses on inverse-flow effects during vertical descent, aerodynamic interaction between the wing and the propeller slipstream, and flap control effectiveness across the full angle-of-attack range. Together, these effects determine the achievable moment authority and control performance across the flight envelope.

2.4.1. Inverse flow

During the hover phase of tailsitters, the dominant flow over the wing surface is usually the flow generated by the propellers. However, during vertical descent, the total rotor thrust is intentionally reduced, such that the propeller-induced slipstream weakens and the freestream becomes dominant. Under this condition, the incoming flow may approach the wing from the trailing edge direction, giving rise to a reversed flow (inverse flow) regime over the wing surface. As Figure 2.9 shows, when a tailsitter descends vertically, it will be affected by air flowing over the wing in reverse (inverse flow), which will affect the control effectiveness of the flaps. In this section, the influence of the inverse flow will be discussed.

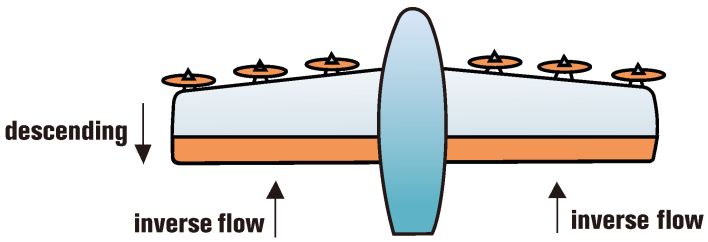

Figure 2.9: Schematic representation of a tailsitter equipped with the test wings in the descending phase.

It can be seen from Figure 2.10 that in our wind tunnel tests, when the AoA is

in the range of $-180°$ to $-90°$ and $90°$ to $180°$, the trailing edge of the wing will face towards the air flowing over the wing surface in reverse, which simulates the situation when the tailsitter encounters inverse flow.

Figure 2.11 shows the pitching moment M for the 0% and 70% throttle settings at 6 m/s airspeed, in which the plots have been filtered with a moving average filter compared to the moment at 6 m/s in Figure 2.8. Within the α range of $-90°$ to $90°$, the moment basically has the larger value with the upward deflected flaps for both 0% and 70% throttle settings. However, within the α range of $-180°$ to $-90°$ and $90°$ to $180°$, the wing is under the impact of inverse flow. For the 0% throttle setting, the air flowing over the wing is purely from the wind tunnel in the reversed direction. As is shown in Figure 2.11 (a), the value of the moment for 0% throttle is larger with downward deflected flaps than with upward ones within the α range of $-180°$ to $-90°$ and $90°$ to $180°$, which is just opposite to the case within $-90°$ to $90°$. It is also worth noting that within $-120°$ to $150°$ the upward flap deflection has little impact on the moment for 0% throttle. On the contrary, the propeller induced slipstream for 70% throttle is so strong that it is the dominant flow over the wing in a non-reversed direction. Within the full $360°$ AoA, the moment for 70% throttle always reaches a larger value with upward deflected flaps than with downward deflection. It can be concluded that when the air flowing over the wing is reversed, the flap deflections will affect the pitch moment in an opposite way compared to the non-reversed case, but this kind of opposite effect can be prevented by increasing the throttle setting.

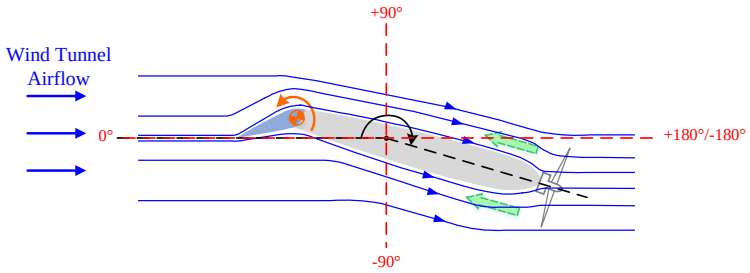

Figure 2.10: Schematic representation of the test wing under the influence of inverse flow from the top view.The blue arrows indicate the undisturbed upstream flow provided by the wind tunnel, while the green arrows represent the propeller-induced slipstream. This schematic does not depict the local resultant flow field, but rather illustrates the relative directions of the two contributing flow components for conceptual clarity.

2.4.2. Wing-propeller interaction

In research on tailsitter UAVs, the wing-propeller interaction constitutes a major source of nonlinear aerodynamic behavior. When the motors are on, a slipstream will be generated by the spinning propellers that significantly alters the velocity field over the wing, modifying both the effective angle of attack and the pressure distribution.

In conventional fixed-wing aerodynamics, lift is typically modeled using a linearized relation of the form $C_L = C_{L0} + C_{L\alpha}\,\alpha + C_{L\delta}\,\delta$, which is valid primarily in the flow regime before stall. However, in tailsitter configurations, especially under large angles of attack and strong propeller slipstream influence, the flow becomes highly non-uniform, rendering such linear models inadequate. Therefore, instead of relying on conventional aerodynamic modeling, this section focuses on quantifying the propeller-induced force increment by analyzing the difference in the measured force components along the measurement-frame y_M axis between the 0% throttle case and the corresponding 50% and 70% throttle cases over the full angle of attack range.

We assume that the propeller thrust does not influence the free-stream wind-tunnel speed. The wind tunnel does not have a closed-loop velocity controller, yet the influence of the propeller thrust is typically small. In the present experiments, the propellers are driven using a fixed PWM-based throttle command, and no direct thrust or torque measurements are available. Therefore, the throttle setting is used here as a control input variable rather than as a direct physical parameter. The objective of this study is to experimentally characterize the resulting force and moment acting on the wing under different motor command levels. For each airspeed, the experiments were conducted under different motor command levels applied to the propellers, specifically throttle settings in this study. Although an isolated propeller operating at non-zero angle of attack can generate normal forces and pitching/yawing moments, existing experimental and numerical studies [24] report that the normal force coefficient of isolated propellers under moderate inflow angles is typically significantly smaller than the axial thrust coefficient and is strongly dependent on inflow angle and advance ratio. The present analysis assumes that, in the tested configuration, the normal force contribution generated by the propellers alone is small compared with the forces induced on the wing by the propeller slipstream. Therefore, the change in the measured force along the y_M axis between powered and unpowered cases is primarily attributed to the aerodynamic force induced by the propeller slipstream acting on the wing.

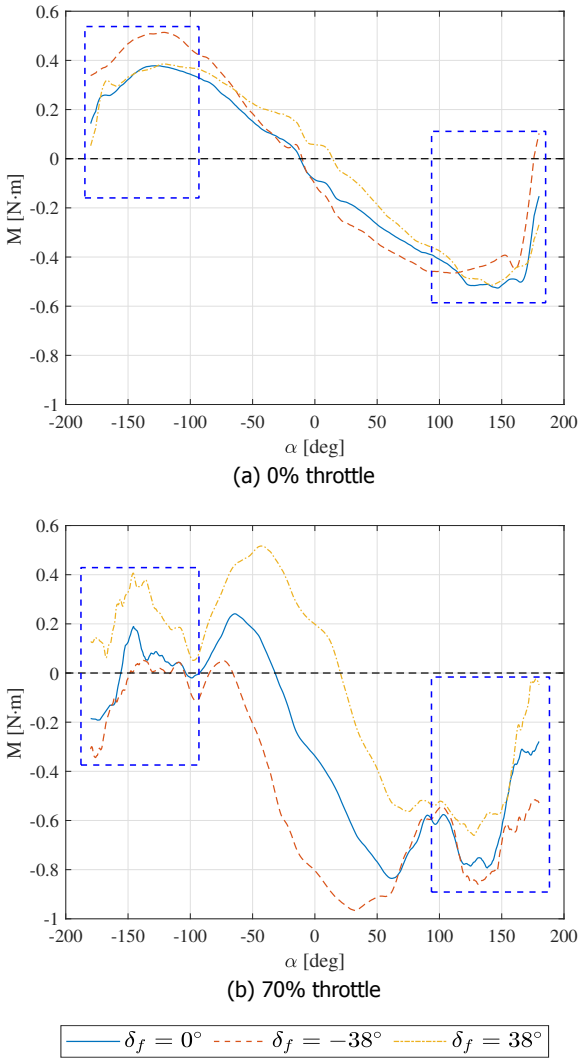

(a) 0% throttle

(b) 70% throttle

Figure 2.11: The pitching moment M for respective 0% and 70% throttle settings at 6 m/s airspeed.

To quantify this effect, the slipstream-induced force on the wing is defined as

$$F_{induced_y} = F_{diff} = F_{Y_{M_{motor}}} - F_{Y_{M_{0\%}}} \tag{2.5}$$

where $F_{induced_y}$ is the aerodynamic force generated by the propeller induced flow on the y_M axis, F_{diff} is the difference of the force measured on y_M axis, $F_{Y_{M_{motor}}}$ is the force measured on y_M axis for 50% or 70% throttle setting, and $F_{Y_{M_{0\%}}}$ is

the force measured on y_M axis for 0% throttle setting. From the measurements obtained by [25], we conclude that the force on the y_M axis induced by a propeller alone without the wing in oblique flow is small, which can be neglected compared to $F_{induced_y}$ acting on the wing.

2.4.3. Control effectiveness

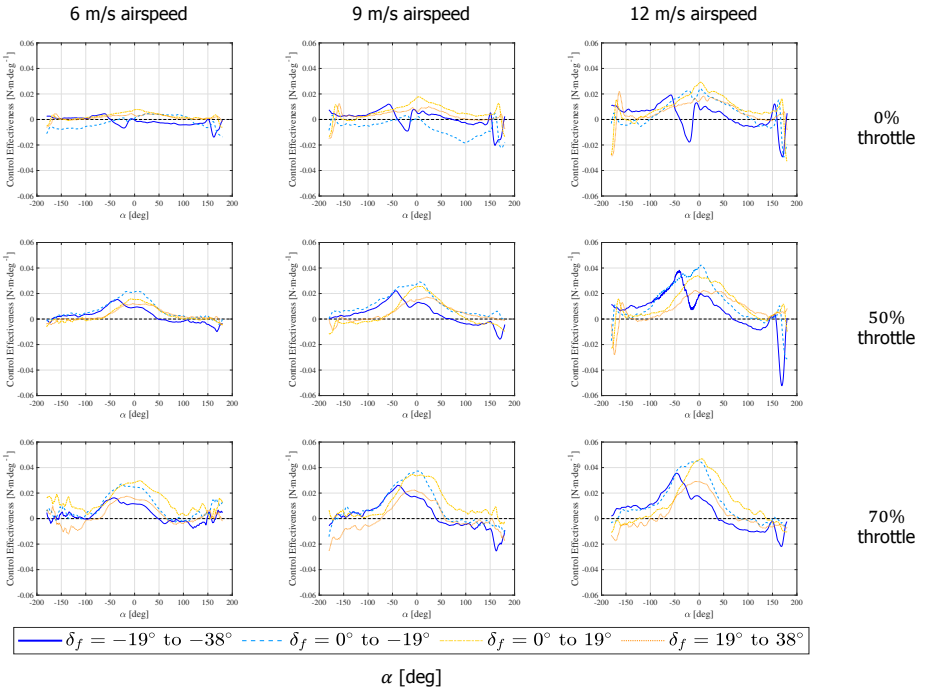

Figure 2.13: Control effectiveness of flap deflection under different throttle settings.

The control effectiveness refers to the the change in force or moment caused by a change in control input[5], which directly describes the control effect of actuators on the output. When the control effectiveness is zero, the corresponding control surface becomes ineffective. A change of its sign can potentially complicate the design of a stable controller. Hence, when trying to control a tailsitter drone, it is important to find out how the control effectiveness changes depending on the AoA, airspeed, flap deflection and throttle setting. Due to the discrete settings of the wind tunnel test conditions, only a finite set of flap deflection levels are available, and therefore the derivative is approximated using a finite-difference scheme. In this work, the control effectiveness is evaluated using a local finite difference ap-

proximation of the pitching moment with respect to the flap deflection, using the following equation

$$CE = \frac{\partial M}{\partial \delta_f} \approx \frac{\Delta M}{\Delta \delta_f} \tag{2.6}$$

where ∂M is the partial derivative of the moment, $\partial \delta_f$ is the partial derivative of flap deflection, ΔM is the moment change, and the $\Delta \delta_f$ is the change of flap deflection between two discrete operating points.

With flap deflections changed in four ways, Figure 2.13 displays the control effectiveness for 0%, 50% and 70% throttle settings at 6 m/s, 9 m/s and 12 m/s freestream airspeeds. From a control perspective, control effectiveness is determined by the achievable moment levels rather than by dimensionless coefficients. In this section, the freestream velocity is varied as an operating-condition parameter representative of different flight regimes to assess how the pitching control effectiveness scales with dynamic pressure. It can be observed that the control effectiveness generally gets higher with the increase of the throttle setting and airspeed and reaches the peak value around 0° AoA. This behavior can be explained by the fact that, around $\alpha \approx 0^\circ$, the flap is most effective in modifying the pressure distribution over the airfoil because the flow remains largely attached and the local flow direction is well aligned with the flap deflection. As a result, a change in flap deflection angle produces a prompt change in pitching moment, leading to a high control effectiveness. The control effectiveness is relatively lower around $\pm 180^\circ$ AoA. For each throttle setting, the observations of flap control effectiveness are described as follows.

For 0% throttle setting, the change of flap deflection has little impact on the control effectiveness at low airspeed and the effectiveness value is largest at 0° AoA with the flaps deflected from 0° to 19°. Ideally, the curve of the control effectiveness would be a flat horizontal line above zero. However, as the AoA changes to $\pm 180^\circ$, the value of control effectiveness decreases rapidly and the sign flips. Noticeably, when the flaps are deflected from -19° to -38°, sudden declines and rises appear in the curve of control effectiveness, respectively within the ranges of -50° to 0° and 150° to 180°. These drops are attributed to nonlinear aerodynamic effects arising from excessive flap deflection, where the moment contribution of the flap becomes strongly dependent on local flow attachment state.

For both the 50% and 70% throttle settings, the control effectiveness is basically higher around 0° AoA than at $\pm 180^\circ$ and attains a larger peak value with the increase of airspeed. For both upward and downward flap deflections, it is more effective

to deflect the flaps from $0°$ to $\pm 19°$ than from $\pm 19°$ to $\pm 38°$. For 50% throttle, the highest control effectiveness is achieved at $0°$ AoA by deflecting the flaps from $0°$ to $-19°$. For 70% throttle, it is both significantly effective to deflect the flaps from $0°$ to $\pm 19°$. Similar to the situation under 0% throttle setting, the control effectiveness also drops rapidly in the the ranges of $-50°$ to $0°$ and $150°$ to $180°$, especially for 50% throttle.

Overall, for different throttle settings and airspeeds, the change of flap deflections can make a big difference to the control effectiveness at small AoA. In other words, it is more effective to deflect the flaps around $0°$ AoA than at $\pm 180°$, which validates the common practice that it is usually very hard to control a tailsitter at large AoA, e.g. during its vertically descending phase. To control a tailsitter with spinning propellers, it is generally more effective to deflect the flaps from zero to halfway deflection than from halfway deflection to full deflection. This is attributed to the saturation of flow turning capability and the onset of local separation near the flap at large deflections, which limits further growth of aerodynamic moment.

2.5. Conclusion

This chapter describes aerodynamic data of a wing under different throttle setting and flap deflection conditions, measured from wind tunnel tests at all angles of attack (AoA).

The aerodynamic coefficients of the tested wing are analyzed based on the measurements for 0% throttle. It is found that flap deflections have a great impact on the lift, drag and moment coefficients. Within $-15°$ to $15°$ AoA, the lift coefficient is linearly related to the flap deflections and angle of attack, which is not the case for the rest of angles of attack. It is found that when sufficient thrust is provided, a clear stall can no longer be observed in the lift of the vehicle.

For 0% throttle setting, the pitch moment is more affected by changes in airspeed than changes in flap deflection at very large AoA. For the tested airfoil with spinning propellers, the flap deflections have a significant impact on the pitch moment within the AoA range from $-100°$ to $100°$.

For the full $360°$ AoA, the propeller induced force is dependent on the AoA, the flap deflections, airspeed and the thrust in a coupled and nonlinear way. It is not accurate to model a tailsitter by calculating only the collective force of the thrust and the aerodynamic lift, even if the propeller slipstream airspeed has been considered and added to the total speed.

When the air flowing over the wing is reversed, the flap deflections will affect

the pitch moment in an opposite way compared to the non-reversed case. This kind of opposite effect can be avoided by increasing the throttle setting.

The control effectiveness is an important term for the control of tailsitters, which depends on the AoA and flap deflection itself. It is more effective to deflect the flaps from 0° to $\pm 19^\circ$ than from $\pm 19^\circ$ to $\pm 38^\circ$. It is also found that the flap control effectiveness is usually highest around 0° AoA. In flight conditions involving high AoA and low throttle, the control effectiveness of the flaps can become close to zero or even negative. This makes control design for tailsitters challenging at high angle of attack, and during vertical descending flight. For a tailsitter drone, it could be promising to deflect the motors and propellers rather than flaps to achieve large control effectiveness of the pitch moment.

Moreover, it should be noted that the present wind-tunnel experiments are conducted under nominally steady and uniform inflow conditions, which do not explicitly account for unsteady atmospheric disturbances such as gusts. For lightweight UAVs, these unsteady effects can lead to pronounced load variations and may affect flight robustness in real-world operations. However, the purpose of the present study is not to reproduce atmospheric disturbances, but to establish a baseline understanding of the underlying force and moment behavior of a tailsitter wing configuration under different settings of airspeed and actuation across the full 360° angle of attack range. Therefore, although wind-tunnel testing may overpredict steady aerodynamic loads compared with real flight in gusty environments, it remains an essential step for identifying fundamental trends and nonlinear behaviors in a repeatable and controlled manner.

References

[1] A. S. Saeed, A. B. Younes, S. Islam, J. Dias, L. Seneviratne, and G. Cai, "A review on the platform design, dynamic modeling and control of hybrid uavs", in *2015 International Conference on Unmanned Aircraft Systems (ICUAS)*, IEEE, 2015, pp. 806–815.

[2] Z. Li, L. Zhang, H. Liu, Z. Zuo, and C. Liu, "Nonlinear robust control of tail-sitter aircrafts in flight mode transitions", *Aerospace Science and Technology*, vol. 81, pp. 348–361, 2018.

[3] A. Flores and G. Flores, "Transition control of a tail-sitter uav using recurrent neural networks", in *2020 International Conference on Unmanned Aircraft Systems (ICUAS)*, IEEE, 2020, pp. 303–309.

[4] J. M. Barth, J.-P. Condomines, M. Bronz, J.-M. Moschetta, C. Join, and M. Fliess, "Model-free control algorithms for micro air vehicles with transitioning flight capabilities", *International Journal of Micro Air Vehicles*, vol. 12, pp. 1–12, 2020.

[5] E. J. J. Smeur, M. Bronz, and G. C. H. E. de Croon, "Incremental control and guidance of hybrid aircraft applied to a tailsitter unmanned air vehicle", *Journal of Guidance, Control, and Dynamics*, vol. 43, no. 2, pp. 274–287, 2020.

[6] G. Fratello, D. Favier, and C. Maresca, "Experimental and numerical study of the propeller/fixed wing interaction", *Journal of Aircraft*, vol. 28, no. 6, pp. 365–373, 1991.

[7] B. J. Gamble and M. F. Reeder, "Experimental analysis of propeller-wing interactions for a micro air vehicle", *Journal of Aircraft*, vol. 46, no. 1, pp. 65–73, 2009.

[8] A. M. Stoll, "Comparison of cfd and experimental results of the leaptech distributed electric propulsion blown wing", in *15th AIAA Aviation Technology, Integration, and Operations Conference*, AIAA, 2015, pp. 1–9.

[9] V. Hrishikeshavan, C. Bogdanowicz, and I. Chopra, "Experimental investigation of performance of a wing-propeller system for a quad-rotor-biplane micro air vehicle", in *54th AIAA/ASME/ASCE/AHS/ASC Structures, Structural Dynamics, and Materials Conference*, AIAA, 2013, pp. 1–19.

[10] G. K. Ananda, M. S. Selig, and R. W. Deters, "Experiments of propeller-induced flow effects on a low-reynolds-number wing", *AIAA Journal*, vol. 56, no. 8, pp. 3279–3294, 2018.

[11] I. H. Abbott and A. E. Von Doenhoff, *Theory of wing sections: including a summary of airfoil data*. Courier Corporation, 2012.

[12] D. Kubo and S. Suzuki, "Tail-sitter vertical takeoff and landing unmanned aerial vehicle: Transitional flight analysis", *Journal of Aircraft*, vol. 45, no. 1, pp. 292–297, 2008.

[13] C. C. Critzos, H. H. Heyson, and R. W. Boswinkle Jr, "Aerodynamic characteristics of naca 0012 airfoil section at angles of attack from 0 degrees to 180 degrees", Langley Aeronautical Laboratory, Tech. Rep., 1955.

[14] X. Lyu, H. Gu, Y. Wang, Z. Li, S. Shen, and F. Zhang, "Design and implementation of a quadrotor tail-sitter vtol UAV", in *2017 IEEE international conference on robotics and automation (ICRA)*, IEEE, 2017, pp. 3924–3930.

[15] V. Truong, "An analytical model for airfoil aerodynamic characteristics over the entire 360 degrees angle of attack range", *Journal of Renewable and Sustainable Energy*, vol. 12, no. 033303, pp. 1–16, 2020.

[16] M. H. Snyder, W. Wentz, and A. Ahmed, "Wer-16: Two-dimensional tests of four airfoils at angles of attack from 0 to 360 degrees", Wichita State University, Center for Energy Studies., Tech. Rep., 1984.

[17] Z. Ma and E. J. J. Smeur, "Wind tunnel data set with a wing at all angles of attack", 4TU.ResearchData.Dataset, 2022.

[18] H. Alons, "Ojf external balance documentation", *Nationaal Lucht en Ruimtevaartlaboratorium*, 2008.

[19] A. G. Escobar-Ruiz, O. Lopez-Botello, L. Reyes-Osorio, P. Zambrano-Robledo, L. Amezquita-Brooks, and O. Garcia-Salazar, "Conceptual design of an unmanned fixed-wing aerial vehicle based on alternative energy", *International Journal of Aerospace Engineering*, vol. 2019, pp. 1–13, 2019.

[20] APC Propellers Inc., *13×10 electric propeller performance data*, https://www.apcprop.com/files/PER3_13x10.dat, Manufacturer performance data.

[21] C. De Wagter et al., "The NederDrone: A hybrid lift, hybrid energy hydrogen UAV", *International Journal of Hydrogen Energy*, pp. 1–16, Mar. 2021.

[22] B. Li, W. Zhou, J. Sun, C. Wen, and C. Chen, "Model predictive control for path tracking of a vtol tailsitter uav in an hil simulation environment", in *2018 AIAA Modeling and Simulation Technologies Conference*, AIAA, 2018, pp. 1–14.

[23] U. of Illinois at Urbana-Champaign, *Mh32 airfoil coordinates*, UIUC Airfoil Coordinates Database, Accessed: 2024-11-28, 2023. [Online]. Available: https://m-selig.ae.illinois.edu/ads/coord/mh32.dat.

[24] W. Khan and M. Nahon, "A propeller model for general forward flight conditions", *International Journal of Intelligent Unmanned Systems*, vol. 3, no. 2/3, pp. 72–92, 2015.

[25] B. Theys, G. Dimitriadis, P. Hendrick, and J. De Schutter, "Experimental and numerical study of micro-aerial-vehicle propeller performance in oblique flow", *Journal of aircraft*, vol. 54, no. 3, pp. 1076–1084, 2017.

3

Attitude Control of a Tilt-rotor Tailsitter Micro Air Vehicle Using Incremental Control

Building on the aerodynamic understanding established in Chapter 2, this chapter explores a control-oriented design for tailsitter micro air vehicles. Two-rotor configurations offer structural simplicity and efficient cruise but suffer from actuator saturation due to poor pitch control at high angles of attack. To address this, a novel tilt-rotor design is proposed using two tilting rotors as the sole control actuators. Incremental Nonlinear Dynamic Inversion (INDI) is applied for attitude control and validated through indoor and outdoor flight tests. Results show that thrust vectoring effectively prevents actuator saturation by enabling sufficient pitch moment generation. However, the absence of aerodynamic control surfaces leads to limited roll control in forward flight.

This chapter is based on the following article:
G.H.L.H. Lovell-Prescod, **Z. Ma**, E.J.J. Smeur, *Attitude control of a tilt-rotor tailsitter micro air vehicle using incremental control*, International Conference on Unmanned Aircraft Systems (ICUAS) (2023) pp. 842-849.

3.1. Introduction

In recent decades, Micro Air Vehicles (MAVs) have undergone significant advancements. Their applications have expanded widely, including infrastructure inspection, agricultural monitoring, and tasks related to reconnaissance and surveillance.[1]. Some of these missions require MAVs to be capable of hovering as well as fast-forward flight and the rapid transition between the two, which brings about the high demand for hybrid MAVs that combine the advantages of both fixed-wing aircraft and rotorcrafts. Among different kinds of hybrid MAVs, tailsitters are special for their way of transitioning between hovering and forward flight by pitching either up or down 90°, which allows them to use the same actuators in hover as well as forward flight.

Despite the rapid and promising development, traditional tailsitters are faced with the challenge of actuator saturation, which has been mentioned or alluded to in [2], [3] and [4]. During the forward flight, in addition to 'prop-wash' airflow from the propellers mounted on the leading edge, there is sufficient velocity-induced airflow over the flaps. However, in vertical flight, the velocity-induced airflow is nonexistent in the hovering case, low in the slow climb case and negative in the descent case, which degrades the flap control effectiveness compared to the forward flight phase. In [5], Ma et al. discovered from the wind tunnel tests of a wing that the flap control effectiveness is much lower at high angles of attack than around zero angles of attack, demonstrating that the flap control effectiveness is limited during the transition and the vertical descent. Consequently, the limited flap control effectiveness leads to potential actuator saturation. Therefore, Bronz [6] compared pitch moment generation with a trailing edge aerodynamic surface on a wing, compared to thrust vectoring with a rotor in front of the wing. For the configuration tested, the pitching moment generated through thrust vectoring was almost twice that produced by the same deflection of flaps. Inspired by using thrust vectoring for control moment generation, a novel configured tailsitter is proposed in this chapter, namely a tilt-rotor tailsitter.

The flight control of tailsitters is a well-studied subject. The high non-linearity of tailsitters makes accurate modeling difficult and resource-intensive. To avoid resource-intensive modeling, Incremental Nonlinear Dynamic Inversion (INDI), a sensor-driven control strategy, has been extensively employed in the control of tailsitter aircraft. Smeur et al.[2] demonstrated the application of INDI to both attitude and velocity control across the full flight envelope of a tailsitter, showing that robust control performance can be achieved primarily by identifying the mapping

between actuator commands and the corresponding control moments. This actuator effectiveness was experimentally determined through flight testing. Further implementations were presented by Yang et al.[3] and Tal et al. [7]. The former introduced a mathematical model to capture actuator effectiveness, while the latter adopted a simplified ϕ-theory-based aerodynamic model to relate control inputs and system states via flat outputs, enabling a fully nonlinear inversion framework. Due to low dependency on modeling, an INDI control law is also derived and implemented for the attitude control of the novel-designed tilt-rotor tailsitter.

The contribution of this chapter is the attitude control of a newly designed and built tilt-rotor tailsitter with the INDI control strategy and the validation of the control performance by flight tests, which also demonstrates alleviation of actuator saturation with the use of thrust vectoring. However, it is also found in this research that the proposed tilt-tailsitter with only leading-edge mounted motors for control moment generation has the drawback of unreliable roll control performance during the forward flight. This chapter is organized as follows. Section 3.2 presents the physical design of the proposed tilt-rotor tailsitter. Section 3.3 details the derivation and adaptation of the INDI control law, including actuator dynamics and implementation considerations. Section 3.4 provides both indoor and outdoor flight test results, while Section 3.5 offers a discussion focused on actuator saturation. Finally, Section 3.6 concludes the chapter and outlines directions for future research.

3.2. Vehicle Design

3.2.1. Platform Configuration

Figure 3.1 shows a picture of the designed and built tilt-rotor tailsitter. Similar to the traditional tailsitters presented in [2], [3], [4], [7], [8], [9], this proposed tilt-rotor tailsitter has two motors mounted on its wing's leading edge. Instead of having aerodynamic control surfaces, the vehicle is equipped with servos to tilt the two motors individually. Figure 3.1 defines the body axis system for the tilt-rotor tailsitter, with the Euler angles ϕ, θ and ψ defined with respect to the hovering condition shown in the figure. Throughout this paper, the ZXY Euler rotation sequence is employed to prevent singularities that occur at pitch angles of $\pm 90^{\circ}$[2]. The left and right thrust in Newton are denoted T_l and T_r respectively, and the left and right tilt angles in radians are denoted δ_l and δ_r respectively. With these four actuators, four Degrees of Freedom (DOFs) can be controlled.

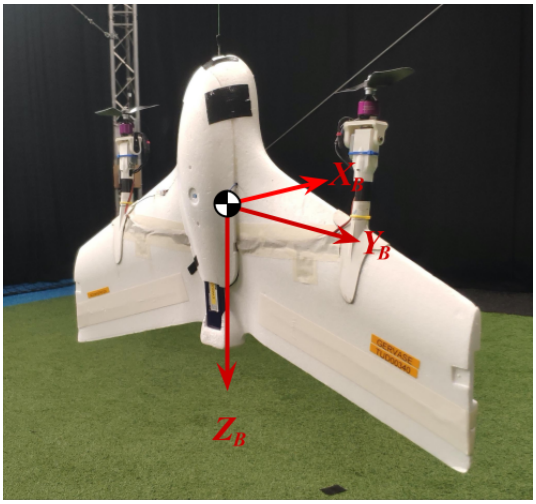

Figure 3.1: Body axis system of the tilt-rotor tailsitter.

Table 3.1: Inventory of build components

Component	Name	Qty.
Autopilot	mRo Pixracer R15	1
Motor	Hacker motors A20-20L EVO kV1022	2
ESC	T-motor F35A 3-6s	2
Servo	MKS HV9767	2
GPS	GPS NEO-M8N BDS Compass	1
Battery	Turnigy 3300mAh 4S 25C LiPo	1

3.2.2. Physical specifications

The airframe of the tilt-rotor tailsitter is the off-the-shelf Skywalker x5 Expanded Polyolefin (EPO) foam airframe, into which a carbon fiber spar was added for stiffness. The motors and servos are mounted with 3D printed parts. The tilt-rotor tailsitter MAV has a weight of 1.27 kg and a wingspan of 1.0 m. The center of gravity is positioned at a point 0.35 m downstream from the nose tip along the body longitudinal axis. Each motor has a lateral distance to the center of gravity of 0.3 m, denoted by b in Figure 3.2. Longitudinally, the distance between the axis of each tilt servo to the center of gravity is 0.135 m, denoted by l. Moreover, the maximum deflection angle of the tilt servos is 55°, and an inventory of the main electronic components used for the drone is presented in Table 3.1.

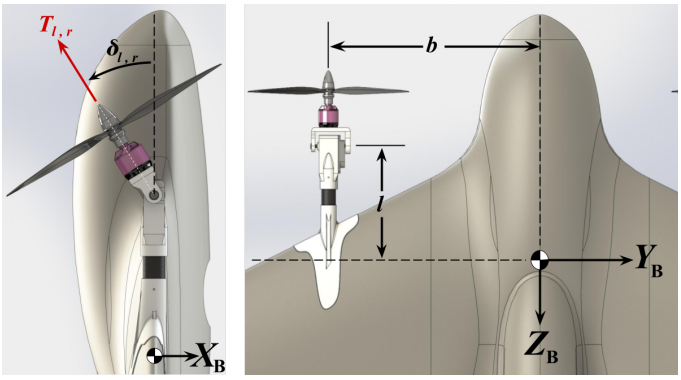

Figure 3.2: Definition of the positive deflection angles of the left & right motors δ_l & δ_r respectively as well as the scalar distances of each motor from the CG.

3.3. Attitude Control

3.3.1. Incremental Nonlinear Dynamic Inversion

INDI control is a sensor-driven approach based on the principle that both internal and external forces and moments acting on a rigid body (such as due to wind disturbances) will cause linear and angular accelerations which can be derived from accelerometer and gyroscope measurements. We denote the angular velocity vector of the vehicle by $\boldsymbol{\Omega}$, the velocity vector in the body frame by $\mathbf{v}$, the tilt angle of servos by $\boldsymbol{\delta}$ and the angular velocity of the left and right rotors by $\boldsymbol{\omega} = [\omega_l \ \omega_r]^T$. In this chapter, it is assumed that the inertia change due to the tilt rotors is small and can be neglected. Moreover, the inertia variation caused by tilting rotors occurs at a significantly lower rate than the attitude dynamics and can therefore be regarded as a slowly varying parameter, which which further justifies neglecting it in the INDI framework. Taking a diagonal inertia matrix $\mathbf{I}$, Euler's equation for rotational motion is given by:

$$\mathbf{I}\dot{\boldsymbol{\Omega}} + \boldsymbol{\Omega} \times \mathbf{I}\boldsymbol{\Omega} = \mathbf{M}_c(\boldsymbol{\omega}, \boldsymbol{\delta}) + \mathbf{M}_a(\boldsymbol{\Omega}, \mathbf{v}), \tag{3.1}$$

where the total moment is written as the sum of the moment due to aerodynamic effects $\mathbf{M}_a$ and the moment due to control inputs $\mathbf{M}_c$.The control moment $\mathbf{M}_c$ depends on the angular velocities of the motors and the tilt angles of the left and right servos, and is expressed by the following equation:

$$\mathbf{M}_c = \begin{bmatrix} M_{c_x} \\ M_{c_y} \\ M_{c_z} \end{bmatrix} = \begin{bmatrix} -T_r b \cos\delta_r + T_l b \cos\delta_l \\ T_r l \sin\delta_r + T_l l \sin\delta_l \\ T_r b \sin\delta_r - T_l b \sin\delta_l \end{bmatrix}, \tag{3.2}$$

where M_{c_x}, M_{c_y} and M_{c_z} refer to the control moments around X_B, Y_B & Z_B axes respectively. As is defined in Figure 3.2, T_l and T_r are functions of the angular velocity ω of each motors and δ_l and δ_r are tilt angles of the left and right servos.

Equation 3.1 can be inverted to obtain an expression for the angular acceleration $\dot{\boldsymbol{\Omega}}$ as follows:

$$\dot{\boldsymbol{\Omega}} = \mathbf{I}^{-1}\left(\mathbf{M}_a(\boldsymbol{\Omega}, \mathbf{v}) - \boldsymbol{\Omega} \times \mathbf{I}\boldsymbol{\Omega}\right) + \mathbf{I}^{-1}\mathbf{M}_c(\boldsymbol{\omega}, \boldsymbol{\delta}). \tag{3.3}$$

We assume that the drone will rotate relatively slowly, such that the term $\boldsymbol{\Omega} \times \mathbf{I}\boldsymbol{\Omega}$ can be neglected compared to the other terms. We can then apply a first-order Taylor expansion:

$$\begin{aligned}\dot{\boldsymbol{\Omega}} = \dot{\boldsymbol{\Omega}}_0 &+ \frac{\partial}{\partial \boldsymbol{\Omega}}\left(\mathbf{I}^{-1}\mathbf{M}_a(\boldsymbol{\Omega}, \mathbf{v}_0)\right)\Big|_{\boldsymbol{\Omega}=\boldsymbol{\Omega}_0}(\boldsymbol{\Omega} - \boldsymbol{\Omega}_0) \\ &+ \frac{\partial}{\partial \mathbf{v}}\left(\mathbf{I}^{-1}\mathbf{M}_a(\boldsymbol{\Omega}_0, \mathbf{v})\right)\Big|_{\mathbf{v}=\mathbf{v}_0}(\mathbf{v} - \mathbf{v}_0) \\ &+ \frac{\partial}{\partial \boldsymbol{\omega}}\left(\mathbf{I}^{-1}\mathbf{M}_c(\boldsymbol{\omega}, \boldsymbol{\delta}_0)\right)\Big|_{\boldsymbol{\omega}=\boldsymbol{\omega}_0}(\boldsymbol{\omega} - \boldsymbol{\omega}_0) \\ &+ \frac{\partial}{\partial \boldsymbol{\delta}}\left(\mathbf{I}^{-1}\mathbf{M}_c(\boldsymbol{\omega}_0, \boldsymbol{\delta})\right)\Big|_{\boldsymbol{\delta}=\boldsymbol{\delta}_0}(\boldsymbol{\delta} - \boldsymbol{\delta}_0).\end{aligned} \tag{3.4}$$

As was proven in [10], the terms not related to the actuators can be neglected if very fast actuator dynamics are assumed. Therefore, it is assumed that the partial derivatives with respect to $\boldsymbol{\Omega}$ and $\mathbf{v}$ have significantly less influence than those with respect to $\boldsymbol{\omega}$ and $\boldsymbol{\delta}$. Therefore, the omission of the partial derivatives of $\mathbf{M}_a$ with respect to both angular velocity $\boldsymbol{\Omega}$ and linear velocity $\mathbf{v}$ is considered justified. Additionally, we examine the specific force along the negative Z_B-axis, denoted as T_Z:

$$T_Z = \frac{1}{m}\left(T_l \cos\delta_l + T_r \cos\delta_r\right), \tag{3.5}$$

where m is the mass of the MAV.

A desired thrust in the Z_B-axis should be fulfilled with the two motors which also have control authority over the other control DOFs, meaning that the desired thrust increment must be allocated keeping into consideration the other control DOFs. Also applying a Taylor expansion to this equation and combining it with Equation 3.4 yields:

$$\begin{bmatrix} \dot{\boldsymbol{\Omega}} \\ T_Z \end{bmatrix} = \begin{bmatrix} \dot{\boldsymbol{\Omega}}_0 \\ T_{Z_0} \end{bmatrix} + \mathbf{G}(\mathbf{u} - \mathbf{u}_0), \tag{3.6}$$

where the control input vector $\mathbf{u}$ is defined as follows:

$$\mathbf{u} = \begin{bmatrix} \delta_l & \delta_r & \omega_r & \omega_l \end{bmatrix}^\top, \tag{3.7}$$

and with the control effectiveness matrix $\mathbf{G}$ defined analytically as:

$$\mathbf{G} = \begin{bmatrix} \mathbf{I}^{-1}_{\{3\times3\}} & 0 \\ 0 & \frac{1}{m} \end{bmatrix} \begin{bmatrix} -bT_l \mathrm{s}\delta_l & bT_r \mathrm{s}\delta_r & -b\frac{\partial}{\partial\omega_r}(T_r)\,\mathrm{c}\delta_r & b\frac{\partial}{\partial\omega_l}(T_l)\,\mathrm{c}\delta_l \\ lT_l \mathrm{c}\delta_l & lT_r \mathrm{c}\delta_r & l\frac{\partial}{\partial\omega_r}(T_r)\,\mathrm{s}\delta_r & l\frac{\partial}{\partial\omega_l}(T_l)\,\mathrm{s}\delta_l \\ -bT_l \mathrm{c}\delta_r & bT_r \mathrm{c}\delta_r & b\frac{\partial}{\partial\omega_r}(T_r)\,\mathrm{s}\delta_r & -b\frac{\partial}{\partial\omega_l}(T_l)\,\mathrm{s}\delta_l \\ T_l s\delta_l & T_r s\delta_r & \frac{\partial}{\partial\omega_r}(T_r)\,c\delta_r & \frac{\partial}{\partial\omega_l}(T_l)\,c\delta_l \end{bmatrix}, \tag{3.8}$$

where 's' and 'c' represent sine and cosine operations.

Equation 3.6 can be inverted to obtain the INDI control law given by:

$$\mathbf{u}_c = \mathbf{u}_f + \mathbf{G}^+ \left(\boldsymbol{\nu} - \begin{bmatrix} \dot{\boldsymbol{\Omega}}_f \\ T_{Z_f} \end{bmatrix} \right), \tag{3.9}$$

where $\mathbf{u}_c$ is the new commanded input, $\boldsymbol{\nu}$ is the virtual control and the superscript '$+$' represents the Moore-Penrose pseudo-inverse. To remove noise from measured signals, all signals with subscript 0 are filtered with the same filter in order to keep these signals synchronized [11], indicated with the subscript f. Since the angular acceleration $\dot{\boldsymbol{\Omega}}_f$ in Equation 3.9 is from measurements, the impact of wind disturbances can be compensated through the control increments. The structure of the control law is illustrated in the block diagram shown in Figure 3.3.

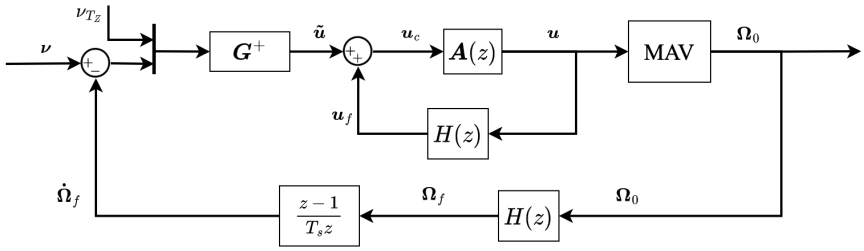

Figure 3.3: Block diagram of the derived control law and its relation to the MAV

The angular rates can be regulated using a proportional feedback controller, as defined in Equation 3.10:

$$\boldsymbol{\nu} = K_{\boldsymbol{\Omega}} \left(\boldsymbol{\Omega}\mathrm{ref} - \boldsymbol{\Omega} \right). \tag{3.10}$$

Attitude control is achieved through an additional proportional controller, which utilizes the vector part of the quaternion error as feedback [12]:

$$\boldsymbol{\Omega}\mathrm{ref} = K_{\boldsymbol{\eta}} \begin{bmatrix} q_{\mathrm{err1}} & q_{\mathrm{err2}} & q_{\mathrm{err3}} \end{bmatrix}, \tag{3.11}$$

where the quaternion error $\mathbf{q}\mathrm{err}$ quantifies the difference between the reference quaternion $\mathbf{q}\mathrm{ref}$ and the current state quaternion $\mathbf{q}s$, and is computed as:

$$\mathbf{q}\mathrm{err} = \mathbf{q}\mathrm{ref} \otimes \mathbf{q}_s^*, \tag{3.12}$$

in which '$\otimes$' denotes the quaternion (Hamilton) product and the superscript '$*$' represents the quaternion conjugate.

3.3.2. Actuator Dynamics

The effectiveness of the INDI control law depends strongly on the relationship between control inputs and measured outputs, making accurate knowledge of the actuator states essential. As actuator state feedback is not available in this case, we employ a model of the actuator to estimate the its state. A servo dynamics experiment was conducted to identify the dynamics of the tilt mechanism, using a gyroscope mounted to the servo arm as shown in Figure 3.4.

The tilt dynamics of the servos are described by a second-order transfer function as follows:

$$A(s) = e^{-\tau_d \cdot s} \cdot \frac{\omega_n^2}{s^2 + 2\zeta\omega_n s + \omega_n^2}. \tag{3.13}$$

Here, τ_d represents the actuator delay, ω_n denotes the natural frequency, and ζ is the damping ratio. The resulting response is subsequently processed through a rate limiter, set according to the maximum angular rate observed during the experiments. The identified tilt dynamics are summarized in Table 3.2. The corresponding discrete-time transfer function, derived for a sampling frequency of 500 Hz, is expressed as follows:

$$A(z) = z^{-7} \cdot \frac{0.01175z^{-1} + 0.01079z^{-2}}{1 - 1.752z^{-1} + 0.7741z^{-2}} \tag{3.14}$$

Figure 3.4: Photograph of the experimental hardware for the servo dynamics experiment

Table 3.2: Summary of actuator dynamics characteristics

Characteristics	Value	Unit
Tilt servo delay, τ_d	14	[ms]
Tilt servo natural frequency, ω_n	76	[rad/s]
Tilt servo damping ratio, ζ	0.8	[-]
Tilt servo rate limit	11.34	[rad/s]

The linear mapping relationship between the servo Pulse Width Modulation (PWM) command c_δ and the angle in degrees is obtained and given by:

$$\delta_{l,r} = 0.1096 \cdot c_\delta \tag{3.15}$$

Moreover, to express the thrust as a function of the angular rate $\omega_{l,r}$, static thrust tests using the RCBenchmark 1580 motor test bench were conducted[1]. The following thrust expression at zero inflow speed in Newton is obtained for the motor-ESC pair outlined in Section 3.2.2.

$$T_{l,r}(\omega_{l,r}) = 5.0 \cdot 10^{-6}\omega_{l,r}^2 - 8.0 \cdot 10^{-4}\omega_{l,r} + 0.10, \tag{3.16}$$

where angular rate $\omega_{l,r}$ as a function of motor PWM command u_m is given by:

$$\omega(u_m) = -6.0 \cdot 10^{-4}u_m^2 + 3.1u_m - 2.6 \cdot 10^3. \tag{3.17}$$

3.3.3. Implementation

The attitude control law derived in Section 3.3.1 was applied alongside the actuator dynamics modeled in Section 3.3.2 within the Paparazzi open-source autopilot soft-

[1]https://www.tytorobotics.com/pages/series-1580-1585

ware[13]. The following three sections hightlight aspects taken into consideration for the successful implementation of the INDI control law on the presented tilt-rotor tailsitter.

(1) Filtering

Since angular accelerations are derived by differentiating the angular rate signals measured by the onboard gyroscope, the resulting data is inherently noisy due to both structural vibrations and sensor noise. To suppress this noise, the gyroscope signals are processed using a second-order Butterworth filter. The filter's transfer function in the Laplace domain is given by:

$$\mathbf{H}(s) = \frac{\omega_c}{s^2 + 2\zeta\omega_c s + \omega_c^2}, \tag{3.18}$$

where the corner frequency ω_c is 6.28 rad/s (1 Hz), and the damping ratio ζ is 0.707. The corresponding discrete-time transfer function $\mathbf{H}(z)$ is obtained using the Tustin transformation with a sampling frequency of 500 Hz.

Additionally, since the tilting mechanism rotates about an axis aligned with the Y_B-axis, increased noise is observed in the pitch rate measurements. This noise propagates through the control system, particularly affecting the computation of the angular acceleration setpoint. To mitigate this effect, a first-order low-pass filter with a cutoff frequency ω_c of 12.56 rad/s (2 Hz) is applied to the Y_B-axis rate feedback. The proportional feedback control law in Equation 3.10 is thus modified as follows:

$$\boldsymbol{\nu} = K_{\boldsymbol{\Omega}} \left(\boldsymbol{\Omega}_{\text{ref}} - \begin{bmatrix} p \\ q_{f_{\text{LP}}} \\ r \end{bmatrix} \right) \tag{3.19}$$

where the subscript 'f_{LP}' indicates the low-pass filtered signal.

(2) Control Allocation Priorities

To avoid exceeding the actuator limits with Equation 3.9, the Weighted Least Squares (WLS) control allocation algorithm was employed in order to give priorities to the control objectives [14]. In this implementation, the Weighted Least Squares (WLS) control allocation algorithm is configured with relative priority weights of $[1, 1, 1, 10]$, corresponding to rotations about the X_B-, Y_B-, and Z_B-axes, and thrust along the negative Z_B-axis, respectively.

Furthermore, when a motor's throttle is reduced to 0%, its corresponding tilt actuator loses control authority, rendering the matrix $\mathbf{G}$ singular. This condition prevents the control allocation algorithm from computing a valid solution. To prevent this, a minimum throttle level is required for each motor, respectively 41.6% for vertical flight and 21% for horizontal flight. Note that the nominal throttle setting for hovering is approximately 70%, leaving sufficient range for differential thrust.

(3) Constraining Control Objective

The INDI control law and WLS control allocation rely on the linearization of the control forces in Equation 3.4, which can lead to linearization errors if the commanded control input is far away from the linearization point. We propose to constrain the control increment to the vicinity of the linearization point in this chapter. On the one hand, the maximum setpoint for roll, pitch and yaw rates is set as ± 2 rad/s (approx. 115 deg/s). On the other hand, a maximum tilt increment of 25° is imposed, based on a comparison between angular accelerations predicted using the linearized control effectiveness model in Equation 3.8 and those calculated from the nonlinear control moment formulation in Equation 4.15. This limit was chosen as a 25° increment produced a deviation of only 3.3%, indicating acceptable linearization accuracy.

3.4. Flight Test Results

To evaluate the performance of thrust vectoring as the only means of control moment generation, both indoor and outdoor tests have been conducted. The results of the performed flight tests are demonstrated in the following section.

3.4.1. Indoor Flight Test

Multiple indoor fight tests were conducted in a $10\text{m}\times10\text{m}$ flight arena, in order to verify the implemented INDI attitude control law and the modeled actuator dynamics. Due to the limited space, only hovering tests were performed indoors.

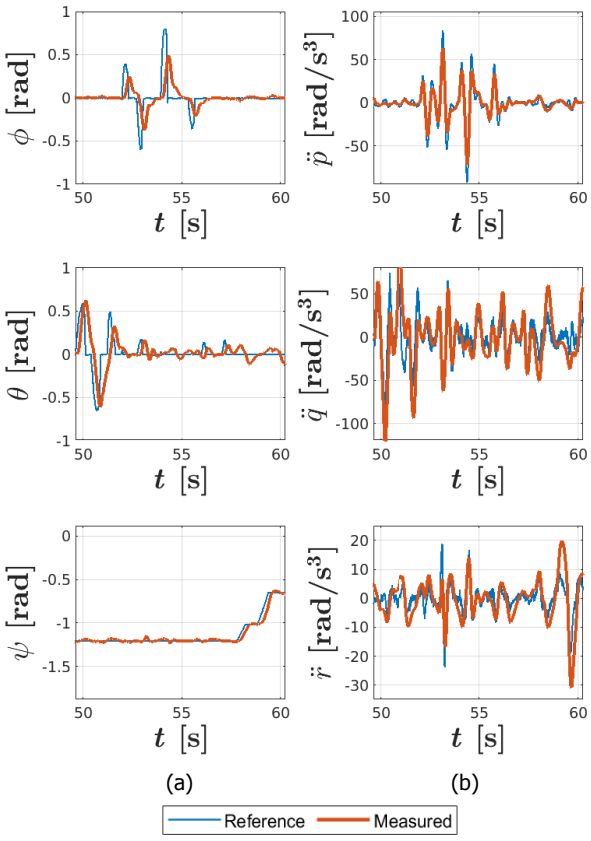

Figure 3.5: (a) Pilot-commanded attitude reference versus measured Euler angles for the indoor vertical flight test; (b) Corresponding commanded angular jerk reference versus measured angular jerks for the indoor vertical flight test.

Figure 3.5 presents a comparison between pilot commanded attitude references and the corresponding measurements during the fight tests, shown for both Euler angles and angular jerk responses. Though the control effectiveness matrix G theoretically maps inputs to angular accelerations, the jerk response captures the rate of acceleration and is critical for validating the transient fidelity of the model. Specifically, the references and measurements are respectively calculated and measured for roll, pitch and yaw angles and angular jerk responses to the same actuator input from one indoor vertical flight test. The figure shows that the measured Euler angles are able to keep a generally good track of the reference attitude angles. It can also be seen from the figure that the measured angular jerk responses mostly align

with the angular jerks calculated from the control derivatives, verifying that the actuator dynamics and actuator control effectiveness have been accurately modeled. Nevertheless, some discrepancies in magnitude are also observed which can be explained by the difference between the actual thrust and the computed thrust according to the static test results. Though not considering wind disturbances, the indoor flight test results validate the successful implementation of the INDI attitude control law for the tilt-prop tailsitter during vertical flight.

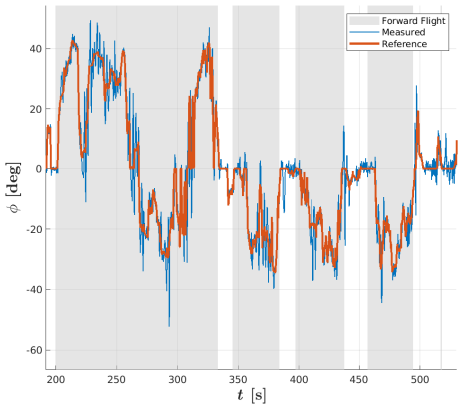

(a) Roll ϕ measured and reference angles for the flight (ZXY Euler)

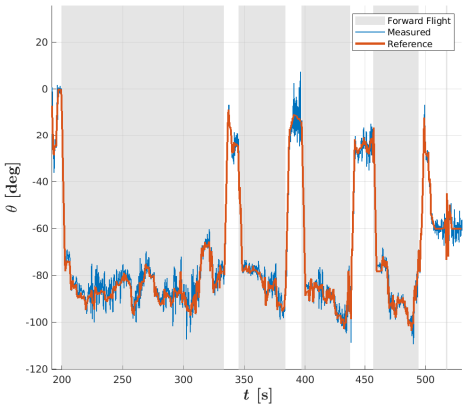

(b) Pitch θ measured and reference angles for the flight (ZXY Euler)

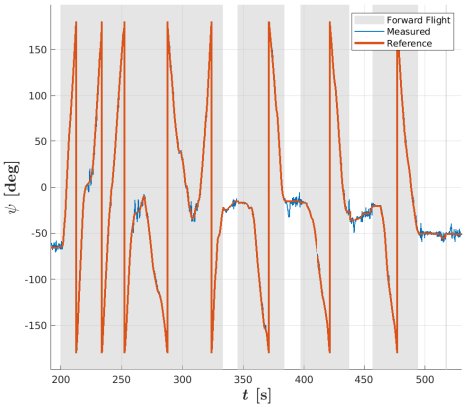

(c) Yaw ψ measured and reference angles for the flight (ZXY Euler)

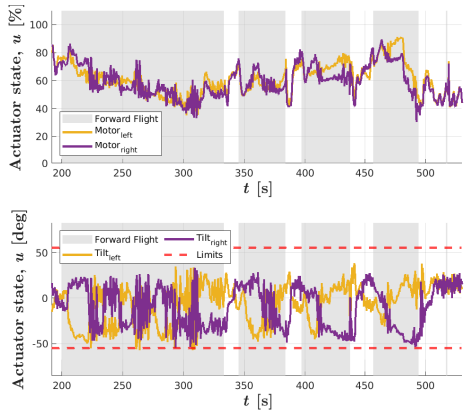

(d) Evolution of actuator states $\mathbf{u}$, respectively, motor evolution as a percentage of max throttle setting and tilt angle $\delta_{l,r}$ in degrees.

Figure 3.6: Tracking performance of attitude controller for a six-minute flight within the whole envelope, grey shaded areas of all plots represent the horizontal flight phase.

3.4.2. Outdoor flight test

To test the flight performance of the tilt-rotor tailsitter in the whole flight envelope, multiple outdoor flights were conducted. The flight test results presented below were from an approximately six-minute continuous outdoor flight, including hovering and forward flight and transitions between the two.

Figure 3.6 depicts the tracking performance of the INDI attitude controller for the tilt-rotor tailsitter within the whole envelope, in which gray shaded areas correspond to the forward flight phase. It can be observed that during the six-minute fight, eight transitions between hovering and forward flights were performed.

In Figure 3.6(a), Figure 3.6(b) and Figure 3.6(c), the tracking performance for ϕ, θ and ψ are displayed respectively. It can be seen that the measured attitude angles follow the reference angles accordingly, showing that it is possible to control the vehicle with the approach presented. Nevertheless, in multiple outdoor flight tests, the drawback of the proposed tilt-rotor tailsitter design is also exposed. Figure 3.7 presents the roll angle tracking performance and the corresponding actuator states for a 130-second flight that covers the whole flight envelope. During forward flight, notable tracking errors for the roll angle are observed, where the left and right servos have already generated large tilt deflections, showing the deficiency of the tilt-rotor tailsitter with only leading-edge mounted motors for control moment generation.

3.5. Discussion

To give an insight into actuator saturation, the actuator states are displayed in Figure 3.6(d), in which the motor states are shown as a percentage of their maximum throttle setting and servo states directly as tilt angles in degrees. Even if the tilt angle command exceeds the lower limit at very rare moments (around 265s and 310s) due to overshoot, throughout the entire flight, the incremental control inputs for tilt angles are within the range of -55° to 55°. It is noteworthy that during the entire outdoor test, actuator saturation happens to the left tilt servo δ_l three times, with a total time of 0.544s taking up approximately 0.15% of the whole six-minute test.

Figure 3.8(a) presents the actuator states at various pitch angles where the vehicle is in pitch equilibrium: the pitch angular acceleration $\dot{q}$ is very low, specifically, $-0.5 \leq \dot{q} \leq 0.5$ [deg/s^2] and $-5 \leq q \leq 5$ [deg/s]. The red diamond in the figure refers to an instance of left tilt saturation of -55 deg. However, the corresponding left motor throttle is only 43% and the percentage of pitch moment

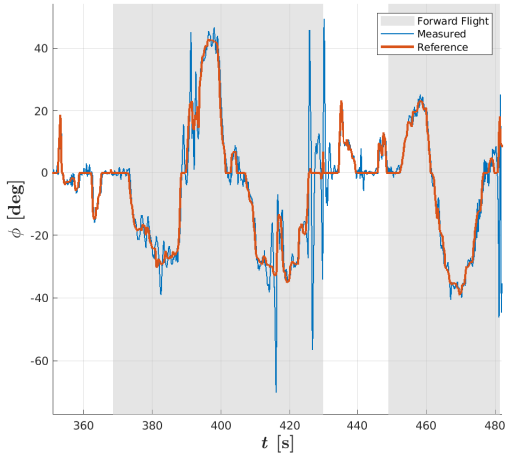

(a) Roll ϕ measured and reference angles for the flight (ZXY Euler)

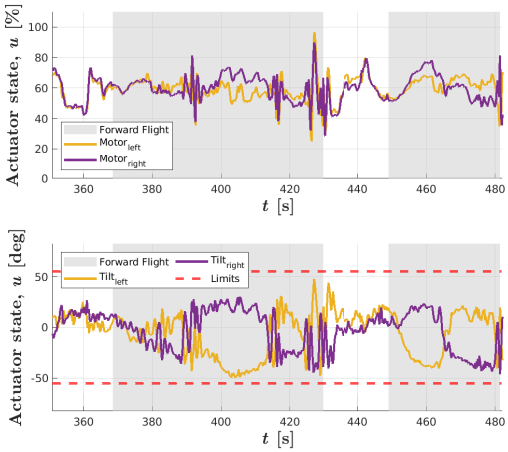

(b) Evolution of actuator states $\mathbf{u}$, respectively, motor evolution as a percentage of max throttle setting and tilt angle $\delta_{l,r}$ in degrees.

Figure 3.7: Tracking performance of controller for a 130-second flight, and grey shaded areas correspond to the forward flight phase

to the maximum pitch moment generation availability is -10.25% as is shown in Figure 3.8(b). Despite the instance of the left tilt, there is still sufficient availability for pitch moment generation. It can be concluded that actuator saturation is significantly avoided by the application of thrust vectoring, which provides sufficient pitch moment generation capability even with the occasional occurrence of actuator saturation.

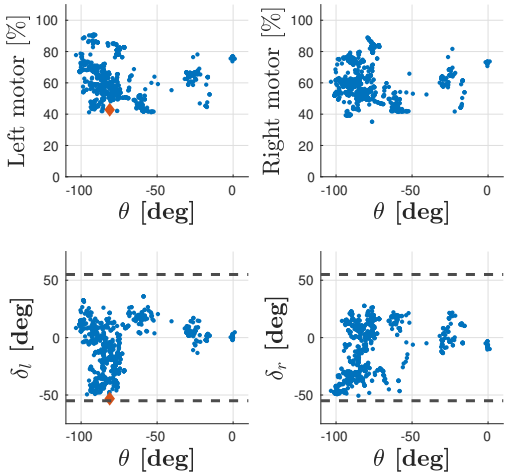

(a) Tilt deflections $\delta_{l,r}$ at varying pitch θ angle equilibrium points

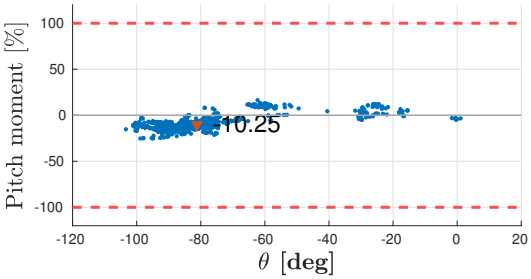

(b) Pitch control moment as percentage of total available pitch moment generation capability.

Figure 3.8: Illustration of pitch moment generation availability despite the occurrence of saturation of left tilt.

Though saturation does not happen often, it can be seen that the tilts show large deflections during forward flight. This raises questions about the effectiveness of

the tilts during forward flight, even though the throttle in some of these cases is not low. A possible cause could be the propeller-wing interaction since the propeller is positioned in front of the wing. It should be considered that even though the tailsitter is meant to fly efficiently during forward flight, flight efficiency may be reduced due to these large deflections.

3.6. Conclusion

This chapter presents a novel configuration of tilt-rotor tailsitter which exclusively uses thrust vectoring for control moment generation. Different from traditional tailsitters, it features two motors mounted on tilting mechanisms. An Incremental Nonlinear Dynamic Inversion (INDI) control law is derived and implemented for the attitude control of the proposed vehicle. Outdoor test flights demonstrate attitude angle tracking for the whole flight envelope. Furthermore, it is found that the use of thrust vectoring for control moment generation avoids actuator saturation which only takes up 0.15% of the flight time. However, from the large differential deflections of the motor tilts during forward flight it can be concluded that the roll control is not very effective in this flight phase.

Given the fact that the roll control of the tilt-rotor tailsitter is shown to be poor during forward flight, quantitative and qualitative comparisons for respectively pitch, roll and yaw moment generation between thrust vectoring and flap deflection will be addressed in future work. Overall, this chapter highlights both the practical viability of using thrust vectoring alone for control in tailsitters and the successful adaptation of the INDI control law to this configuration.

References

[1] A. S. Saeed, A. B. Younes, C. Cai, and G. Cai, "A survey of hybrid Unmanned Aerial Vehicles", *Progress in Aerospace Sciences*, vol. 98, pp. 91–105, 2018.

[2] E. J. Smeur, M. Bronz, and G. C. de Croon, "Incremental control and guidance of hybrid aircraft applied to a tailsitter unmanned air vehicle", *Journal of Guidance, Control, and Dynamics*, vol. 43, no. 2, pp. 274–287, 2020.

[3] Y. Yang, X. Wang, J. Zhu, X. Yuan, and X. Zhang, "Robust proportional incremental nonlinear dynamic inversion control of a flying-wing tailsitter", *Proceedings of the Institution of Mechanical Engineers, Part G: Journal of Aerospace Engineering*, vol. 234, no. 16, pp. 2274–2295, 2020.

[4] J. Zhong, B. Song, Y. Li, and J. Xuan, "L1 adaptive control of a dual-rotor tail-sitter unmanned aerial vehicle with input constraints during hover flight", *IEEE Access*, vol. 7, pp. 51 312–51 328, 2019.

[5] Z. Ma, E. J. J. Smeur, and G. C. H. E. de Croon, "Wind tunnel tests of a wing at all angles of attack", *International Journal of Micro Air Vehicles*, vol. 14, 2022.

[6] M. Bronz, "Comparison of pitching moment generation via flap deflection and thrust vectoring on a generic blown-wing model", in *AIAA Aviation 2019 Forum*, 2019, p. 3171.

[7] E. A. Tal and S. Karaman, "Global trajectory-tracking control for a tailsitter flying wing in agile uncoordinated flight", in *AIAA AVIATION 2021 FORUM*, 2021, p. 3214.

[8] L. R. Lustosa, F. Defay, and J. M. Moschetta, "Longitudinal study of a tilt-body vehicle: Modeling, control and stability analysis", *2015 International Conference on Unmanned Aircraft Systems, ICUAS 2015*, pp. 816–824, 2015.

[9] J. L. Forshaw and V. J. Lappas, "High-fidelity modeling and control of a twin helicopter rotor tailsitter", *AIAA Guidance, Navigation, and Control Conference 2011*, no. August, pp. 1–16, 2011.

[10] R. Steffensen, A. Steinert, and E. J. J. Smeur, "Nonlinear dynamic inversion with actuator dynamics: An incremental control perspective", *Journal of Guidance, Control, and Dynamics*, pp. 1–9, Dec. 2022.

[11] E. J. J. Smeur, Q. Chu, and G. C. H. E. de Croon, "Adaptive incremental nonlinear dynamic inversion for attitude control of micro aerial vehicles", *2016 AIAA Guidance, Navigation, and Control Conference*, pp. 1–16, 2016.

[12] E. J. J. Smeur, G. C. H. E. de Croon, and Q. Chu, "Cascaded incremental nonlinear dynamic inversion for MAV disturbance rejection", *Control Engineering Practice*, vol. 73, no. January, pp. 79–90, 2018.

[13] G. Hattenberger, M. Bronz, and M. Gorraz, "Using the Paparazzi UAV System for Scientific Research", in *International Micro Air Vehicle Conference and Competition (IMAV)*, 2014, pp. 247–252.

[14] E. J. Smeur, E. C. Höppener, and D. Wagter, "Prioritized Control Allocation for Quadrotors Subject to Saturation", *International Micro Air Vehicle Conference and Flight Competition 2017*, pp. 37–43, 2017.

4

Design and Control of a Tilt-Rotor Tailsitter Aircraft with Pivoting VTOL Capability

As shown in Chapter 3, tailsitters with only tilting rotors suffer from limited control effectiveness and associated actuator saturation during vertical flight and transitions. This chapter addresses that limitation by introducing a tilt-rotor tailsitter equipped with both elevons and tilting rotors. A cascaded weighted least squares-based incremental nonlinear dynamic inversion (INDI) controller enables autonomous waypoint tracking at 16 m/s, including smooth transitions without actuator saturation. Wind tunnel and flight tests confirm improved roll control over rotor-only designs and superior vertical maneuverability compared to elevon-only setups. The vehicle also demonstrates stable autonomous takeoff and landing using a novel pivoting strategy under wind disturbances.

This chapter is based on the following article:
Z. Ma, E.J.J. Smeur, G.C.H.E. de Croon, *Design and control of a tilt-rotor tailsitter aircraft with pivoting VTOL capability*, IEEE Robotics and Automation Letters (2025) vol. 10, no. 6, pp. 5911-5918.

4.1. Introduction

In the field of robotics, vertical take-off and landing (VTOL) aircraft have gained increasing attention as they combine the high-speed, long-range capabilities of fixed-wing aircraft with the precise hovering and vertical take-off/landing abilities of rotorcraft. This will make them invaluable in various robotic applications such as aerial photogrammetry, environmental monitoring, and search-and-rescue operations. Compared to other categories of VTOL aircraft like quadplanes[1], tilt-rotors[2] (fixed-wing), tilt-wings[3], tailsitters stand out for their unique transitioning between flight modes by pitching the entire body. This simplicity in mechanical design, along with their operational flexibility, positions tailsitters as a promising solution for complex missions requiring rapid transitions and sustained high-speed flight.

Figure 4.1: (Top) TRE-tailsitter executing a pivot takeoff, where it pitches up steadily off the ground by pivoting around its tail by thrust vectoring. (Bottom) Transition from hover to forward flight, captured at 0.1-second intervals.

Despite promising advancements, tailsitters face two significant challenges that hinder their broader application. The first challenge lies in robust vertical take-off and landing. Conventional VTOL tailsitters require an upright stand on the ground before takeoff, necessitating structural elements such as additional landing gears[4],[5],[6],[7]. These structures, while mechanically simple, add extra weight and drag and restrict the operational flexibility of the tailsitter, especially in uneven

terrain or windy conditions. For example, if a tailsitter with landing gears tips over, it will require human intervention before a new take-off is possible. This reliance on precise ground placement and human intervention reduces the autonomy and deployment flexibility of the system.

A tilt-rotor mechanism presents a promising alternative by enabling takeoff from a level resting position, as presented in Ardupilot's Thrust Vectored Belly Sitter project and [8]. However, [8] utilizes thrust vectoring solely to lift the aircraft off the ground, while exhibiting a pitch overshoot of approximately 50 degrees and significant horizontal drift. Additionally, for the landing phase, the drone is manually caught by hand at low altitude, posing safety risks and operational constraints.

The second challenge involves controllability and actuator saturation. Tailsitters with only aerodynamic control surfaces that function like elevons (E-tailsitters) often experience limited control effectiveness at low airspeeds, leading to elevon saturation during transitions[9]. This is because the elevon effectiveness benefits from strong velocity-induced airflow at high airspeeds. The effectiveness diminishes during vertical flight or transitions, where airflow over the elevons becomes reduced or even reversed during descent, further reducing control effectiveness [10]. To address this, tailsitters using only tilt-rotors for control moment generation (TR-tailsitters) have been developed, featuring dual tilt rotors for thrust vectoring control[11], [12]. Though the tilt-rotor design guarantees pitch control authority in vertical and transition phases, it suffers from reduced roll control effectiveness in forward flight due to the wing-propeller interaction. To tackle this, a tailsitter combining control surfaces with tilt rotors (TRE-tailsitter) presents a promising solution by combining the effective pitch control of tilting rotors in hover with the stable roll control provided by elevon deflections during the forward flight.

For a TRE-tailsitter, the priority is ensuring stable control throughout the flight envelope. Regarding the E-tailsitter control, substantial studies have been conducted. Compared to separate control strategies for each flight phase as presented in [13], [14], a global control law without switching between flight modes is advantageous for rapid and smooth transitions. In [15], a global cascaded proportional–integral–derivative (PID) controller is introduced and validated by indoor trajectory tracking tests, albeit with significant tracking errors in the pitch angle. Differential flatness has also been explored for the global control of tailsitters, as presented in[7] and [16], where agile and aerobatic maneuvers are performed in indoor tests. In [17], a differential flatness based model predictive controller (MPC) is also developed by establishing a high-fidelity aerodynamic model to attain aggressive flights

of tail-sitters. Nevertheless, the differential flatness property doesn't apply to the TRE-tailsitter proposed in this paper. In [18], a position control architecture is employed for a simplified tailsitter model in simulation, integrating a nonlinear dynamic inversion (NDI) attitude controller, which is sensitive to model inaccuracies. Alternatively, in [9], a cascaded sensor-based incremental nonlinear dynamic inversion (INDI) controller is implemented for guidance and control of an E-tailsitter. Given the integration of tilting rotors and aerodynamic control surfaces, establishing an accurate model for the proposed TRE-tailsitter demands considerable efforts. Therefore, a control method with reduced model dependency is favored for the proposed TRE-tailsitter.

The **main contributions** of this work are as follows:

- Autonomous guidance and control of a TRE-tailsitter, guaranteeing control authority across the full flight envelope.
- Pivoting takeoff and landing approach as presented in Figure 4.1, enabling stable takeoff and landing in windy conditions, with robustness validated through indoor and outdoor tests.
- Experimental comparison: Wind tunnel and flight tests confirm the TRE-tailsitter's improved roll control over TR-tailsitters during the forward flight, and superior performance over E-tailsitters in descent and transitions.

The chapter is structured as follows: Section 4.2 introduces the TRE-tailsitter design. Section 4.3 details the pivoting VTOL and in-flight attitude controllers, while Section 4.4 outlines velocity control and guidance. Section 4.5 presents outdoor autonomous flight test results across the full flight envelope, and Section 4.6 discusses pivot controller robustness and comparative fight tests. Section 4.7 concludes this chapter.

4.2. Aircraft Design

This section presents the design of the TRE-tailsitter aircraft, with a focus on optimizing both aerodynamic performance and control moment generation capabilities.

4.2.1. Platform Configuration

Figure 4.2 shows a top view of the designed and built TRE-tailsitter, which includes a pair of elevons and dual independent tilt rotors mounted at the leading edge of the vehicle. Specifically, the tilt angles of the left and right rotors are denoted by

δ_{TL} and δ_{TR}, left and right elevon deflections by δ_{EL} and δ_{ER}, with upward rotor tilt/elevon deflection considered positive, and a maximum tilt/deflection angle $\delta_{\max}$ of $63°$. The thrusts produced by the left and right motors, T_L and T_R. The body axis system is depicted in Figure 4.2, following the right-hand rule. To avoid singularities at $\pm 90°$ pitch angle, the ZXY Euler rotation sequence is adopted throughout this chapter.

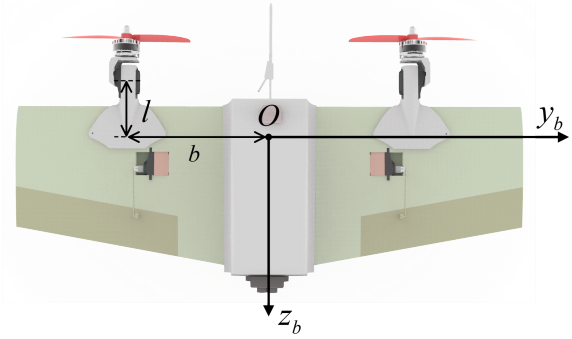

Figure 4.2: The top view of the TRE-tailsitter.

The TRE-tailsitter features a wing with a NACA0012 airfoil, without a fuselage, consisting of three sections with a total wingspan of 0.5 m and a wing area of 0.071 m^2. The center section is 0.06 m wide with a constant chord of 0.16 m, while the left and right sections taper from a root chord of 0.16 m to a tip chord of 0.12 m, each measuring 0.22 m in width. The straight leading edge and tapered trailing edge create a root-to-tip sweep angle of $-2.291°$. The wing's aerodynamic center is located 0.0357 m from the leading edge and the center of gravity (CG) is set 0.03 m from the leading edge to ensure stability, with b and l denoting the distances from CG to the servo tilt axis along y_b and z_b axes. The aircraft weighs 489 g including a 650 mAh Li-Po battery and is equipped with a Pixracer R15 autopilot programmed running the Paparazzi open-source software [19], a pitot tube for airspeed measurement, an M9N-5883 GPS for localization, and a TFMini-S micro LiDAR module for height measurement during landing.

4.2.2. Wind Tunnel Experiment

(1) Tilt rotors

The proposed tiltrotor-tailsitter achieves thrust vectoring by independently tilting

the left and right rotors. The tilt mechanism is achieved with a customized 3D print design presented in Figure 4.3.

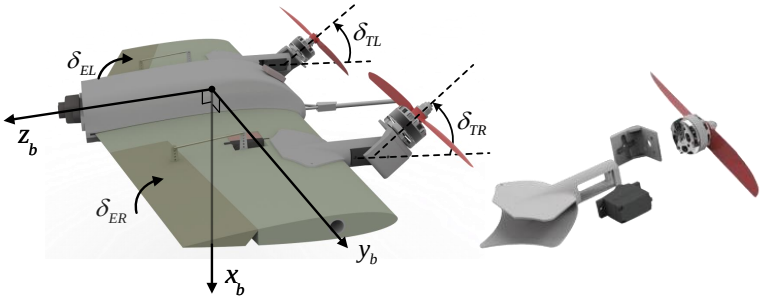

Figure 4.3: Tilt rotor configuration with positive rotor tilt and elevon deflection defined.

(2) Elevons

Our previous research [12] identifies a limitation in roll moment control during forward flight when relying solely on thrust vectoring for control moment generation. When the rotors tilt upwards or downwards, the generated propwash alters the local angle of attack of the wing opposite to the thrust vector direction, potentially reducing the local lift and diminishing the roll moment produced by tilt rotors.

To quantitatively address this, a new wind tunnel experiment has been performed to assess the control moment generation capabilities of rotor tilt and elevon deflection. As shown in Figure 4.4, the experiment took place at TU Delft's Open Jet Facility wind tunnel, which measures 2.85 m in both width and height. The TRE-tailsitter was securely positioned in front of the wind tunnel's open test section, oriented directly into the wind tunnel airflow to create forward flight conditions. The experimental setup measured forces and moments under different motor throttle settings (0%, 30%, 50%, and 70%) for different elevon deflections or rotor tilt angles (0, $\pm 18.9°$, $\pm 37.8°$, and $\pm 63°$) at zero angle of attack and 15 m/s airspeed. Each throttle and elevon deflection/rotor tilt combination was measured for 10 seconds, and the mean values for each measurement were used for subsequent analysis.

Figure 4.5 compares the pitch and roll moments generated by elevon deflection and rotor tilt under various throttle settings. Figure 4.5 (left) shows that rotor tilt is significantly more effective at generating pitch moments than elevon deflection for high throttle settings (50%, 70%), while for relatively lower throttle settings (0%,

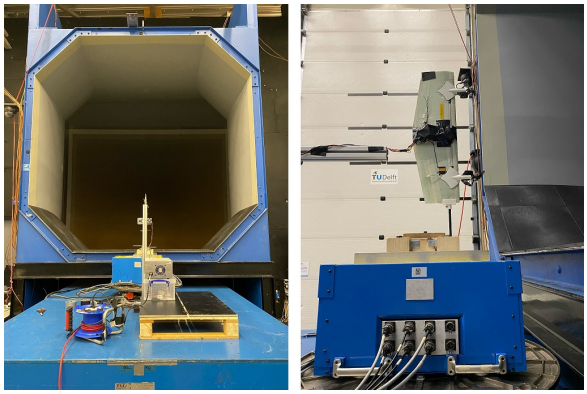

Figure 4.4: The front and side views for the wind tunnel test setup, where the aircraft faces against a wind airflow of 15 m/s, representing the forward flight phase.

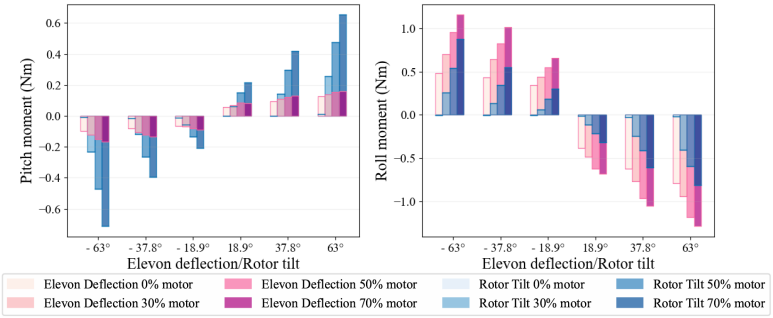

Figure 4.5: Pitch and roll moments generated by either elevon deflection or rotor tilt at 15 m/s airspeed, with only one side rotor tilted or elevon deflected, under the assumption that the left and right actuators have symmetrical effects.

30%), elevons are capable of producing considerable pitch moment compared to tilt rotors. In Figure 4.5 (right) , it displays that elevon deflection is more effective at generating roll moments than rotor tilt for different throttle levels and tilt/deflection angles. Overall, Figure 4.5 highlights the strengths of each actuator, with rotor tilt inducing a stronger influence on pitch control and elevon deflection offering superior roll moment control. The hybrid actuator configuration in the TRE-tailsitter combines the strengths of both types of actuators.

4.3. Attitude Control

In this section, we address the solutions for the attitude control of the customized TRE-tailsitter, including the pivot takeoff/landing and in-flight phases.

4.3.1. Pivot Takeoff and Landing

In this chapter, we propose a new takeoff and landing approach for a tailsitter aircraft through thrust vectoring, which lifts the drone off the ground by pivoting around its tail, eliminating the need of an upright stand before takeoff for conventional tailsitters. To enable controlled takeoff and landing in this pivoting configuration, we have developed a dedicated control strategy, detailed as follows.

Figure 4.6 illustrates a schematic representation of the pivot control system. In this configuration, θ represents the pitch angle, while I'_{yy} denotes the moment of inertia about the tail pivot axis. The distances from the tilt servo axis and the CG to the tail pivot axis are denoted as l_1 and l_2 respectively. Both the left and right rotors are designed to have the same tilt angle and thrust command to prevent roll and yaw movements caused by differential thrust along the z_b and x_b axes. The primary control objective is to regulate the pitch angle θ to track the desired pitch angle θ_d.

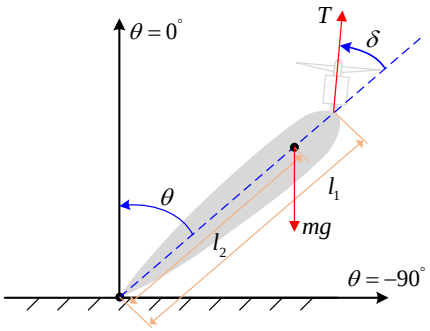

Figure 4.6: Schematic representation of the pivot control system.

The longitudinal dynamics of the pivot system are described by the following equations of motion:

$$\begin{cases} I'_{yy} \cdot \dot{q} = l_1 T \sin\delta - mgl_2 \sin(-\theta), \\ \dot{\theta} = q, \end{cases} \tag{4.1}$$

where m is the mass of the drone, T is the combined thrust of both propellers, δ represents the tilt angle, and $\dot{q}$ is the angular acceleration around y_b axis.

Next, we define the state and control input as:

$$x_1 = \theta - \theta_d, \quad x_2 = q, \quad u = T\sin\delta, \tag{4.2}$$

which leads to the following system model:

$$\begin{cases} \dot{x}_1 = x_2 - \dot{\theta}_d, \\ \dot{x}_2 = \frac{mgl_2 \sin\theta}{I'_{yy}} + \frac{l_1}{I'_{yy}} u. \end{cases} \tag{4.3}$$

For Lyapunov stability analysis, we define an auxiliary state $z = k_1 x_1 + x_2 - \dot{\theta}_d$, whose time derivative is

$$\dot{z} = k_1 x_2 - k_1 \dot{\theta}_d + \frac{mgl_2 \sin\theta}{I'_{yy}} + \frac{l_1}{I'_{yy}} u - \ddot{\theta}_d, \tag{4.4}$$

where k_1 is a positive parameter. To stabilize the auxiliary state z, we design the controller as follows:

$$u = \frac{I'_{yy}}{l_1} \left(-k_1 x_2 + k_1 \dot{\theta}_d - \frac{mgl_2 \sin\theta}{I'_{yy}} + \ddot{\theta}_d - k_2 z \right), \tag{4.5}$$

where $k_2 > 0$ is a control gain. To analyze the closed-loop stability, a Lyapunov function candidate is chosen as $E = \frac{1}{2} z^2$. With (1)-(4), we have

$$\dot{E} = -k_2 z^2 = -2k_2 E. \tag{4.6}$$

This negative semi-definite expression for $\dot{E}$ ensures that the closed-loop system is globally asymptotically stable, which implies that $z \to 0$ as $t \to +\infty$. When $z = 0$, we have $x_2 = \dot{\theta}_d - k_1 x_1 \Rightarrow \dot{x}_1 = -k_1 x_1$. It follows that $x_1(t) = x_1(0) e^{-k_1 t}$, which implies the pitch error $x_1 = \theta - \theta_d$ converges to zero.

Subsequently, the overall control input u needs to be allocated between thrust T and tilt angle δ. In real implementation, the desired pitch angle is set to be either a constant angle or a ramp variable, so $\dot{\theta}_d$ is 0 or a constant, and $\ddot{\theta}_d$ is 0. The auxilary state z into Eq. (4.5) yields:

$$u = \underbrace{\frac{I'_{yy}}{l_1} k_1 k_2 x_1 - \frac{I'_{yy}}{l_1} (k_1 + k_2)(x_2 - \dot{\theta}_d)}_{\Delta u} \underbrace{- \frac{mgl_2 \sin\theta}{l_1}}_{u_{eq}}, \tag{4.7}$$

where the control input is composed of two parts: the equilibrium component u_{eq} and the feedback correction Δu which refers to the real-time adjustments required

to achieve the desired state. Specifically,

$$u_{eq} = -\frac{mgl_2 \sin\theta}{l_1}, \quad T_{eq} = \frac{mgl_2}{l_1}, \quad \delta_{eq} = -\theta. \tag{4.8}$$

In order to allocate Δu to T and δ, we first linearize u in Eq. (4.1) around the equilibrium condition, so that we find the control effectiveness matrix B for thrust and tilt angle as follows:

$$B = \begin{bmatrix} \sin\delta_{eq} & T_{eq}\cos\delta_{eq} \end{bmatrix}. \tag{4.9}$$

The changes in thrust and tilt angle, ΔT_{out}, $\Delta\delta_{out}$, are then calculated with the weighted pseudo inverse:

$$\begin{bmatrix} \Delta T, \Delta\delta \end{bmatrix} = W^{-1}B^T(BW^{-1}B^T)^{-1}\Delta u, \tag{4.10}$$

where the weighting matrix compensates for the different scales of T and δ and is given by:

$$W = \begin{bmatrix} \frac{1}{8.56^2} & 0 \\ 0 & \frac{1}{(63\pi/180)^2} \end{bmatrix}. \tag{4.11}$$

The weight for thrust is empirically determined and the tilt angle weight corresponds to the servo's rotation range. Finally, overall actuator commands of thrust and the tilt angle are given as:

$$T = \Delta_{out} + T_{eq}, \quad \delta = \Delta\delta_{out} + \delta_{eq}. \tag{4.12}$$

By implementing the designed controller and control allocation method, the TRE-tailsitter is capable of VTOL in a pivoting pattern, as is shown in Figure 4.7. With the drone lying on the ground, the rotors initially tilt up to their maximum angle, to initiate an upward thrust. Then the pivot controller governs the drone to pitch up by pivoting around its tail. Once the drone reaches a pitch angle of ±5.4° (6% of 90°) and the pitch angular velocity falls below 5.73°/s (0.1 rad/s), indicating a stable upright state, the drone seamlessly enters the in-flight stage. For landing, the pivot controller is triggered again when the LiDAR sensor detects the altitude falling below 0.15 m and the tailsitter then pivots back to the ground in an inverse manner to takeoff.

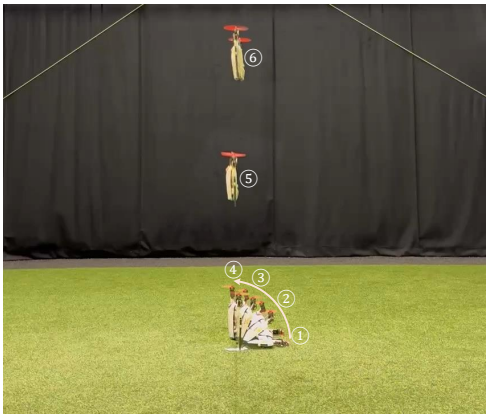

Figure 4.7: Indoor pivoting takeoff maneuver, captured at 0.8-second intervals of sequential video frames.

4.3.2. In-flight INDI Attitude Controller

Due to the high non-linearity inherent in the dynamics of a TRE-tailsitter, an INDI controller is applied during flight, for its minimal dependency on the vehicle model [20]. Since the INDI controller relies on an estimate of the actuator state, the actuator dynamics are modeled as:

$$A(s) = \frac{1}{\tau s + 1}, \tag{4.13}$$

where $\tau_{servo} = 0.00325$ s with a rate limit of 12.54 rad/s; $\tau_{motor} = 0.00707$ s with no rate limit.

Let Ω denote the angular velocity vector of the vehicle, v the velocity vector in the body frame, and $T = [T_l, T_r]^T$ the left and right motor thrusts, respectively. Assuming that changes in inertia due to the rotor tilts are negligible, and considering a diagonal inertia matrix I, Euler's equation for rotational motion can be expressed as follows:

$$I\dot{\Omega} + \Omega \times I\Omega = M_{\delta_T}(T, \delta_T) + M_a(\Omega, v, \delta_E), \tag{4.14}$$

where M_a denotes the aerodynamic moments acting on the vehicle, and M_{δ_T} represents the control moments generated by the rotor tilt which can be further expanded as below:

$$M_{\delta_T} = \begin{bmatrix} bT_L \cos\delta_{T_L} - bT_R \cos\delta_{T_R} \\ lT_L \sin\delta_{T_L} + lT_R \sin\delta_{T_R} \\ -bT_L \sin\delta_{T_L} + bT_R \sin\delta_{T_R} \end{bmatrix}, \tag{4.15}$$

The angular accelerations of the vehicle are obtained by rearranging Euler's equation as:

$$\dot{\Omega} = I^{-1}\left(M_{\delta_T}(T, \delta_T) + M_a(\Omega, v, \delta_E)\right), \tag{4.16}$$

where we assume the drone rotates slowly enough that the term $\Omega \times I\Omega$ is negligible compared to the other terms. To incorporate thrust control along the negative z_b axis, the desired overall trust T_z is expressed as:

$$T_Z = \frac{1}{m}\left(T_L \cos \delta_{T_L} + T_R \cos \delta_{T_R}\right), \tag{4.17}$$

The system dynamics consisting of the drone's angular acceleration and overall thrust can be expressed as:

$$\begin{bmatrix} \dot{\Omega} \\ T_Z \end{bmatrix} = \begin{bmatrix} \dot{\Omega}_0 \\ T_{Z_0} \end{bmatrix} + G(u - u_0), \tag{4.18}$$

where $u = \left[\delta_{T_L}, \delta_{T_R}, T_L, T_R, \delta_{E_L}, \delta_{E_R}\right]^T$ represents a new command, and u_0 represents the current actuator state that can be modeled from the control input vector u_c with the actuator dynamics. Then, the control effectiveness matrix G is expressed as:

$$G = \begin{bmatrix} G_{\delta_T} & G_T & G_E \end{bmatrix}, \tag{4.19}$$

where G_{δ_T}, G_T, and G_E represent the control effectiveness of the rotor tilt, motor rotational speed and elevon deflection, respectively. Specifically,

$$G_{\delta_T} = \begin{bmatrix} \frac{\partial (I^{-1} M_{\delta_T})}{\partial \delta_T} \\ \frac{\partial T_Z}{\partial \delta_T} \end{bmatrix}, G_T = \begin{bmatrix} \frac{\partial (I^{-1} M_T)}{\partial T} \\ \frac{\partial T_Z}{\partial T} \end{bmatrix}, \tag{4.20}$$

while G_E accounts for the aerodynamic surfaces:

$$G_E = \begin{bmatrix} 0 & 0 \\ G_{E_{25}} & G_{E_{26}} \\ G_{E_{35}} & G_{E_{36}} \\ 0 & 0 \end{bmatrix}. \tag{4.21}$$

Given the elevons are aerodynamic control surfaces, their control effectiveness is continuously affected by the airspeed V. To account for this, we schedule G_E based on the airspeed, as measured by a pitot tube. Since the pitot tube readings are in-

accurate at low airspeed, the control effectiveness of elevon deflection is scheduled with the pitch angle at low airspeed. The functions of elevon control effectiveness, in units of (rad/s^2)/rad, are derived from flight test data. Specifically, the elevon control effectiveness about the pitch axis is given as:

$$G_{E_{25}}(\theta, V) = \begin{cases} 13.10(1 - r_\theta) + 21.83 r_\theta, & V < 12\,\text{m/s}, \\ 13.10 + 0.1746 V^2, & V \geq 12\,\text{m/s}, \end{cases} \tag{4.22}$$

with $G_{E_{26}} = G_{E_{25}}$ and where r_θ serves as a pitch ratio relative to the vertical and forward flight phases:

$$r_\theta = \begin{cases} 0, & -\frac{\pi}{6} \leq \theta, \\ \left(\theta + \frac{\pi}{6}\right)/(-\frac{\pi}{6}), & -\frac{\pi}{3} \leq \theta \leq -\frac{\pi}{6}, \\ 1, & \theta \leq -\frac{\pi}{3}, \end{cases} \tag{4.23}$$

Similarly, the yaw control effectiveness is computed by:

$$G_{E_{35}}(\theta, V) = \begin{cases} 15.72(1 - r_\theta) + 26.19 r_\theta, & V < 12\,\text{m/s}, \\ 15.72 + 0.0873 V^2, & V \geq 12\,\text{m/s}, \end{cases} \tag{4.24}$$

with $G_{E_{36}} = -G_{E_{35}}$.

From Eq. 4.18, the control input u is found using weighted least squares (WLS) algorithm presented in [9], with the cost function defined as:

$$C(u) = \|W_u(u - u_p)\|^2 + \gamma \|W_v(Gu - v)\|^2, \tag{4.25}$$

where u_p represents the preferred control inputs and v is the control objective in terms of $\begin{bmatrix} \dot{\Omega} & T_Z \end{bmatrix}^T$, acquired from the errors in attitude angles and angular rates with a linear controller. γ is a scale factor of 10^4, and W_u and W_v are control input and control objective weighting matrices respectively. W_v is defined as $[10, 10, 0.1, 1.0]$, with the weight corresponding to the priority of the rotation about the x_b, y_b, z_b axes and thrust respectively.

Since thrust vectoring is more effective in the vertical flight phase and elevon deflection is more stable and consistent especially for roll control in the forward flight phase, the controller is designed to prioritize rotor tilt in vertical flight and elevon deflection in forward flight. As is displayed in Figure 4.8, the weights for rotor tilt and elevon deflection, bounded between 0.001 and 1, are adjusted dynamically

and continuously based on the pitch angle, ensuring smooth actuator allocation across different flight phases. The computed weights apply to both left and right rotor tilts/elevon deflections. Throughout the flight envelope, the weights for motor thrust remain constant at 0.001.

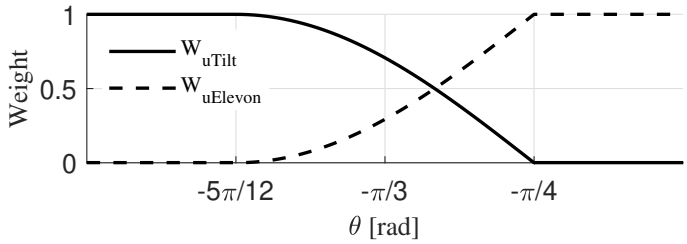

Figure 4.8: Weights for rotor tilt and elevon deflection.

4.4. Velocity Control and Guidance

The guidance of the TRE-tailsitter follows the implementation outlined in [9]. Similar to the INDI attitude controller, an outer loop WLS-based INDI controller is applied making use of a control effectiveness matrix that maps changes in attitude angles and thrust to corresponding changes in linear accelerations. The heading of the tiltrotor-tailsitter is updated by a proportional sideslip correction controller, with the assumption that changes in heading are small relative to the other attitude angles and thrust. Therefore, the control input weight matrix, $W_u = [1, 1, 1]$, assigns equal weights to roll, pitch, and thrust increments, while the control objective weight matrix, $W_v = [100, 100, 1]$, prioritizes the horizontal linear accelerations in the North-East-Down (NED) frame. The reference linear acceleration is computed from position and velocity errors using a PD controller.

In this chapter, the TRE-tailsitter is assigned an autonomous waypoint tracking flight plan. The reference path is defined as straight-line segments connecting the waypoints, and the velocity vector field method is used to guide the drone along the desired track.

4.5. Flight Test Results

The customized TRE-tailsitter's flight performance was evaluated through outdoor tests with the implemented guidance and attitude controllers, and the flight test results are presented in this section.

4.5.1. Pivoting robustness

In order to validate the robustness of the pivoting controller, eight outdoor pivoting tests were conducted sequentially under an average wind of 6.7 m/s and a peak gust of 10.28 m/s, with their pitch angles and pitch rates shown in Figure 4.9. For each test, the pitch angle reaches an allowable error margin of $\pm 5.4^\circ$, corresponding to 6% of the desired movement range (from -90° to 0°) with the pitch rate below $\pm 5.73^\circ$/s, suggesting a stable upright posture ready to enter the in-flight stage. To further demonstrate the benefit of the pivoting approach, a E-tailsitter and a TRE-tailsitter of the same airframe were placed close to a three-bladed fan, which generates strong turbulent flow. As Figure 4.10 shows, the E-tailsitter tips over while the TRE-tailsitter steadily pitches up off the ground and flies against the wind, indicating the superior performance of pivoting takeoff under windy conditions.

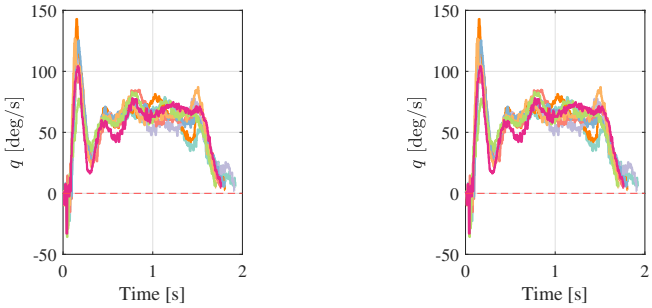

Figure 4.9: Eight sequent outdoor pivoting experiments. (a) Pitch angle. (b) Pitch rate.

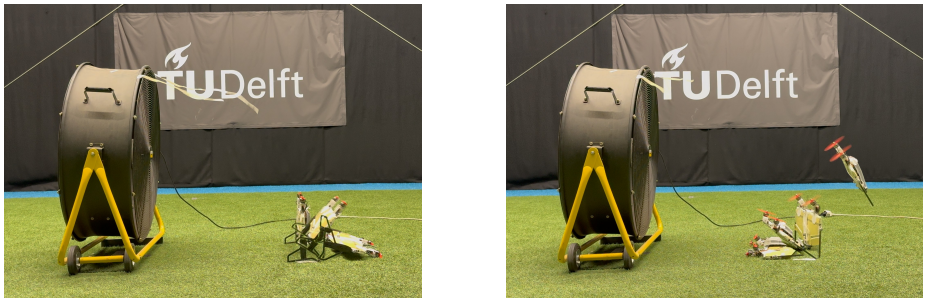

Figure 4.10: Comparative tests between E-tailsitter and TRE-tailsitter under strong turbulent flow.

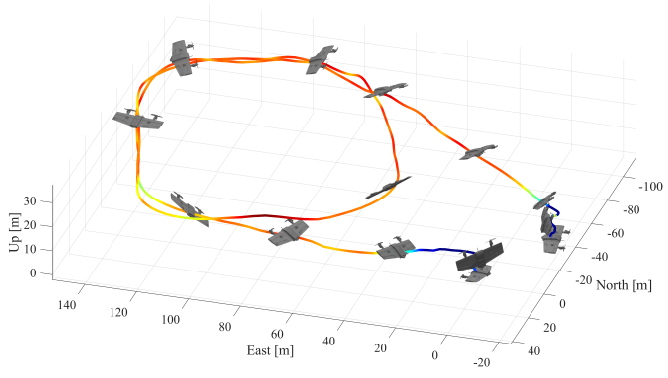

(a)

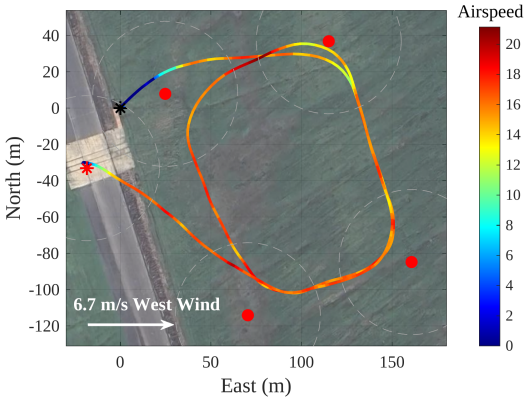

(b)

Figure 4.11: (a) 3D view of an autonomous, outdoor flight covering the full flight envelope. (b) 2D view of the waypoint tracking, with gray dashed lines representing the threshold range for reaching each waypoint. Airspeed in m/s.

4.5.2. Autonomous full-envelope outdoor flight

Figure 4.11(a) illustrates a 3D view of the TRE-tailsitter's trajectory throughout the entire flight envelope, demonstrating its capability to perform vertical takeoff and landing, and smooth transitions between vertical and forward flight phases. The flight begins with a pivoting vertical takeoff, followed by a seamless transition into forward flight. The drone autonomously tracks a series of waypoints before transitioning back to a controlled pivoting landing. Figure 4.11(b) provides a top-down view of the waypoint tracking trajectory with color-coded airspeed. Despite a 6.7 m/s west wind and a peak gust of 10.28 m/s, the drone effectively reaches

each waypoint at a cruise airspeed of 16 m/s, showcasing robust performance under wind disturbances.

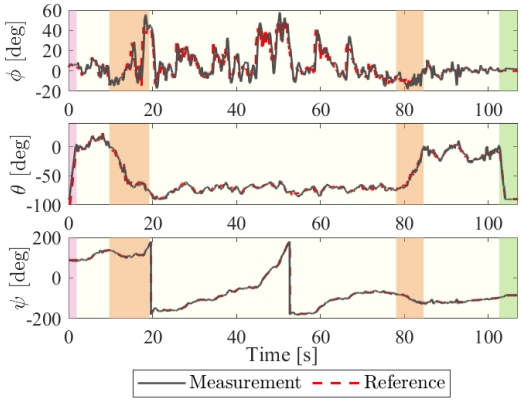

(a)

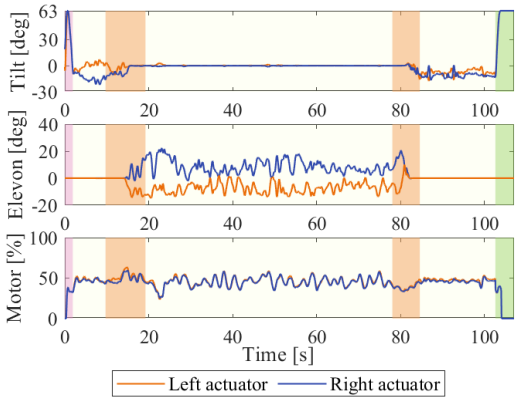

(b)

Figure 4.12: (a) Measured and reference attitude angles corresponding to the autonomous flight shown in the 3D and 2D views. (b) Actuator states during the flight. Pink, light beige and green areas respectively refer to takeoff, in-flight and landing stages, with soft orange highlighting the transition phases.

Figure 4.12(a) presents the measured and reference attitude angles (roll, pitch, and yaw) during the flight depicted in Figure 4.11. During vertical takeoff and landing, the drone exhibits a quick pitch change of approximately $\pm 90^{\circ}$, indicating the pivoting takeoff. Smooth transitions are observed from the effective pitch angle changes. The close alignment between the measured and reference angles across all axes confirms stable control of the TRE-tailsitter across all flight phases. Correspondingly, Figure 4.12(b) displays the actuator states during the flight, including rotor tilt angles, elevon deflections and motor throttle. During takeoff, the

rotors start from a maximum tilt angle and gradually adjust to a neutral position, and vice versa for the landing period. In flight, the rotor tilt is prioritized during vertical flight, while elevon deflection shows more prominent behavior in forward flight. Meanwhile, the motor speed remains relatively consistent throughout. Notably, no actuator saturation occurs during the entire flight, suggesting effective control authority.

4.6. TRE-Tailsitter vs. E-Tailsitter

To further investigate the flight performance of the TRE-tailsitter, comparative flight tests were conducted between the TRE-tailsitter and the E-tailsitter. By setting the weight for rotor tilt to a very high value (100000) and the weight for elevons to 0, the controller uses the elevons only. Additionally, with the actuator command for tilt set as 0, the TRE-tailsitter can be transformed into a E-tailsitter without any hardware modifications.

The first experiment is an 8-meter climb and descent test for both configurations under a 4 m/s north wind, in order to test the influence of vertical descending flight, in which the elevons may encounter reverse flow. Figure 4.13 presents the results. During the descent phase, the E-tailsitter deviates significantly from the expected vertical path and the desired descent speed of 1 m/s, whereas the TRE-tailsitter maintains a stable climb and descent without notable position deviations. Quantitatively, the mean position error for the E-tailsitter is 0.291 m during the climb and increases to 2.708 m during descent, compared to the TRE-tailsitter's lower mean errors of 0.256 m during climb and 0.348 m during descent. Additionally, while no actuator saturation is observed for the TRE-tailsitter, the E-tailsitter encounters downward eleven saturation during descent. This demonstrates the improved flight control performance of the TRE-tailsitter, particularly during descent when the elevon control effectiveness is reduced due to insufficient or reversed airflow over the wings.

In addition to vertical flight, comparative tests were conducted during the transition phase. As shown in Figure 4.14, despite a 6.7 m/s westward wind, the TRE-tailsitter completes a sharp "stop and go" with an apex angle of 12.3° with smooth transitions. In contrast, the E-tailsitter fails due to elevon saturation. Moreover, during the transition from hover to forward flight, the TRE-tailsitter predominantly relies on its tilt rotors, achieving a pitch control effectiveness of 126.6 $(rad/s^2)/rad$ compared to 27.1 $(rad/s^2)/rad$ for the elevon control effectiveness of the E-tailsitter. In the reverse transition, the TR-E tailsitter prioritizes elevons initially and then tilt

rotors, where the pitch control effectiveness values for elevons and tilt rotors are respectively 37.9 (rad/s^2)/rad and 98.6 (rad/s^2)/rad, versus 22.7 (rad/s^2)/rad of that for E-tailsitter's elevons, highlighting the superiority of tilt rotors over elevon deflections during transitions. This comparative study underscores the TRE-tailsitter's capability of executing agile maneuvers, such as sharp turns, under wind disturbances.

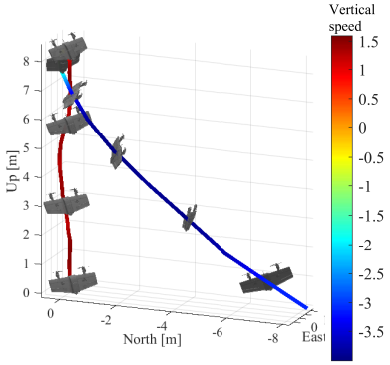

(a) E-tailsitter

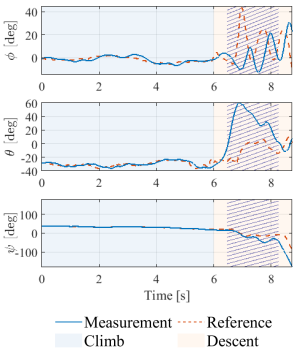

(b) E-tailsitter attitude

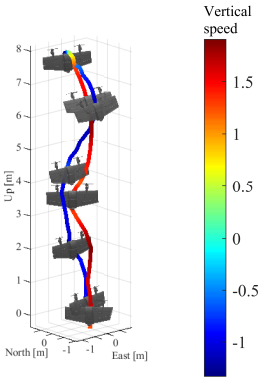

(c) TRE-tailsitter

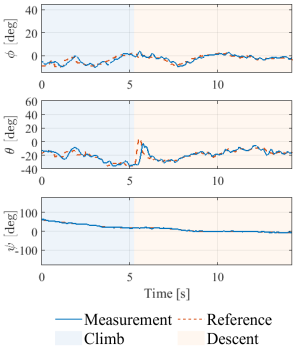

(d) TRE-tailsitter attitude

Figure 4.13: (a) 3D view of the climb and descent process for the E-tailsitter. (b) Attitude tracking for the E-tailsitter during its climb and descent, with shaded regions indicating at least one elevon saturation. (c) 3D view of the climb and descent process for the TRE-tailsitter. (d) Attitude tracking during the TRE-tailsitter's climb and descent. Airspeed in m/s.

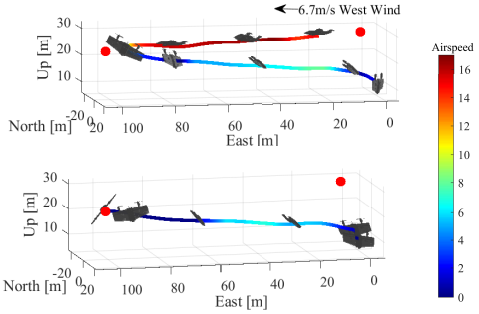

(a) Transition and sharp turn process for the TRE-tailsitter (top) and E-tailsitter (bottom)

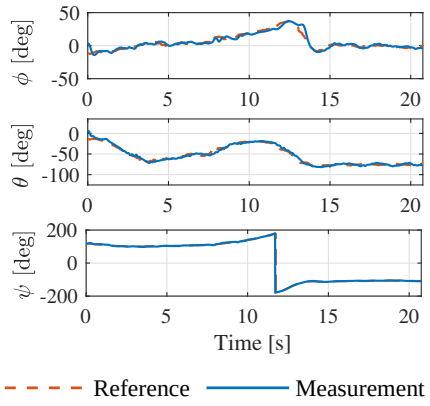

(b) Attitude tracking for the TRE-tailsitter

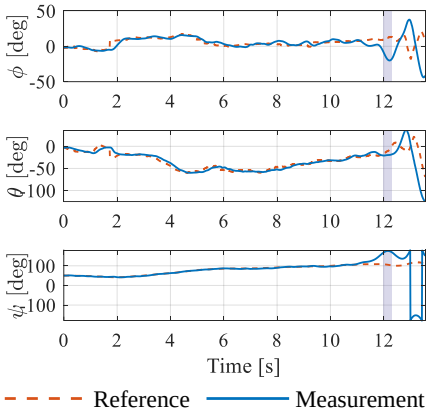

(c) Attitude tracking for the E-tailsitter, with shaded regions indicating at least one elevon saturation

Figure 4.14: (a) Transition and sharp turn process for the TRE-tailsitter and the E-tailsitter. (b) Attitude tracking for the TRE-tailsitter. (c) Attitude tracking for the E-tailsitter, with shaded regions indicating at least one elevon saturation. Airspeed in m/s.

4.7. Conclusion

In this work, a TRE-tailsitter is designed and built to address the challenges of actuator saturation and limited control effectiveness for E-tailsitters during vertical flight and transitions. Additionally, the design overcomes the insufficient roll control authority observed in TR-tailsitters. The incorporation of rotor tilt not only enhances control but also introduces a novel pivoting takeoff and landing capability, eliminating the reliance on auxiliary supporting structures or landing gear commonly required by traditional E-tailsitters. The pivoting controller has demonstrated both stability and robustness under wind disturbances. A cascaded WLS-based INDI controller is implemented to maintain guidance and control of the drone across different flight phases. Wind tunnel tests validate the improved roll control authority of the TRE-tailsitter compared to TR-tailsitters, while comparative outdoor flight tests demonstrate its superior performance over E-tailsitters, particularly during vertical descent and transition phases. Moreover, the TRE-tailsitter exhibits high-speed forward flight capabilities like fixed-wing aircraft and agile maneuverability like quadrotors, particularly during sharp turns, indicating potential applications in drone racing. Future work will focus on exploring advanced trajectory planning algorithms to further optimize the drone's flight performance and agility.

References

[1] H. Karssies and C. De Wagter, "Extended incremental non-linear control allocation (xinca) for quadplanes", *International Journal of Micro Air Vehicles*, vol. 14, p. 17 568 293 211 070 825, 2022.

[2] C. Chen, J. Zhang, D. Zhang, and L. Shen, "Control and flight test of a tilt-rotor unmanned aerial vehicle", *International Journal of Advanced Robotic Systems*, vol. 14, no. 1, p. 1 729 881 416 678 141, 2017.

[3] P. Hartmann, C. Meyer, and D. Moormann, "Unified velocity control and flight state transition of unmanned tilt-wing aircraft", *Journal of guidance, control, and dynamics*, vol. 40, no. 6, pp. 1348–1359, 2017.

[4] J. Zhong and W. Chen, "Transition characteristics for a small tail-sitter unmanned aerial vehicle", *Chinese Journal of Aeronautics*, vol. 34, no. 10, pp. 220–236, 2021.

[5] E. A. Islas-Narvaez, J. F. Ituna-Yudonago, L. E. Ramos-Velasco, M. A. Vega-Navarrete, and O. Garcia-Salazar, "Design and determination of aerodynamic coefficients of a tail-sitter aircraft by means of cfd numerical simulation", *Machines*, vol. 11, no. 17, pp. 1–24, Jan. 2023.

[6] K. Anuar, W. Fatra, A. Asral, N. Nazaruddin, and M. Taslim, "Preliminary design of tail-sitter UAVs", in *3rd Conference on Innovation in Technology and Engineering Science (CITES)*, AIP Publishing, vol. 2891, May 2022, pp. 1–11.

[7] E. A. Tal and S. Karaman, "Global trajectory-tracking control for a tailsitter flying wing in agile uncoordinated flight", in *AIAA Aviation 2021 Forum*, AIAA, Jul. 2021, pp. 1–20.

[8] J. Wang et al., "Vectored-thrust system design for a tail-sitter micro-aerial-vehicle with belly/back takeoff ability", *Aerospace Science and Technology*, vol. 155, p. 109 542, 2024.

[9] E. J. Smeur, M. Bronz, and G. C. de Croon, "Incremental control and guidance of hybrid aircraft applied to a tailsitter unmanned air vehicle", *Journal of Guidance, Control, and Dynamics*, vol. 43, no. 2, pp. 274–287, 2020.

[10] Z. Ma, E. J. J. Smeur, and G. C. H. E. de Croon, "Wind tunnel tests of a wing at all angles of attack", *International Journal of Micro Air Vehicles*, vol. 14, 2022.

[11] S. M. Nogar and C. M. Kroninger, "Development of a hybrid micro air vehicle capable of controlled transition", *IEEE Robotics and Automation Letters*, vol. 3, no. 3, pp. 2269–2276, Jul. 2018.

[12] G. H. Lovell-Prescod, Z. Ma, and E. J. J. Smeur, "Attitude control of a tilt-rotor tailsitter micro air vehicle using incremental control", in *2023 International Conference on Unmanned Aircraft Systems (ICUAS)*, IEEE, Jun. 2023, pp. 842–849.

[13] A. Oosedo, S. Abiko, A. Konno, and M. Uchiyama, "Optimal transition from hovering to level-flight of a quadrotor tail-sitter uav", *Autonomous Robots*, vol. 41, pp. 1143–1159, 2017.

[14] X. Lyu, H. Gu, J. Zhou, Z. Li, S. Shen, and F. Zhang, "A hierarchical control approach for a quadrotor tail-sitter vtol uav and experimental verification", in *2017 IEEE/RSJ International Conference on Intelligent Robots and Systems (IROS)*, IEEE, 2017, pp. 5135–5141.

[15] R. Ritz and R. D'Andrea, "A global controller for flying wing tailsitter vehicles", in *2017 IEEE International Conference on Robotics and Automation (ICRA)*, IEEE, May 2017, pp. 2731–2738.

[16] E. Tal, G. Ryou, and S. Karaman, "Aerobatic trajectory generation for a vtol fixed-wing aircraft using differential flatness", *IEEE Transactions on Robotics*, vol. 39, no. 6, pp. 4805–4819, Dec. 2023.

[17] G. Lu, Y. Cai, N. Chen, F. Kong, Y. Ren, and F. Zhang, "Trajectory generation and tracking control for aggressive tail-sitter flights", *The International Journal of Robotics Research*, vol. 43, no. 3, pp. 241–280, 2024.

[18] K. F. McIntosh, S. Mishra, and J.-P. Reddinger, "Aerodynamic feedforward-feedback architecture for tailsitter control in hybrid flight regimes", *Journal of Guidance, Control, and Dynamics*, pp. 1–12, Jun. 2024.

[19] E. Baskaya, G. Manfredi, M. Bronz, and D. Delahaye, "Flexible open architecture for uass integration into the airspace: Paparazzi autopilot system", in *2016 IEEE/AIAA 35th Digital Avionics Systems Conference (DASC)*, IEEE, 2016, pp. 1–7.

[20] E. J. Smeur, Q. Chu, and G. C. De Croon, "Adaptive incremental nonlinear dynamic inversion for attitude control of micro air vehicles", *Journal of Guidance, Control, and Dynamics*, vol. 39, no. 3, pp. 450–461, 2016.

5

Aerodynamic interaction of a Tilt-Rotor Tailsitter Aircraft

Building on the hybrid actuation and control framework developed in Chapter 4, this chapter shifts focus back to the aerodynamic domain to examine how combined rotor tilt and elevon deflection influence lift and pitching moment in a tilt-rotor tailsitter. Wind tunnel experiments were performed across various airspeeds and angles of attack, with both actuators dynamically adjusted to achieve pitch moment equilibrium. Results show that upward rotor tilt effectively counters the pitch down moment induced by downward elevon deflection, enabling higher lift than achievable with either actuation alone. This coordinated actuation enhances maneuverability in high-speed turns and highlights the importance of modeling aerodynamic coupling between thrust vectoring and control surfaces.

This chapter is based on the following article:
Z. Ma, E.J.J. Smeur, G.C.H.E. de Croon, *Wind Tunnel Tests of a Tilt-Rotor Tailisitter Focused on Wing-Propeller Interaction,* submitted

5.1. Introduction

Hybrid VTOL aircraft integrate the efficient cruise performance of fixed-wing aircraft with the hovering and vertical lift capabilities of rotorcraft, making them well suited for missions such as aerial mapping, environmental monitoring, and search-and-rescue. Among the various hybrid VTOL designs, tailsitters are notable for their mechanically simple transition method, taking off and landing vertically on their tail and rotating their entire body to transition between hover and forward flight. Tailsitters can be classified into three main types based on their actuation control strategies. Traditional tailsitters are equipped with aerodynamic surfaces such as elevons[1],[2],[3],[4] (E-tailsitter), providing effective control at high speed but suffering from reduced pitch control authority and actuator saturation during low-speed flight. The tailsitter employing only thrust vectoring via tilting rotors[5] (TR-tailsitter) ensures reliable pitch control in vertical flight but lacks sufficient roll control during forward flight due to wing-propeller interaction. The TRE-tailsitter[6] combines both configurations by integrating tilting rotors with control surfaces, offering strong low-speed pitch control through thrust vectoring while retaining reliable roll control at high speeds. This integrated actuation scheme improves control effectiveness throughout the flight envelope and mitigates issues related to actuator saturation.

The ability to execute aggressive maneuvers is increasingly sought-after as tailsitters move from basic feasibility toward high-performance applications. Executing agile flight, including rapid accelerations, steep dives, or sharp turns, demands not only sufficient control authority but also effective coordination of the distinct actuator configurations inherent to tailsitters. Accurately predicting and controlling the aerodynamic forces in such conditions is therefore critical. A key factor complicating the guidance and modeling of aggressive turns for a tilt-rotor tailsitter is the strong aerodynamic coupling between the propellers, elevons and the wing. The propeller slipstream modifies the local angle of attack (AoA), and the elevon deflection changes the wing's effective camber; the combined effect of these actuators introduces complex aerodynamic interactions that significantly affect the forces and moments acting on the tilt-rotor tailsitter. Regarding this, some prior studies have investigated the aerodynamic impact of propeller induced flow and the subsequent wing-propeller interaction. As is demonstrated in [7] and [8], propeller-induced flow reshapes the pressure distribution and alters lift and drag, particularly depending on propeller mounting location and flight regime. An integrated panel and blade-element method is developed in [9] to model a tailsitter UAV, revealing that

propeller-induced velocities dominate aerodynamic loads during low-speed flight. The impact of propeller position and AoA on lift and drag is quantified in [10], highlighting that reduced propeller–wing spacing can substantially increase wing lift while decreasing drag, particularly in compound or tilt-rotor configurations. It is illustrated in [11] that the propeller-induced slipstream modifies local angle of attack distributions over the wing, leading to asymmetric lift profiles and changes in pressure gradients. In [12], the presence of slipstream significantly alters the lift distribution, potentially triggering earlier transitions to turbulent flow and enhancing lift on the downstream wing sections. According to [13], such slipstream effects intensify trailing vortices and affect post-propeller wake characteristics. In spite of the contributions made by previous research, the combined aerodynamic effects brought by rotor tilt and elevon deflection in a tilt-rotor tailsitter configuration remain insufficiently characterized, especially during aggressive maneuvers like sharp turns that involve coordinated actuator inputs. A thorough analysis of wing-propeller interaction brought by rotor tilt and elevon deflection is therefore essential for high-speed turning scenarios, where both high lift and pitching moment equilibrium must be achieved.

Motivated by the potential and unresolved challenges of achieving sharp turns with a tilt-rotor tailsitter, this work presents a dedicated experimental investigation of the vehicle's aerodynamics under conditions representative of sharp-turn maneuvers. Although the aerodynamic phenomena involved in aggressive maneuvers are inherently dynamic, the objective of the present wind-tunnel experiments is not to directly reproduce maneuvering flight, but to establish a fundamental understanding of the underlying aerodynamic characteristics in a controlled and interpretable manner. A comprehensive wind tunnel campaign was carried out with the test tilt-rotor tailsitter rigidly mounted on a six-axis force/moment sensor to measure the forces and moments acting on the vehicle across a range of variations in rotor tilt angle, elevon deflection, thrust level, angle of attack and airspeed. To the best of our knowledge, this work provides the first empirical dataset and the derived empirical model capturing the coupled aerodynamic response of a tilt-rotor tailsitter subjected to simultaneous thrust vectoring and control surface deflection, under different angles of attack and airspeeds. Through the pitching moment trim experiments, the study identifies combinations of rotor tilt and elevon deflection that enable the vehicle to simultaneously generate high lift and maintain pitch-moment equilibrium, which serves as a proxy for the vehicle's capability to perform sharp coordinated turns. Furthermore, using the derived empirical aerodynamic model,

the study quantifies the theoretical minimum turning radius of 9.075 m achievable at a given flight speed of 18 m/s for the proposed tilt-rotor tailsitter, providing a promising performance benchmark for agile maneuvering with hybrid aircraft.

The remainder of this chapter is structured as follows. Section 5.2 introduces the experimental setup, including the tilt-rotor tailsitter model, instrumentation, and wind tunnel configuration. Section 5.3 presents the static wind tunnel tests that examine the aerodynamic response under varying rotor tilt and elevon inputs and develops an empirical model using multivariate regression. Section 5.4 details the pitch moment trimming wind tunnel experiments with real-time actuator control to achieve pitch moment equilibrium, and extends the analysis using the empirical model to map lift force contours overlaid with zero pitch moment lines under combined actuation inputs. Section 5.5 explores optimal actuation strategies for theoretical minimum turning radius in high-speed turning scenarios. Finally, Section 5.6 concludes this chapter and discusses the future work for achieving agile sharp turns with tilt-rotor tailsitter UAVs.

5.2. Wind Tunnel Experiment Design

5.2.1. Experiment Proposal

Tilt-rotor tailsitters offer a unique actuator redundancy by combining rotor thrust vectoring with aerodynamic surface control. From fundamental aerodynamic principles, an upward rotor tilt produces additional vertical force, reduced local angle of attack and a pitch-up moment, while a downward deflected elevon increases lift and induces a pitch-down moment. Inspired by this complementary effect, we hypothesize that a coordinated combination of upward tilt and downward elevon deflection can achieve increased lift while maintaining pitch moment equilibrium, which is especially a critical condition for sharp coordinated turns. Fig. 5.1 schematically illustrates the concept.

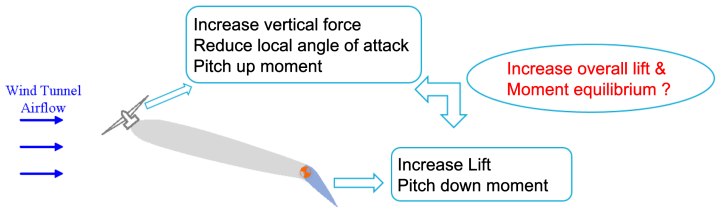

Figure 5.1: Schematic concept of combined tilt and elevon deflection for enhanced lift generation while maintaining pitch moment equilibrium.

However, the presence of wing–propeller interaction, especially the propeller-induced flow over the wing, introduces nonlinear aerodynamic coupling that challenges intuitive predictions. To rigorously investigate the aerodynamic effects of actuator combinations and to evaluate the proposed hypothesis, we design a series of wind tunnel experiments targeting force and moment characterization. The first type is static measurement tests, in which forces and moments are recorded under systematically varied actuator configurations across different angles of attack and wind airspeeds, aimed to develop experimental numerical models. The second type is pitching moment trimming tests, in which the elevon deflection is dynamically adjusted in real time to balance the pitch moment induced by rotor tilt, thereby evaluating the feasibility of achieving moment equilibrium under actuator coordination.

5.2.2. Experiment Setup

Figure 5.2: Wind tunnel experimental setup pictures showing the tilt-rotor tailsitter mounted on a six-axis force/torque sensor in the OJF wind tunnel[14], with a servo-driven mechanism to adjust angle of attack.

To achieve the sharp turn maneuver with a tilt-rotor tailsitter, a series of wind tunnel tests were conducted to investigate the aerodynamic behavior of a custom-built tilt-rotor tailsitter in the TU Delft Open Jet Facility (OJF) low-speed wind tunnel, whose test section outlet measures 2.85 m in both width and height. The test platform is a custom-built tilt-rotor tailsitter, featuring a pair of rotors with variable tilt in the pitch plane and a set of trailing-edge elevons. The airframe has a wingspan of $0.5m$ and uses a symmetric NACA0012 airfoil profile to emulate the tailsitter's wing.

As Fig. 5.2 displays, the tilt-rotor tailsitter, whose specific geometry is described in Chapter 4, is mounted in a horizontal, forward-flight configuration within the wind tunnel test section, with its longitudinal axis aligned with the freestream flow. The support assembly consists of multiple modular components to ensure accu-

rate load measurement and precise control of the angle of attack. Structurally, the drone airframe is attached to a 3D-printed mounting interface, which is connected to a six-axis force/torque sensor (ATI Mini45, IP65-rated) by a support bar. An additional custom-printed connector links the sensor to a Xiaomi CyberGear servo, which enables automated control of the drone's angle of attack by rotating the entire upper assembly as a single rigid body about the pitch axis. All modular components remained mechanically fixed relative to each other during testing, ensuring aerodynamic loads to be transmitted directly and without distortion to the force/torque sensor for accurate measurements. With the instrumentation described, force and moment data were successfully captured real-time, enabling both static measurements and pitching moment trim tests.

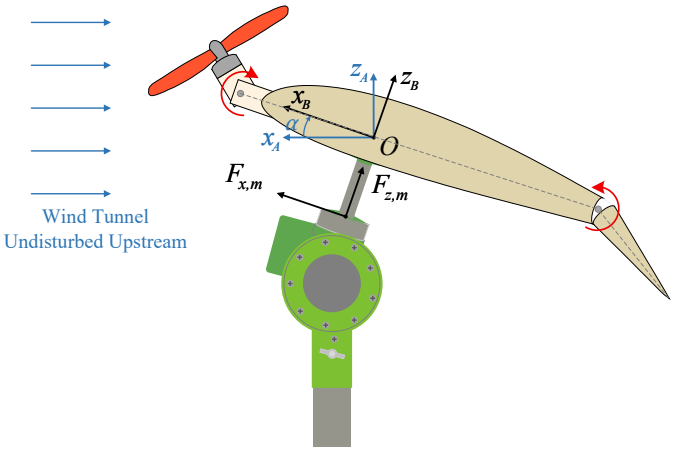

Figure 5.3: Wind tunnel experimental setup schematic figure showing the tilt-rotor tailsitter mounted on a six-axis force/torque sensor in the OJF wind tunnel, with a servo-driven mechanism to adjust angle of attack and red arrows suggesting the positive direction for rotor tilt and elevon deflection.

To quantify the aerodynamic forces and pitching moment acting on the tilt-rotor tailsitter, we define three coordinate frames: the measurement frame (x_m, y_m, z_m) fixed to the ATI force/torque sensor, the body frame (x_B, y_B, z_B) fixed to the drone, and the freestream aligned aerodynamic frame(x_A, y_A, z_A), with axis positive directions defined in Fig. 5.3. The sensor measurement frame follows the right-hand rule. Due to the mechanical installation of the force/torque sensor, a positive measured moment $M_{y,m}$ corresponds to a pitch-down rotation of the aircraft, which is opposite to the conventional aerospace sign convention. For the sake of consistency between the measurement frame and the body frame, the body axes (x_b, y_b, z_b) are defined to be aligned with the sensor axes (x_m, y_m, z_m). All forces and moments

reported in this paper strictly follow this coordinate definition. The reference point of forces and moment is defined at the drone's center of gravity, located 0.0357 m from the leading edge. To extract the net aerodynamic forces and pitching moment, including the effects of rotor thrust and aerodynamic loads, we remove the baseline gravitational contributions measured under no-wind conditions and measurements under wind for the bar that connects the drone and the sensor. The detailed calculation is shown as follows:

$$F_{x,B} = F_{x,m} - F_{x,m}^{(\mathrm{bw})} - \left(F_{x,m}^{(\mathrm{dg})} - F_{x,m}^{(\mathrm{bg})}\right), \tag{5.1}$$

$$F_{z,B} = F_{z,m} - F_{z,m}^{(\mathrm{bw})} - \left(F_{z,m}^{(\mathrm{dg})} - F_{z,m}^{(\mathrm{bg})}\right), \tag{5.2}$$

$$F_{x,A} = F_{x,B}\cos\alpha - F_{z,B}\sin\alpha, \tag{5.3}$$

$$F_{z,A} = F_{x,B}\sin\alpha + F_{z,B}\cos\alpha, \tag{5.4}$$

$$M_{y,B} = M_{y,m} - M_{y,m}^{(\mathrm{bw})} - F_{x,m}^{(\mathrm{dg})} \cdot d_{CG}. \tag{5.5}$$

Specifically, $F_{x,m}$ and $F_{z,m}$ denote the forces measured for the complete setup, the support bar and drone, under wind tunnel freestream conditions. The quantities $F_{x,m}^{(\mathrm{bw})}$ and $F_{z,m}^{(\mathrm{bw})}$ are measured for the bar alone under the same airspeed condition, which include both the aerodynamic loads on the bar and its gravitational components. In addition, $F_{x,m}^{(\mathrm{dg})}$ and $F_{z,m}^{(\mathrm{dg})}$ are obtained for the full setup with the wind tunnel powered off, which represent the combined gravitational forces of the bar and the drone. Finally, $F_{x,m}^{(\mathrm{bg})}$ and $F_{z,m}^{(\mathrm{bg})}$ are measured for the bar alone without wind tunnel freestream, corresponding to the bar's gravitational contribution. Therefore, the subtraction $F_{x,m} - F_{x,m}^{(\mathrm{bw})}$ removes the aerodynamic and gravitational effects of the bar from the total measurement, yielding the combined effect of the drone's aerodynamics, thrust and gravity. The subsequent term $F_{x,m}^{(\mathrm{dg})} - F_{x,m}^{(\mathrm{bg})}$ isolates the gravitational force acting on the drone. Subtracting this gravity term finally yields the resultant force acting on the drone excluding gravity, including both thrust and aerodynamic contributions, as is shown in and similarly for the z-axis. This procedure accounts for changes in the gravitational force components caused by variation of the angle of attack during the tests and ensures that only non-gravitational force contributions are retained. $M_{y,m}$ is the pitching moment measured by the sensor; $M_{y,m}^{(\mathrm{bw})}$ denotes the bar-alone pitch moment measured under wind and α, d_{CG} are respectively the angle of attack and the distance from the sensor measured surface to the drone's center of gravity is 0.95m.

5.3. Static Measurement Test

5.3.1. Static Test Matrix

The static wind tunnel experiments primarily aim to characterize the aerodynamic behavior of the tilt-rotor tailsitter under a representative range of flight and actuation conditions, with a particular focus on the influence of coupled actuator inputs on lift and pitching moment generation. The experimental campaign systematically explores how these aerodynamic forces and moments vary with key parameters including angle of attack (α), airspeed (V), motor throttle setting (T), elevon deflection (δ_e), rotor tilt angle (δ_t) and their coupling terms. This parameter space is also designed to capture the interaction between wing aerodynamics and rotor-induced flow, which plays a critical role in maneuvering performance and control authority.

Wind tunnel airspeeds of 15 and 18 m/s were selected as representative forward flight velocities for evaluating maximum lift capability and maneuvering performance. These values enable estimation of the maximum lift and corresponding minimum turning radius under realistic operating conditions. These discrete setpoints balance coverage of relevant dynamic pressure regimes with practical limitations on test duration. At each airspeed, the tilt-rotor tailsitter was tested across the range of 0° up to 20° with a 5° interval. This AoA range captures typical flight attitudes from level cruise to moderate pitching up, representative of initiating a high-g turn, but avoids deep stall or post-stall angles that are outside the scope of high-speed maneuvers. For each flight condition, the drone was subjected to various combinations of actuator configurations, specifically, 0, 30%, 40% and 45% for throttle level, 0, $\pm 15.75°$, $\pm 31.5°$, $\pm 47.25°$, $\pm 63°$ for elevon deflection and 0, $15.75°$, $31.5°$, $47.25°$ for rotor tilt). Each configuration lasted for 8 seconds and the mean force and moment values were recorded for further analysis.

5.3.2. Empirical Modeling of Aerodynamic Forces and Moments

To quantitatively describe the aerodynamic behavior of the tailsitter, empirical regression models are constructed to represent the overall lift, net axial force, and pitching moment as functions of rotor tilt angle (δ_t), motor throttle setting (T), elevon deflection (δ_e), angle of attack (α), and airspeed (V). All input variables are normalized using a range-based scaling approach defined on their physical operating envelopes. Specifically, each variable is linearly mapped from a representative physical range to a dimensionless interval of either $[0, 1]$ or $[-1, 1]$, as summarized

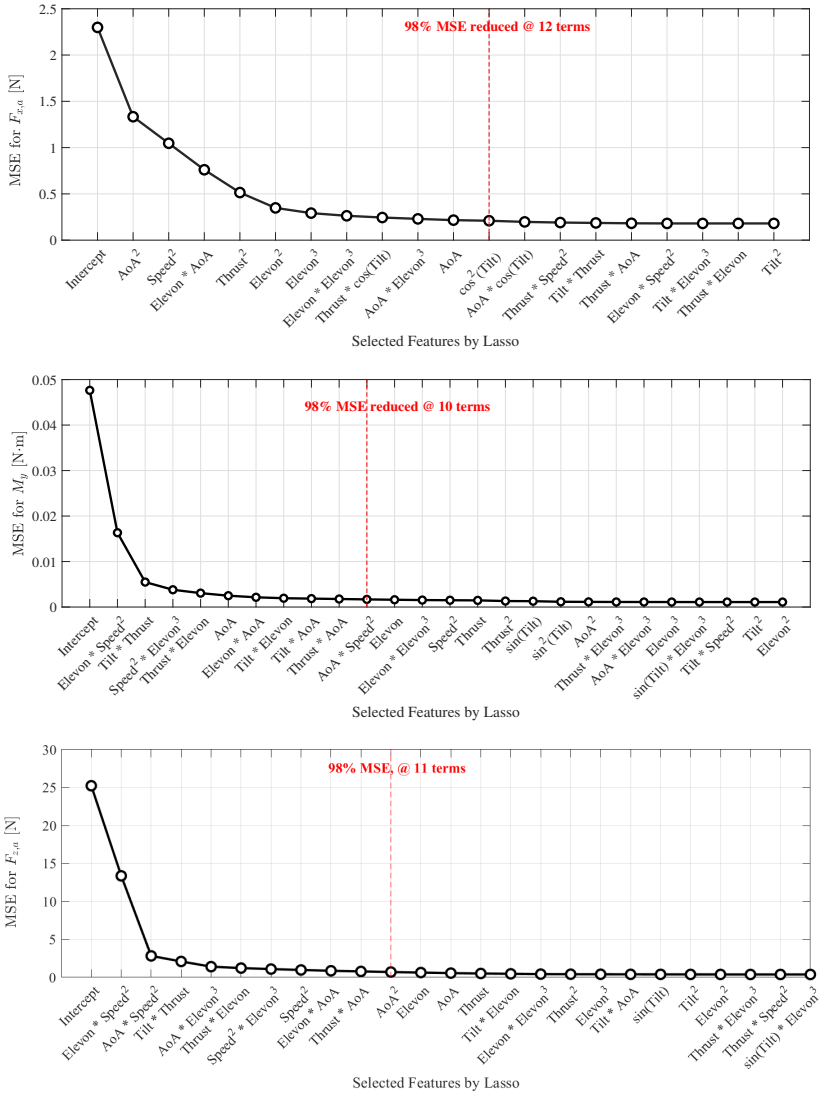

Figure 5.4: Mean squared error (MSE) convergence curves from build-up regression based on LASSO-selected features for $F_{Z,A}$, M_y and $F_{X,A}$. Features are incrementally added in order of their individual R^2 values. The red dashed line indicates the point where 98% of total MSE reduction is achieved.

in Table 5.1, such that the regression coefficients remain directly comparable across variables in terms of relative magnitude. Trigonometric terms are included to account for the nonlinear thrust vectoring introduced by tilt rotors, and a cubic term in elevon deflection is incorporated to capture the nonlinear degradation of control effectiveness at large deflections as described in our previous work [15].

Table 5.1: Summary of input variables, physical operating envelopes, and normalization scaling ranges used in the regression analysis.

Variable	Unit	Physical Range	Normalized Range	Scaling Type
δ_t	deg	$[0, 47.25]$	$[0, 1]$	Min-Max
α	deg	$[0, 20]$	$[0, 1]$	Min-Max
δ_e	deg	$[-63, 63]$	$[-1, 1]$	Center-Scale
V	m/s	$[0, 20]$	$[0, 1]$	Min-Max
T	-	$[0, 1]$	$[0, 1]$	Identity

By sweeping these parameters individually and in combination, the resulting empirical models incorporate linear, quadratic, and interaction terms, yielding a total of 35 candidate features in the initial regression pool. An initial feature selection is performed using the Least Absolute Shrinkage and Selection Operator (LASSO) regression [16], promoting sparsity while retaining predictive power. This reduces the candidate set to 24, 25, and 19 features for lift, pitching moment, and axial force, respectively, by eliminating irrelevant or redundant terms. The retained features are subsequently evaluated using a forward stepwise selection, as illustrated in Fig. 5.4. At each step, the feature that yields the largest reduction in mean squared error (MSE) is added to the model, producing an ordered ranking of explanatory importance based on marginal contribution to model accuracy. A cutoff criterion is then applied based on retaining 98% of the total achievable MSE reduction, defined as the difference between the intercept-only model and the model including all preselected features. Consequently, 12, 10, and 11 terms (including an intercept) are retained for $F_{X,A}$, $F_{M,y}$, and $F_{Z,A}$, respectively, striking a balance between estimation fidelity and model simplicity.

Based on these selected terms, the final multivariate polynomial models describing lift, pitching moment, and axial force as functions of angle of attack, airspeed,

throttle, rotor tilt, and elevon deflection are expressed as follows:

$$\begin{aligned} F_x(\alpha, V, T, \delta_e, \delta_t) = {} & C_{x0} + C_{x\alpha}\,\alpha + C_{x\alpha^2}\,\alpha^2 + C_{xV^2}\,V^2 + C_{xT^2}\,T^2 + C_{x\delta_e^2}\,\delta_e^2 \\ & + C_{x\delta_e\alpha}\,\delta_e\alpha + C_{x\delta_e^3}\,\delta_e^3 + C_{x\alpha\delta_e^3}\,\alpha\,\delta_e^3 + C_{x\delta_e^4}\,\delta_e^4 \\ & + C_{xT\cos\delta_t}\,T\cos(\delta_t) + C_{x\cos^2\delta_t}\,\cos^2(\delta_t) \end{aligned} \tag{5.6}$$

$$\begin{aligned} M_y(\alpha, V, T, \delta_e, \delta_t) = {} & C_{m0} + C_{m\alpha}\,\alpha + C_{m\delta_e\alpha}\,\delta_e\alpha + C_{m\delta_t\delta_e}\,\delta_t\delta_e \\ & + C_{m\delta_eV^2}\,\delta_eV^2 + C_{m\delta_tT}\,\delta_tT + C_{mV^2\delta_e^3}\,V^2\delta_e^3 + C_{mT\delta_e}\,T\delta_e \\ & + C_{m\delta_t\alpha}\,\delta_t\alpha + C_{mT\alpha}\,T\alpha. \end{aligned} \tag{5.7}$$

$$\begin{aligned} F_z(\alpha, V, T, \delta_e, \delta_t) = {} & C_{z0} + C_{z\delta_eV^2}\,\delta_eV^2 + C_{z\alpha V^2}\,\alpha V^2 + C_{z\delta_tT}\,\delta_tT \\ & + C_{z\alpha\delta_e^3}\,\alpha\delta_e^3 + C_{zT\delta_e}\,T\delta_e + C_{zV^2\delta_e^3}\,V^2\delta_e^3 \\ & + C_{zV^2}\,V^2 + C_{z\delta_e\alpha}\,\delta_e\alpha + C_{zT\alpha}\,T\alpha + C_{z\alpha^2}\,\alpha^2. \end{aligned} \tag{5.8}$$

The estimated coefficients of the scaled polynomial models are summarized in Table 5.2, providing a quantitative description of the static aerodynamic behavior of the tilt-rotor tailsitter under coupled variations of flight conditions and control inputs. The resulting models demonstrate high predictive accuracy, with coefficients of determination of 0.972, 0.963, and 0.915 for lift, pitching moment, and axial force, respectively. The corresponding root mean square errors are and 0.458 N for F_x, 0.042 Nm for M_y, and 0.604 N for F_z, indicating good agreement between the regression models and experimental data across the tested conditions. The identified terms reveal dominant aerodynamic trends as well as nonlinear cross-coupling effects between airspeed, rotor tilt, throttle, and elevon deflection.

For the axial-force $F_{X,A}$ model, both α and V^2 exhibit negative main effects, reflecting the increase of axial drag with larger angle of attack and airspeed. The negative quadratic term α^2 captures the quadratic rise in induced drag and the onset of flow separation in the post-linear regime. The throttle contribution is dominated by a strong positive quadratic term T^2, implying that thrust increases nonlinearly with throttle command in the axial direction, outweighing aerodynamic drag at higher throttle settings. With respect to elevon deflection, the dominant negative quadratic term (δ_e^2) captures the fundamental rise in profile drag with deflection. Notably, the positive fourth-order term (δ_e^4) acts as a saturation correction at large deflections. Furthermore, the interaction term $\alpha \cdot \delta_e$ carries a positive coefficient,

which suggests that deflecting the elevon upward at high angles of attack helps align the trailing edge with the local flow, thereby alleviating the drag penalty. Finally, the tilt effect enters the model primarily through the term $T \cdot \cos(\delta_t)$ with a strong positive coefficient, demonstrating that the axial force is governed by the geometric cosine projection of the rotor thrust vector.

Feature	**Coef. ($F_{X,A}$)**	**Coef. (M_y)**	**Coef. ($F_{Z,A}$)**
Intercept	2.6987	−0.0058	2.8861
α	−1.1582	−0.00545	—
α^2	−1.5623	—	−2.3414
$\delta_e \alpha$	2.6779	0.0819	3.6395
$\alpha \delta_e^3$	−1.1351	—	−1.1517
δ_e^4	1.7069	—	—
V^2	−4.8821	—	−3.9620
$\delta_e V^2$	—	−0.5346	−12.4090
αV^2	—	—	14.6860
δ_e^2	−2.8649	—	—
δ_e^3	−0.5078	—	—
$V^2 \delta_e^3$	—	0.2950	5.8411
T^2	4.1031	—	—
$T \delta_e$	—	−0.2427	−3.8545
$T \alpha$	—	−0.1070	3.2568
$\delta_t T$	—	−0.6293	4.9680
$\delta_t \delta_e$	—	−0.0580	—
$\delta_t \alpha$	—	−0.0664	—
$T_s \cos \delta_t$	1.9693	—	—
$\cos^2 \delta_t$	−0.3291	—	—
Model R^2	0.915	0.963	0.972
RMSE	$0.458N$	$0.042Nm$	$0.604N$

Table 5.2: Regression coefficients of the scaled polynomial models for axial force $F_{X,A}$, pitching moment M_y, and lift $F_{Z,A}$.

For the pitching-moment model M_y, both elevon deflection δ_e and rotor tilt δ_t play dominant roles, together with their coupling with airspeed and thrust. It should be noted that due to the sensor mounting orientation, negative M_y corresponds to

a pitch up moment in the body frame. The aerodynamic control authority is captured primarily by the interaction term $\delta_e V^2$ with a negative coefficient, confirming that control effectiveness scales with dynamic pressure. The nonlinear saturation of elevon control authority is modeled by the velocity-weighted cubic term $V^2\delta_e^3$ (positive coefficient) in strongly deflected, high speed conditions. Furthermore, the significant term $T\delta_e$ indicates that increasing throttle enhances the pitching moment generated by elevon deflection even at low airspeeds, consistent with the propeller slipstream energizing the flow over the control surface. The structure of the identified model provides compelling empirical support for the proposed trim strategy of utilizing downward elevon deflection to counteract the moment induced by upward rotor tilt. The dominant bilinear term $\delta_t T$ exhibits a large negative coefficient, confirming that increasing throttle in a tilt-up configuration ($\delta_t > 0$) introduces a powerful pitch up moment via the inclined thrust vector. Maintaining equilibrium therefore requires a counter-acting positive (pitch down) moment. By applying a downward elevon deflection ($\delta_e < 0$), the primary control term $\delta_e V^2$ yields a positive contribution, providing the necessary opposing pitch down moment to the thrust vector. Further interaction terms involving $\delta_t\delta_e$ and $\delta_t\alpha$ with moderate coefficients indicate that rotor tilt modifies the local angle of attack and loading on the wing and elevon, so that the pitching moment is sensitive to the combined setting of rotor tilt, elevon deflection and angle of attack.

For the identified empirical model of $F_{Z,A}$, the lift is governed primarily by angle of attack α, elevon deflection δ_e, airspeed V, and thrust vectoring effects, reflecting the combined aerodynamic and propulsive nature of the tailsitter configuration. The dominant coefficients of the terms αV^2 and $\delta_e V^2$ confirm that the primary lift generation scales significantly with dynamic pressure. However, the quadratic term α^2 implies the onset of nonlinear lift degradation at higher angle of attack, reflecting the early stall characteristics and flow separation. The model also captures saturation effects through the velocity-weighted cubic term $V^2\delta_e^3$ and the interaction term $\alpha\delta_e^3$, further suggesting that at higher angles of attack, excessive elevon deflection becomes less effective in augmenting lift, likely due to the combined effects of flow separation on the control surface and propeller slipstream distortion. Notably, rotor tilt affects the lift generation through two competing mechanisms. On one hand, tilting the rotor upward increases the vertical component of thrust, thereby directly contributing to lift via thrust vectoring. On the other hand, rotor tilt also alters the local inflow direction over the wing, reducing the local angle of attack and hence decreasing the aerodynamic lift component. The positive coefficient of the term

$\delta_t T$ confirms that the thrust induced vertical force outweighs the loss of wing lift caused by local angle of attack reduction under the tested conditions. This demonstrates that, for a tilt-rotor configuration, thrust vectoring plays a leading role in supporting lift, while the adverse aerodynamic effect associated with local angle of attack reduction remains secondary. Furthermore, the interaction term $T \cdot \alpha$ indicates that lift sensitivity to throttle increases at higher angles of attack, suggesting a strengthened coupling between propeller-induced flow and wing aerodynamics under elevated aerodynamic loading. Collectively, the structure of the identified model supports the central hypothesis that coordinated deployment of upward rotor tilt and downward elevon deflection enables efficient lift augmentation while preserving pitch controllability across the operating envelope, thereby supporting the proposed trim strategy for the tilt-rotor tailsitter configuration.

To visualize these effects, Figure 5.5 presents the fitted response surface of lift force (F_z) under fixed airspeed $V = 18$ m/s and throttle $T = 40\%$, evaluated at angles of attack $\alpha = 0^\circ$, 5°, 10°, 15°, and 20°. Each subfigure overlays the model predictions with the corresponding measured data points. The lift surface derived from the fitted model matches the experimental measurements well across the full actuator space, demonstrating the local accuracy of the fitted model. Across all five cases, a consistent trend is observed that upward rotor tilt in combination with downward elevon deflection reaches the highest lift, confirming that the coordinated use of both elevons and rotor tilt can increase the maximum lift of a tailsitter compared to either actuation alone. In addition, increasing angle of attack from 0° to 20° steadily enhances the lift magnitude, reflecting the growing aerodynamic contribution from the wing at higher incidence. These results confirm that the model captures not only the effectiveness of individual actuators but also their interaction with flight condition, providing a reliable basis for moment equilibrium analysis and maneuver envelope prediction.

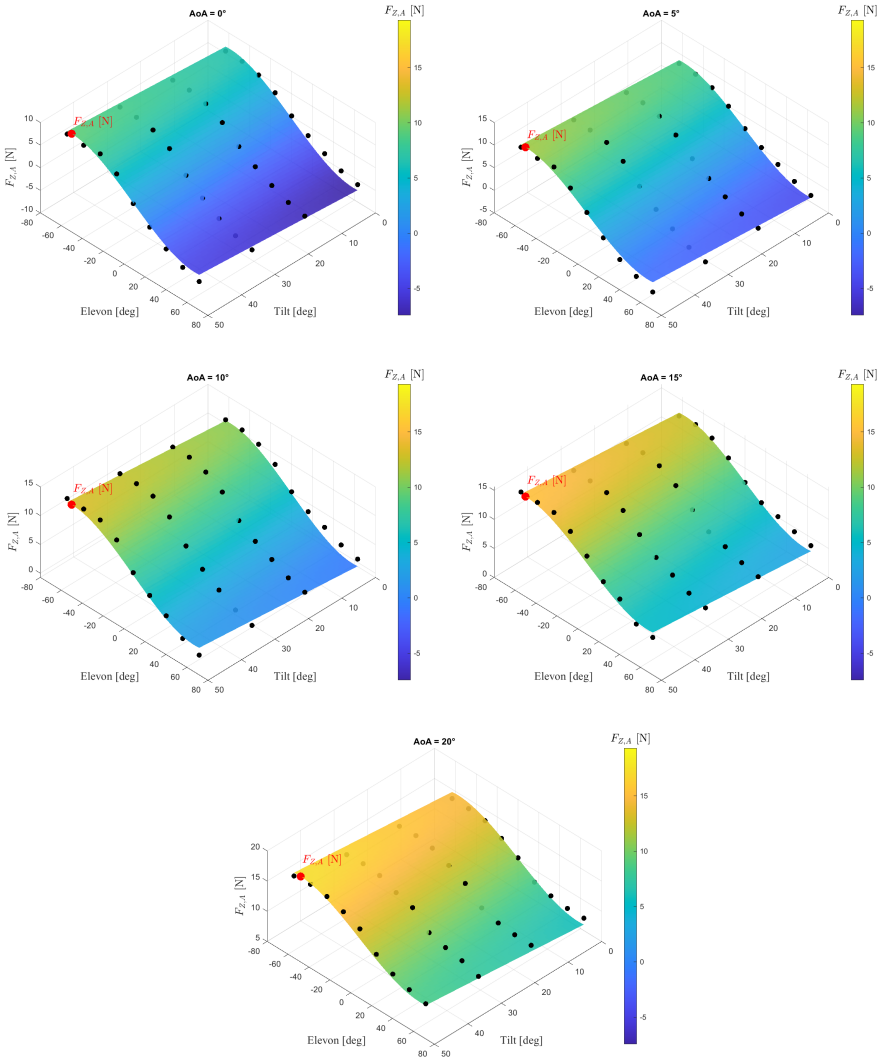

Figure 5.5: Fitted response surfaces of lift force (F_z) under $V = 18$ m/s and $T = 40\%$, evaluated at $\alpha = 0°$, $5°$, $10°$, $15°$, and $20°$. Each subfigure shows the predicted lift across rotor tilt and elevon deflection, with overlaid experimental data points.

5.4. Enhanced lift with pitch moment equilibrium

Building on the empirical model developed from the static parameter sweep wind tunnel tests, the response surface analysis confirmed that upward rotor tilt and downward elevon deflection together contribute to increased lift. To further assess whether this lift-enhancing combination can also satisfy pitch moment equilibrium,

a series of wind tunnel tests aimed at real-time moment trimming was carried out at an airspeed of 18 m/s, which corresponds to typical forward flight as observed in prior outdoor experiments. For each angle of attack ($\alpha = 0^\circ$, 5°, 10°, 15°, 20°, and 25°), the throttle was held constant at 45%, and the rotor tilt and elevon deflection were adjusted to reach a near-zero pitching moment, defined by $|M_y| < 0.02\ \mathrm{Nm}$. A closed-loop PID controller was employed to dynamically adjust the actuator settings using real-time feedback to satisfy the constraint above.

The pitching moment trimming process proceeded in three configurations to explore the role of different control strategies. First, to represent a E-tailsitter, the elevon was actuated while keeping the rotor tilt fixed at neutral ($\delta_t = 0^\circ$), effectively using control surface deflection to offset the inherent pitch up or down moments from wing aerodynamics. Second, to characterize a TR-tailsitter, the reverse strategy was applied: elevon deflection was held at zero while the rotor tilt angle was varied to balance the pitch moment, leveraging the thrust vectoring effect of the tilted rotors. Finally, to analyze a TRE-tailsitter, a set of combined actuation tests were performed, where for each discrete rotor tilt angle ($\delta_t = 15.75^\circ, 31.5^\circ, 47.25^\circ$), the elevon deflection was tuned dynamically to achieve moment balance. This last configuration directly tests the hypothesis that synergistic use of rotor tilt and elevon deflection can achieve pitch moment equilibrium with higher net lift than either control input alone.

Figure 5.6 illustrates actuator combinations of elevon deflection and rotor tilt angle enabling pitch moment equilibrium for the three tailsitter categories, at 45% throttle, 18m/s aispeed and different angles of attack. Across all configurations, the elevon deflection or the rotor tilt angle required for moment equibrilium increases with angle of attack. For the TRE-tailsitter, at low to moderate angles of attack, or at higher angles of attack with moderate rotor tilt, the elevons are able to counteract the pitch up moment induced by upward rotor tilt, achieving successful pitch moment trimming. However, when the angle of attack exceeds 15° and rotor tilt becomes large, the elevon rapidly saturates and no pitch equilibrium can be further achieved, which suggests that the wing stalls and flow separation occurs at the elevons in these cases. This limitation highlights the importance of actuator coordination and the trade-off between lift enhancement and moment controllability.

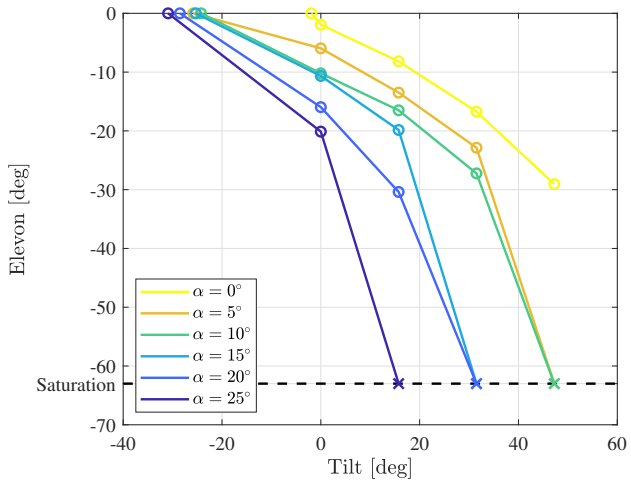

Figure 5.6: Rotor tilt and elevon deflection combinations achieving pitch moment equilibrium ($|M_y| < 0.02$ Nm) at various angles of attack under $V = 18$ m/s and 45% throttle. Open circles denote successful pitch moment trims; crosses indicate elevon saturation ($\delta_e = -63°$).

5

To further investigate the interaction between actuator inputs, lift generation, and pitching moment behavior, a series of contour plots was generated from the empirical model, as shown in Figure 5.7. Each subplot depicts the predicted lift force $F_{Z,A}$ varying with rotor tilt and elevon deflection at a fixed throttle setting of 45% and airspeed of 18 m/s and different angles of attack. Superimposed on the lift contours are black dashed lines representing the pitching moment bounds $M_y = \pm 0.02$ Nm, which are consistent with the moment equilibrium threshold used in the pitching moment trim experiments.

The plots reveal that pitch equilibrium is consistently achieved through coordinated actuator settings combining upward rotor tilt and downward elevon deflection. This actuator pairing not only satisfies moment balance but also yields substantially higher lift. As the angle of attack increases from $0°$ to $20°$, the global lift magnitude rises as expected. However, the moment equilibrium contour progressively bends toward the elevon saturation boundary at higher angles of attack, indicating that moderate rotor tilt angles are sufficient to drive the elevon toward its actuation limit, consistent with the findings from pitching moment trim tests. This behavior suggests that while high angle of attack benefits lift generation, it imposes a rapidly increasing demand on the elevon's pitch down authority to counteract the pitch up moment brought by upward rotor tilt, thereby narrowing the available control margin.

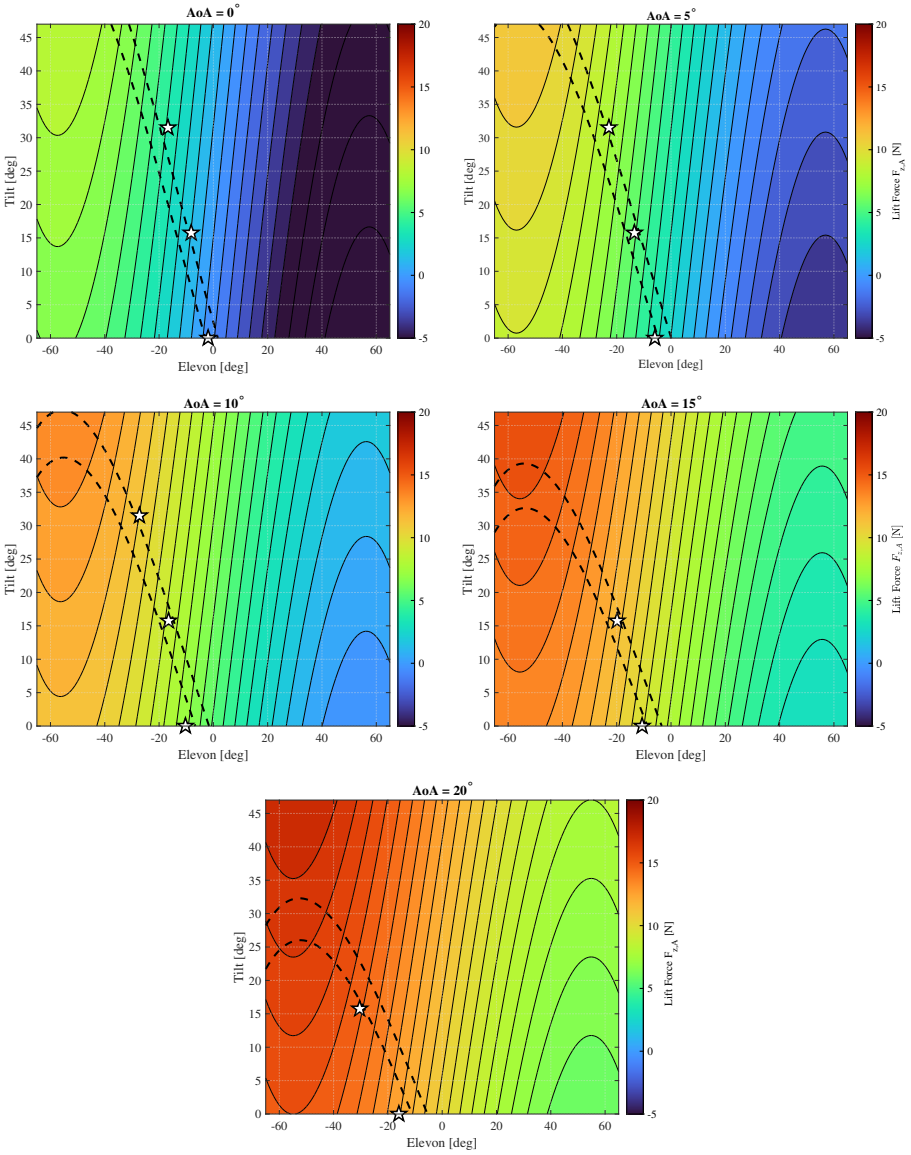

Figure 5.7: Lift contour maps overlaid with allowable pitch equilibrium threshold ($|M_y| \leq 0.02Nm$) at angles of attack $\alpha = 0^\circ$, 5°, 10°, 15°, and 20°, under $V = 18$ m/s and 45% throttle. Each plot shows the predicted lift force ($F_{Z_{\mathbb{B}A}}$) as a function of rotor tilt and elevon deflection, based on the empirical model. The black dash lines indicate trimmed moment threshold contours and stars represent the measurements from the pitching moment trim test under the same flight condition.

Furthermore, the white stars denote actuator combinations satisfying pitch moment equilibrium measured during the above mentioned pitch-trim wind tunnel

experiments, corresponding to open circle points in Figure 5.6. Notably, under the same flight condition of 45% throttle and 18m/s airspeed, these points fall within the $M_y = \pm 0.02$ contour bands predicted by the empirical model, thereby validating the model's accuracy in capturing the effect of actuator configurations on the aerodynamics of the TRE-tailsitter.

To achieve a sharp coordinated turn without losing speed, it is critical to ensure non-negative axial force. Figure 5.8 illustrates the minimum throttle required to maintain positive axial force across various combinations of rotor tilt and elevon deflection, under fixed airspeed ($V = 18$ m/s) and different angles of attack. A consistent trend is observed where higher angles of attack necessitate greater throttle input, reflecting the increased aerodynamic drag associated with high angle of attack. A general monotonic trend is observed in which the minimum throttle requirement increases with rotor tilt, as a larger fraction of thrust is progressively redirected from the axial to the vertical direction. However, the sensitivity of required throttle to rotor tilt is not uniform across the entire range. At moderate tilt angles, approximately $0°$–$25°$, the throttle contours become noticeably flatter, suggesting a regime in which the adverse effect of thrust projection loss is partially mitigated by favorable aerodynamic interactions between the propeller slipstream and the wing, potentially improving boundary-layer attachment and reducing effective drag. Beyond this region, the throttle demand rises rapidly with further increases in rotor tilt, reflecting the dominance of geometric projection loss of thrust in the axial direction.

The influence of elevon deflection on the axial-force balance becomes particularly pronounced at high angles of attack. As shown in Fig. 5.8, at low angles of attack, the minimum throttle requirement exhibits relatively weak sensitivity to elevon deflection. However, as the angle of attack increases, a clear asymmetry emerges between upward and downward deflections. In the high angle of attack regime, downward elevon deflection leads to a rapidly increasing throttle demand. For excessively large downward deflections, the required throttle approaches the saturation boundary imposed by the propulsion system. This behavior reflects the combined effect of increased profile drag, enhanced downwash curvature, and deterioration of flow attachment at large negative deflections. In contrast, configurations with upward elevon deflection remain within the achievable throttle envelope even at high angles of attack. Overall, the results reveal that at high angles of attack, downward elevon deflection represents a critical limiting factor for axial-force sustainability, whereas upward deflections retain a greater operational margin in terms of propulsion demand.

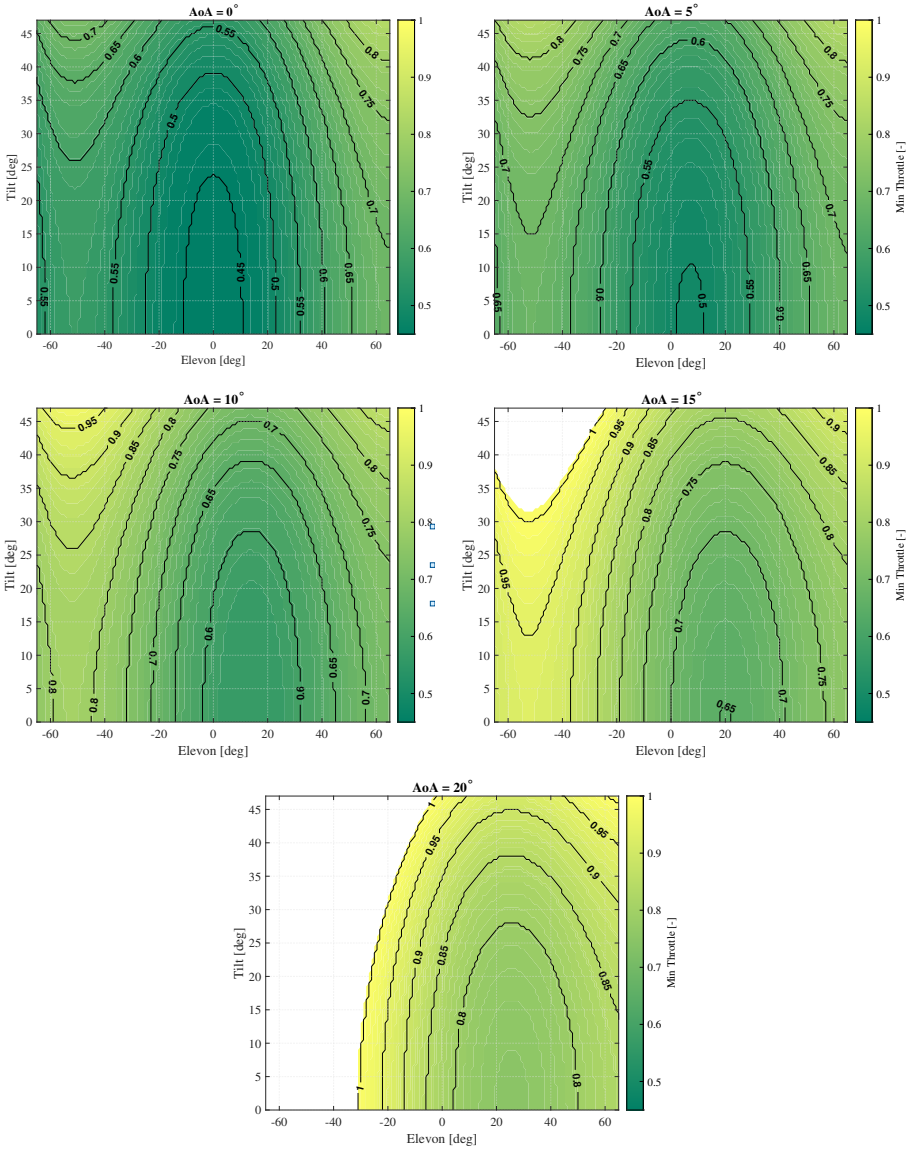

Figure 5.8: Contour plots for the minimum throttle required to sustain positive axial force across rotor tilt and elevon deflection combinations at various angles of attack ($\alpha = 0° \sim 20°$), under $V = 18$ m/s.

5.5. Minimum Radius for High-Speed Sharp Turn

In a high-speed coordinated turn, the aircraft must generate a sufficient lift force in order to provide the centripetal force required to sustain the maneuver, while simultaneously maintaining a stable pitch attitude. To keep consistent with the wind tunnel testing conditions where dynamic pitching was absent, we assume that the rotational pitch rate q has no effect on aerodynamic forces and moments. To identify actuation strategies that enable sharp turning, a parametric search was performed using the empirical aerodynamic models derived in Section 5.3.2 over the actuator space spanned by rotor tilt and elevon deflection. The analysis focused on a forward flight condition representative of a high-speed coordinated turn, using a representative airspeed of 18 m/s within the angle of attack range of 0° to 20°. For each candidate combination (δ_t, δ_e), an inner search was conducted over angle of attack α and throttle setting T to identify feasible operating points satisfying both the pitching moment equilibrium condition $|M_y| \leq 0.02$ Nm and the axial-force constraint $|F_{X,A}| \leq 0.1$ N. This effectively simulates the constraints of a banked turn, where both pitch moment stability and lift generation must be ensured while maintaining the forward speed.

Among all angle of attack and throttle pairs (α, T) at a given actuator configuration, the maximum achievable lift was extracted and defined as the local maximum lift associated with that (δ_t, δ_e) point. By repeating this procedure throughout the (δ_t, δ_e) grid, a contour map of local maximum lift over the actuator space was constructed, as shown in Fig. 5.9. It is important to note that each point on this map corresponds to a distinct combination of optimal angle of attack and throttle setting, rather than a common operating condition shared across the figure.

The red star markers in Fig. 5.9 highlight two groups of representative local optima, which compares the locally optimal lift both across rotor tilt at fixed elevon deflection and across elevon deflection at fixed rotor tilt. For each starred actuator setting (δ_t, δ_e), the corresponding optimal angle of attack, throttle command, and predicted lift level (α, T, F_z) are explicitly annotated in the figure, emphasizing that every point on the contour map is associated with its own optimal operating condition in (α, T) rather than a single global flight condition. The global maximum lift, obtained by comparing all local optima across the actuator space, is denoted by the red hexagram in Fig. 5.9. This optimum occurs at an angle of attack of 18°, a throttle setting of 100%, a rotor tilt of 19°, and an elevon deflection of -63°, yielding a maximum lift of 20.35 N, corresponding to approximately 4.25 times the vehicle weight ($m = 0.489$ kg). This result confirms that the vehicle is capable

of generating sufficiently large lift forces to sustain aggressive coordinated turns under actuator and equilibrium constraints.

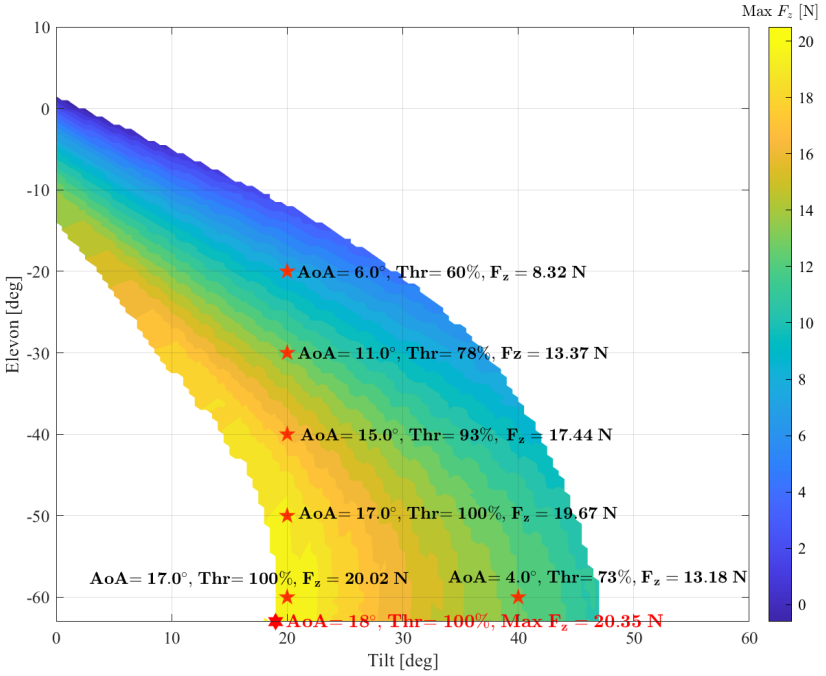

Figure 5.9: Maximum lift force ($F_{Z,A}$) achievable across rotor tilt and elevon deflection combinations at 18 m/s airspeed, while satisfying $|F_{X,A}| < 0.1N$ and $|M_y| < 0.02Nm$. The red Hexagram denotes the global maximum lift point and the red stars represent local maximum lift points.

Building on the identified maximum lift and its corresponding actuator configuration, we proceed to compute the minimum turning radius for a coordinated turn. By projecting the gravity defined in the East-North-Up inertial frame and the aerodynamic force defined in the aerodynamic frame (as defined in Fig. 5.3) onto the trajectory frame, the following expressions are obtained:

$$F_G = \begin{bmatrix} \cos\gamma & 0 & -\sin\gamma \\ 0 & 1 & 0 \\ \sin\gamma & 0 & \cos\gamma \end{bmatrix} \begin{bmatrix} \cos\xi & \sin\xi & 0 \\ -\sin\xi & \cos\xi & 0 \\ 0 & 0 & 1 \end{bmatrix} \begin{bmatrix} 0 \\ 0 \\ -mg \end{bmatrix}, \tag{5.9}$$

$$F_A = \begin{bmatrix} 1 & 0 & 0 \\ 0 & \cos\mu & \sin\mu \\ 0 & -\sin\mu & \cos\mu \end{bmatrix} \begin{bmatrix} -D \\ Y \\ L \end{bmatrix}, \tag{5.10}$$

where γ is the flight path angle, ξ is the aerodynamic heading angle, and μ is the aerodynamic bank angle, and D, Y, and L denote drag, side force, and lift, respectively. Consequently, the resultant force acting on the drone in the trajectory frame is given by

$$F_T = F_G + F_A = \begin{bmatrix} mg\sin\gamma - D \\ Y\cos\mu + L\sin\mu \\ -mg\cos\gamma - Y\sin\mu + L\cos\mu \end{bmatrix}. \tag{5.11}$$

Here, it is assumed that the aircraft is in a level flight phase, with a flight-path angle of zero, i.e., $\gamma = 0$. Furthermore, for symmetric aircraft, e.g. the proposed TRE-tailsitter, under normal flight conditions without sideslip, the aerodynamic side force Y is considered negligible. Therefore, the forces acting on the aircraft in the trajectory frame can be simplified as

$$F_T = \begin{bmatrix} -D \\ L\sin\mu \\ -mg + L\cos\mu \end{bmatrix}. \tag{5.12}$$

The force along the Y-axis of the trajectory frame provides the centripetal force required for turning, and the force along the Z-axis is zero due to the assumption of level flight. Accordingly, it follows that $\cos\mu = \frac{mg}{L}$, and thus $|\sin\mu| = \sqrt{1 - \frac{m^2g^2}{L^2}}$. As a result, the turning radius can be calculated by the following formula:

$$R = \frac{mV^2}{|L\sin\mu|} = \frac{mV^2}{\sqrt{L^2 - m^2g^2}}. \tag{5.13}$$

Given the achievable maximum lift of $20.351N$ under the condition of pitch moment equilibrium and near-zero axial force, the theoretical minimum turning radius for a 0.489 kg TRE-tailsitter during a $18m/s$ coordinated turn is calculated by Eq.5.13 as $8.01m$.

5.6. Conclusion

This study experimentally quantifies the coupled effects of rotor tilt and elevon deflection on a tilt-rotor tailsitter through extensive wind-tunnel measurements and empirical modeling. The results show that coordinated use of upward rotor tilt and downward elevon deflection enables substantial lift augmentation while maintaining pitch equilibrium. However, this benefit is constrained by elevon saturation at high angles of attack, as increasing aerodynamic loading drives the required pitch down authority beyond actuator limits. This reveals a fundamental tradeoff between lift maximization and pitch controllability that governs the feasible trim envelope of the tilt-rotor tailsitter.

By embedding the derived aerodynamic models into a parametric equilibrium constrained performance analysis, the study yields generalizable insight into actuator coordination for agile maneuvers. The theoretical minimum turning radius at 18 m/s of the tilt-rotor tailsitter is found to be 8.01 m, occurring at high angle of attack, full throttle, moderate upward rotor tilt, and maximum downward elevon deflection. These results demonstrate that aggressive turning performance is realized not through extreme reliance on a single actuator, but through balanced allocation between thrust vectoring and aerodynamic control surfaces. The findings provide experimental evidence for actuator synergy in hybrid VTOL aircraft and offer a practical framework for performance-oriented control allocation and envelope exploitation in tilt-rotor tailsitter designs.

Future work will extend the present findings through outdoor flight experiments, focusing on high-speed turning maneuvers to validate the predicted optimal configurations under realistic conditions. These tests will assess not only aerodynamic model fidelity but also the impact of actuator dynamics, control bandwidth, and environmental uncertainty on achievable maneuver performance.

References

[1] J. Zhong and W. Chen, "Transition characteristics for a small tail-sitter unmanned aerial vehicle", *Chinese Journal of Aeronautics*, vol. 34, no. 10, pp. 220–236, 2021.

[2] E. A. Islas-Narvaez, J. F. Ituna-Yudonago, L. E. Ramos-Velasco, M. A. Vega-Navarrete, and O. Garcia-Salazar, "Design and determination of aerodynamic coefficients of a tail-sitter aircraft by means of cfd numerical simulation", *Machines*, vol. 11, no. 17, pp. 1–24, Jan. 2023.

[3] K. Anuar, W. Fatra, A. Asral, N. Nazaruddin, and M. Taslim, "Preliminary design of tail-sitter UAVs", in *3rd Conference on Innovation in Technology and Engineering Science (CITES)*, AIP Publishing, vol. 2891, May 2022, pp. 1–11.

[4] E. A. Tal and S. Karaman, "Global trajectory-tracking control for a tailsitter flying wing in agile uncoordinated flight", in *AIAA Aviation 2021 Forum*, AIAA, Jul. 2021, pp. 1–20.

[5] G. H. Lovell-Prescod, Z. Ma, and E. J. J. Smeur, "Attitude control of a tilt-rotor tailsitter micro air vehicle using incremental control", in *2023 International Conference on Unmanned Aircraft Systems (ICUAS)*, IEEE, Jun. 2023, pp. 842–849.

[6] Z. Ma, E. J. J. Smeur, and G. C. H. E. De Croon, "Design and control of a tilt-rotor tailsitter aircraft with pivoting vtol capability", *IEEE Robotics and Automation Letters*, 2025.

[7] P. Aref, M. Ghoreyshi, A. Jirasek, M. J. Satchell, and K. Bergeron, "Computational study of propeller–wing aerodynamic interaction", *Aerospace*, vol. 5, no. 3, p. 79, 2018.

[8] S. Taniguchi and A. Oyama, "Numerical analysis of propeller mounting position effects on aerodynamic propeller/wing interaction", in *AIAA SciTech 2022 Forum*, 2022, p. 0153.

[9] R. H. Stone, "Aerodynamic modeling of the wing-propeller interaction for a tail-sitter unmanned air vehicle", *Journal of Aircraft*, vol. 45, no. 1, pp. 198–210, 2008.

[10] S. Srivathsan and J. Rauleder, "Experimental wind tunnel investigation on propeller-wing interactional aerodynamics", in *AIAA SCITECH 2023 Forum*, 2023, p. 1752.

[11] L. L. M. Veldhuis, "Propeller wing aerodynamic interference", *TU Delft Repository*, 2005.

[12] F. M. Catalano, "On the effects of an installed propeller slipstream on wing aerodynamic characteristics", *Acta Polytechnica*, vol. 44, no. 3, 2004.

[13] X. Chen, Z. Zhou, and W. Hongbo, "Investigation on approach to control lift distribution of wing by distributed propellers", in *Proceedings of the 31st Congress of the International Council of the Aeronautical Sciences, Belo Horizonte, Brazil*, 2018, pp. 9–14.

[14] H. Alons, "Ojf external balance documentation", *Nationaal Lucht en Ruimtevaartlaboratorium*, 2008.

[15] Z. Ma, E. J. J. Smeur, and G. C. H. E. de Croon, "Wind tunnel tests of a wing at all angles of attack", *International Journal of Micro Air Vehicles*, vol. 14, 2022.

[16] R. Tibshirani, "Regression shrinkage and selection via the lasso", *Journal of the Royal Statistical Society Series B: Statistical Methodology*, vol. 58, no. 1, pp. 267–288, 1996.

6

Conclusion

6.1. Answers to Research Questions

This dissertation set out to address four key research questions about the aerodynamics, control, and agility of tilt-rotor tailsitter UAVs. Each question was tackled in Chapters 2–5, and the findings are summarized as follows:

Research Question 1

How does a tailsitter wing behave aerodynamically across different actuator settings, airspeeds, and all angles of attack, and how do these conditions affect its lift and moment generation as well as the control effectiveness of elevons?

Chapter 2 presents a comprehensive wind tunnel test to characterize the wing's aerodynamics across the full range of angles of attack (AoA), under various settings of thrust throttle, elevon deflection, and airspeed. The resulting dataset, the first of its kind for a tailsitter wing, reveals aerodynamic forces and moments at all angles of attack, including stall, post-stall, and inverse flow conditions. In particular, the data confirm that elevon deflections exert strong influence on lift and pitching moment at low angles of attack, where elevon control effectiveness is most pronounced. However, at high angles of attack and low airspeeds, the control authority of elevons decreases substantially. In inverse flow conditions, such as during descent, elevon deflections affect the pitch moment in the opposite direction compared to the normal flow case. This reversed effect can be mitigated by increasing the throttle setting, which helps restore the expected control response.

These findings answer RQ1 by quantifying the tailsitter wing's aerodynamic force and moment generation at all angles of attack and by highlighting that elevon effectiveness diminishes significantly at high AoA or low airspeeds. This insight lays the aerodynamic foundation for the rest of the research and underlines the need for alternative or augmented actuation in low-speed, high-AoA flight regimes.

Research Question 2

How to design an actuation system and control allocation strategy that guarantees sufficient control authority across all flight phases of a hybrid tailsitter UAV, including hover, transition, and forward flight?

Chapters 3 and 4 address this question by refining the actuation architecture and control strategy to ensure full-envelope autonomous flight without actuator saturation. Chapter 3 introduces a tilt-rotor (TR) tailsitter equipped with dual tilting rotors and no aerodynamic control surfaces, governed by an Incremental Nonlinear Dynamic Inversion (INDI) attitude controller. Flight tests demonstrate that thrust vectoring alone provides sufficient pitch authority, effectively preventing the saturation typically observed in conventional E-tailsitters (tailsitters with only aerodynamic control surfaces that function like elevons). However, the absence of aerodynamic control surfaces limits roll authority during fast forward flight.

To overcome this, Chapter 4 proposes a TRE-tailsitter that integrates dual tilting rotors with conventional elevons. A weighted least squares (WLS) control allocation scheme coordinates the actuators across the envelope: rotor tilt dominates at low speeds, while elevons progressively assume control at higher speeds. This ensures actuator authority is preserved without over-reliance on any single component.

The tilt-rotor-elevon configuration, implemented with a cascaded INDI controller, achieves full-envelope autonomous flight including vertical climb and descent, 16 m/s cruise, and seamless transitions between them without control saturation. Comparative tests confirm that a TRE-tailsitter outperforms single-actuator designs. In forward flight, roll authority is significantly improved compared to a TR-tailsitter. During vertical flight and particularly in descent, pitch control remain more effective than that of an E-tailsitter.

In conclusion, RQ2 is addressed by the complementary use of tilting rotors and elevons, coordinated through adaptive allocation. This dual-actuation design resolves the long-standing saturation issue and enables sufficient control authority across all flight regimes.

Research Question 3

How to achieve robust and fully autonomous vertical takeoff and landing for a hybrid tailsitter UAV in unstructured environments with wind disturbances and irregular terrain?

Chapter 4 also addresses the challenge of achieving autonomous VTOL operations in the presence of wind disturbances and uneven terrain. This is accomplished through a pivoting takeoff and landing mechanism that utilizes the tilt-rotor system. Rather than requiring the vehicle to begin in an upright orientation, the TRE tailsitter initiates flight from a horizontal resting pose. By tilting its rotors, the tilt-rotor tailsitter lifts itself off the ground by pivoting around its tail.

This maneuver is regulated by a dedicated pivoting controller that controls the drone's pitch attitude during ground operations. It removes the need for additional landing gears or manual intervention. Indoor and outdoor experiments confirm that the pivoting approach enables fully autonomous takeoffs and landings. Wind rejection tests further demonstrate that the proposed method maintains stability under wind disturbances, where conventional tailsitters might lose balance or fail to initiate flight. The ability to reliably perform vertical takeoff and landing without external assistance directly addresses RQ3, and advances the operational readiness of tailsitter UAVs for deployment in unstructured environments.

Research Question 4

How to exploit wing–propeller interactions through optimal actuator configurations to enable agile maneuvers, such as sharp turns, without sacrificing forward speed?

Chapter 5 investigates the agility of the tilt-rotor tailsitter, with a particular focus on sharp high-speed turns. Such maneuvers demand minimal turning radius, which in turn requires maximizing the lift generated during coordinated turning flight. To achieve this, wind tunnel experiments were conducted to characterize the (overall) lift force and pitch moment under systematic variations of actuator combinations. An empirical model has been developed to describe lift and pitch moment as functions of angle of attack, airspeed, thrust, rotor tilt angle, and elevon deflection, revealing the complex coupling between wing-propeller interaction.

In addition, dynamic balance wind tunnel tests were performed, in which upward rotor tilt was paired with downward elevon deflection to maintain pitch mo-

ment equilibrium while increasing lift. This actuator combination has been shown to be optimal for generating the required centripetal force during coordinated turns. Accordingly, a theoretical minimum turning radius of $8.01m$ for coordinated sharp turns was derived by the established empirical aerodynamic model at a representative flight speed of 18 m/s.

These findings directly address RQ4 by demonstrating that coordinated use of thrust vectoring and control surface deflection enables agile maneuvering without compromising forward velocity. The study establishes a data-driven aerodynamic framework for analyzing and planning aggressive turning maneuvers, supported by quantitative insights into actuator-induced aerodynamic coupling.

With the research questions addressed, we now synthesize the findings to assess how the overall research objective has been achieved in an integrated and systematic manner.

Research Goal

To develop a tailsitter UAV with sufficient control authority to enable autonomous, robust, and precise flight across the entire flight envelope, including vertical takeoff and landing, hover, forward flight, and all transitional phases. The research further aims to investigate the vehicle's capability for agile maneuvers such as sharp turns.

On Airframe Design and Control Authority

- E-tailsitter: Suffers from low pitch control in vertical/descending flight due to ineffective elevons at low airspeed.
- TR-tailsitter: Thrust vectoring enhances pitch control effectiveness but lacks roll control authority in forward flight.
- TRE-tailsitter: Combines tilt rotors and elevons, achieving full-envelope control with no actuator saturation.

On Full-Envelope Autonomous Flight

- Pivoting VTOL: A dedicated controller exploits rotor tilt to pitch the vehicle around its tail for takeoff and landing, eliminating external landing gears and ensuring wind robustness.
- Cascaded INDI: Weighted Least Squares control allocation coordinates actuators across all flight regimes, enabling smooth transitions and stable flight.

On Agile Maneuvering in Sharp Turns

- Empirical Modeling: Wind tunnel tests quantify lift and moment over varied actuator settings.
- Optimal Coordination: Upward rotor tilt combined with downward elevon yields maximum coordinated lift and minimum turning radius.

To conclude, this dissertation advances the design and control of hybrid VTOL UAVs by addressing the challenges of actuator authority, full-envelope autonomous flight and aerodynamic characterization. Through an integrated approach combining mechanical design, experimental validation, and control development, this work deepens the understanding of tailsitter dynamics and enables reliable operation across all flight regimes. These findings lay a foundation for the deployment of autonomous VTOL aircraft in demanding real-world environments.

6.2. Future Work

Despite the substantial progress achieved, this research also uncovered new questions and areas for improvement. Several directions for future work are proposed to build on the present findings:

Firstly, conducting real-world flight tests offers a natural extension of the agile turning maneuvers identified in Chapter 5. So far, the optimal actuator combinations for minimum-radius turns were derived from wind tunnel data theoretically. Demonstrating these agile maneuvers in actual flight will validate the tilt-rotor tailsitter VTOL aircraft's potential as racing drones.

Secondly, building high-fidelity dynamic models based on the wind tunnel dataset enables the implementation of advanced model-based control approaches. Techniques such as Model Predictive Control (MPC) and reinforcement learning-based control benefit from accurate models to achieve precise maneuvering through cluttered environments while respecting aerodynamic constraints.

Thirdly, improving the platform's robustness and endurance expands its operational potential. While the current design reliably performs pivoting takeoff outdoors, it still requires reorientation to a vertical posture before liftoff. Investigating direct upwind takeoff could address limitations in strong winds. Additionally, the current configuration favors agility over endurance. Future efforts may adapt the aerodynamic model and control strategy to larger, longer-endurance platforms. Ultimately, combining agility, robustness, and extended flight time is essential for applications like long-range surveillance and continuous environmental monitoring.

Acknowledgements

I would like to express my deepest gratitude to Prof. Max Mulder and Prof. Guido de Croon for giving me the opportunity to start my PhD journey at TU Delft. I would also like to thank the China Scholarship Council (CSC) for the financial support that made my doctoral study possible.

I am sincerely grateful to my promotor, Prof. Guido de Croon, for his vision and guidance throughout my PhD. He always had a clear view of the big picture and provided strategic direction when my research felt uncertain or overwhelming. His encouragement, trust, and high academic standards have continuously motivated me to grow as a researcher. Special thanks go to my daily supervisor, Dr. Ewoud Smeur. His rigorous thinking, technical expertise, and dedication to precision offered important guidance and insights during my research process. More importantly, his kindness and approachability created an environment in which I always felt supported. His patience and insight taught me how to see beyond immediate results and pursue long-term scientific value.

I would also like to thank all my colleagues at MAVLab for providing such a warm, inspiring, and collaborative environment. To Yingfu, who was the first colleague I met in Delft. Throughout the five years, thank you for being a heartwarming colleague and more importantly, a reliable friend. To Hang, also my neighbor, thank you for providing inspiring views in research and helping me without hesitation in the emergent situation. To Liming and Baihui, thank you for the intense yet wonderful time we spent together during the wind tunnel experiments. To Chaoxiang, thank you for the thoughtful discussions on career planning and the relaxing tennis sessions. To Sunyou, thank you for all the museum visits, restaurant explorations, and small adventures across the Netherlands that made daily life colorful and memorable. To Sunyi, thank you for your guidance on the fan system and for the engaging conversations we shared in the office. To the master students, Gervase, Alexis and Yamac, it was a pleasure working with you. I would like to thank Erik for his tremendous help with hardware implementation and for his patience and professionalism. Many thanks to Alessandro and Vaggelis for driving together to Valkenburg for outdoor flight tests, and to Taran for taking care of flight test scheduling. I also thank all other lab members for their support in the organization of scientific presentations, and for the many coffee breaks and casual chats that brought warmth to everyday research life.

I am also thankful to my colleagues from the C&S section. To Esther, my desk mate, thank you for the bag tag that meant so much at the difficult moment. To Rowenna, thank you for organizing section activities and always being supportive.

I also thank Maria, with whom I attended career and DISC courses, for the inspiring conversations we shared. Many thanks to Yiyuan, my neighbor, for the discussions we had during our final PhD year, which provided insight, comfort, and encouragement. I also thank Jiayu and Wenying for the joyful barbecue nights, and all other C&S colleagues who made the workplace feel welcoming and alive.

During the five-year stay in Delft, I had a lot of experiences, some were challenging, some were fascinating, some remain unforgettable and invaluable moments in my life. I want to thank the people who shared the wonderful memories with me. To Xiaohuan, my truthful friend, We had so many overnight talks which were my main source of happiness in Delft. We traveled, shopped, gossiped, laughed together. The "blue tears" we saw along the beach in Den Haag tells how shining our happy hangouts are. To Cheng, it was an upmost interesting experience of advertising osmanthus-flavored iced-jelly together with you on the Erasmus Bridge, which lightened the Mid-autumn Festival of that year. It was also a good experience to play tennis with you. To Sherry and Sihao, and their beloved daughter Lianlian, thank you for organizing the road trip to Hamburg and gatherings especially Avalon games at your place. We shared so many happy memories and I cherish a lot. I also want to thank Shushuai and Zhou for hosting me in Switzerland, and Jingyi and Kai for inviting me to join them for movie. To Yujie, Yiru and Jingjing, brilliant girls and dear neighbors, We celebrated birthdays together, discussed research struggles, and most importantly we accompanied each other through this PhD journey. I have met so many amazing people in Delft, and although I cannot list all your names here, each of you has left an imprint on my life that I will forever cherish.

I owe my deepest gratitude to my best three friends, my "jiajia family". I thank my parents, Jing Xu and Chengtian Ma, for their unconditional support and love. They have witnessed my laughter and tears, my achievements and doubts, and accompanied me firmly through every stage of my life. I also would like to thank my boyfriend, Dr. Yu Wang. Thank you for accompanying me. We have been together for seven years, and five of which was in a long distance relationship since we both started our PhD in 2020. You support me, understand me, and love me. It's a great pleasure to have met you, like sunday, like rain.

Lastly, I want to thank myself, Ziqing. Thank you, for being brave during this challenging but awarding journey. I'm proud of you, as always.

Ziqing MA
Delft, September 2025

Curriculum Vitæ

Ziqing Ma

24.12.1996 Born in Zhongxiang, China.

Education

09.2010–06.2013	No.1 Middle School Affiliated to Central China Normal University
09.2013–06.2017	Bachelor, Northwestern Polytechnical University
09.2017–03.2020	Master, Northwestern Polytechnical University
10.2020–01.2026	PhD, Delft University of Technology *Dissertation:* Design and Control of a Tilt-Rotor Tailsitter Aircraft *Promotor:* Prof. dr. G.C.H.E. de Croon *Co-Promotor:* Dr. ir. E.J.J. Smeur

Experience

05.2012	International Youth Climate Summit Wolfsburg, Germany
07.2018	Summer School by University of Tokyo Tokyo, Japan
09.2023	International Micro Air Vehicle Competition Aachen, Germany
06.2024	”Aerotrain” Summer School by ETH Zurich Chania, Greece

List of Publications

4. **Z. Ma**, E.J.J. Smeur, G.C.H.E. de Croon, *Wind Tunnel Tests of a Tilt-Rotor Tailsitter Focused on Wing-Propeller Interaction*, submitted.

3. **Z. Ma**, E.J.J. Smeur, G.C.H.E. de Croon, *Design and control of a tilt-rotor tailsitter aircraft with pivoting VTOL capability*, IEEE Robotics and Automation Letters (2025) vol. 10, no. 6, pp. 5911-5918.

2. G.H.L.H. Lovell-Prescod, **Z. Ma**, E.J.J. Smeur, *Attitude control of a tilt-rotor tailsitter micro air vehicle using incremental control*, International Conference on Unmanned Aircraft Systems (ICUAS) (2023) pp. 842-849.

1. **Z. Ma**, E.J.J. Smeur, G.C.H.E. de Croon, *Wind tunnel tests of a wing at all angles of attack*, International Journal of Micro Air Vehicles **14**, 17568293221110931 (2022).

TU Delft
Delft
University of
Technology

ISBN: 978-94-6518-205-6